Investigation of alternative approaches for load recovery on a truck chassis using indirect measurements

by

Eugene Jacobs

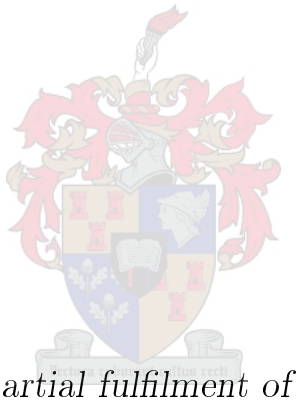

Thesis presented in partial fulfilment of the requirements for the degree of Master of Engineering (Mechanical) in the Faculty of Engineering at Stellenbosch University

Supervisor: Prof. G. Venter

March 2020

Declaration

By submitting this thesis electronically, I declare that the entirety of the work contained therein is my own, original work, that I am the sole author thereof (save to the extent explicitly otherwise stated), that reproduction and publication thereof by Stellenbosch University will not infringe any third party rights and that I have not previously in its entirety or in part submitted it for obtaining any qualification.

Date: March 2020 .....

Abstract

Investigation of alternative approaches for load recovery on a truck chassis using indirect measurements

E. Jacobs

Department of Mechanical and Mechatronic Engineering,
University of Stellenbosch,
Private Bag X1, Matieland 7602, South Africa.

Thesis: MEng (Mech)

March 2020

A proper description of the input loading experienced by a truck during operation is essential. This makes it possible to perform high quality finite element analysis which can validate designs numerically, rather than via physical prototype testing. Higher quality finite element analysis will lead to safer vehicle designs for drivers and the general public. Less time spent on prototyping would lead to faster releases of new designs into the market, preserving both time and money for manufacturers. The feasibility of alternative approaches for load recovery on a truck chassis using indirect measurements was investigated in this thesis. The first approach utilised acceleration measurements processed with multi-body dynamic simulations. The second approach utilised the linear relationship between strain and input loading and superposition to recover said input loading. Strain gauges were used as measurement instruments for this approach. Both approaches have advantages and disadvantages. Investigation of various influencing factors on both approaches led to the conclusion that load recovery, using acceleration data and a simple quarter truck model, produces load recoveries with sufficient accuracy. This approach is also the least computationally complex, is relatively easy to set up and is a low-cost alternative to direct measuring methods which use expensive force transducers instrumented in the load path. Furthermore, this approach does not alter

the truck in any way, aside from the instrumentation of accelerometers at key locations on the truck chassis and wheels.

Uittreksel

Ondersoek na alternatiewe benaderings van die insetlading wat 'n vragmotor-onderstel ervaar deur van indirekte metings gebruik te maak

E. Jacobs

Departement Meganiese en Megatroniese Ingenieurswese,
Universiteit van Stellenbosch,
Privaatsak X1, Matieland 7602, Suid Afrika.

Tesis: MIng (Meg)

Maart 2020

Die behoorlike beskrywing van die insetlading wat 'n vragmotor ondervind, is noodsaaklik om eindige elementanalises van hoë gehalte uit te voer. Hierdie eindige elementanalises bevestig ontwerpe numeries, eerder as om van fisiese prototipe-toetsing gebruik te maak. Eindige elementanalises van hoër gehalte sal lei tot veiliger voertuigontwerp vir bestuurders en die publiek. Minder tyd sal aan prototipe toetsing bestee word, wat sal lei tot vinniger vrystelling van nuwe ontwerpe aan die mark, wat die vervaardiger tyd en geld bespaar. Die haalbaarheid van alternatiewe metodes tot die benadering van die insetlading wat vragmotor-onderstel ervaar met indirekte metings was ondersoek in hierdie tesis. Die eerste benadering maak gebruik van versnellingsmetings, wat met versnellingsmeters gemeet was, en verwerk met dinamiese veel liggaam simulasies. Die tweede benadering het gebruik gemaak van die lineêre verband tussen spanning en insetbelasting om genoemde insetlading te herstel. Rekstrokies was as meetinstrument vir hierdie benadering gebruik. Beide benaderings het voor- en nadele. Na die ondersoek van verskillende beïnvloedingsfaktore op albei benaderings, was gevolgtrekkings gemaak dat akkurate vragherwinning met behulp van versnellingsdata en 'n eenvoudige model van 'n kwart vragmotor verkrybaar was. Hierdie benadering is ook die minste berekeningkompleks en relatief maklik om op te stel. Verder verander die benadering die vragmotor

op geen enkele manier nie, behalwe vir die instrumentasie van versnellingsmeters op sleutelplekke op die vragmotor-onderstel en wiele. Die metode is 'n laekoste-alternatief vir direkte meting metodes wat gebruik maak van duur lasomsetters wat op die trok se wielle geïnstalleer moet word.

Acknowledgements

I would like to express my sincere gratitude to the following people and organisations:

- Triz Engineering solutions for providing me the opportunity to further my studies by providing this project and funding.
- Prof. Gerhard Venter for sharing his experience and continuous guidance throughout the course of this project.
- My friends for their constant support.

Dedications

Hierdie tesis word opgedra aan ma en pa. Baie dankie vir al die liefde, ondersteuning en geleenthede wat julle vir my voorsien het oor die jare.

Contents

Declaration i

Abstract ii

Uittreksel iv

Acknowledgements vi

Dedications vii

Contents viii

List of Figures x

List of Tables xii

1 Introduction 1
- 1.1 Background . . . 1
- 1.2 Motivation . . . 1
- 1.3 Aim . . . 2
- 1.4 Scope . . . 2

2 Literature review 4
- 2.1 Different methods of load recovery . . . 4
- 2.2 Problem solving methodolody . . . 6
- 2.3 Rigid body dynamics . . . 7
- 2.4 Load recovery from stain gauge data . . . 11
- 2.5 Summary . . . 16

3 Truck instrumentation and models 17
- 3.1 Background . . . 17
- 3.2 Instrumentation . . . 18
- 3.3 Experimental data . . . 19
- 3.4 Finite element model . . . 22
- 3.5 Compensating for unaccounted masses . . . 26

4 Rigid body dynamics experiment 29
4.1 Derivation of required equations 29
4.2 Integration problem 31
4.3 Experimental setup parameter identification 32
4.4 Multi-body dynamic simulation 35

5 Truck multi-body dynamic simulation 38
5.1 Quarter truck model 38
5.2 Data post processing 41
5.3 System parameter identification using force and acceleration data 43
5.4 System parameter identification using only acceleration data . . 49
5.5 Summary 53

6 Load recovery from strain gauge data 55
6.1 Background 55
6.2 Load recovery with shell model 56
6.3 Impact of dominating forces 58
6.4 Load recovery using strain gauge field data 61
6.5 Payload optimisation 63
6.6 Recovery of payload size with strain gauge data 66
6.7 Load recovery using a beam model as experiment 69
6.8 Effect of random error on load recovery accuracy 72
6.9 Effect of D-optimal design 73
6.10 Summary 77

7 Conclusions and future research 79
7.1 Conclusions 79
7.2 Recommendations for future work 80

Appendices 82

A Provided truck dimensions 83

B Field data post processing 85

C Payload size recovery using strain gauge field data 90

List of References 93

List of Figures

2.1 CQUAD4 Element geometry and coordinate systems (Siemens, 2017). 14

3.1 Truck model similar to the truck used to gather field data and the roll-off mechanism. 17
3.2 Position and labels of various sensors fixed on the truck. 18
3.3 Wheel force transducer configuration on the test vehicle. 19
3.4 GPS track of payload pickup and delivery on 28/02/2018. 20
3.5 Comparison of recorded acceleration signal with double integrated and differentiated acceleration signal of accelerometer 2 for data Section B. 21
3.6 Measured strains for Runs 1 and 2 by certain strain gauges. 22
3.7 Truck schematics as provided that indicate key component positions. 23
3.8 Finite element model developed to model the truck. 24
3.9 Basic setup of the front leaf spring configuration. 25
3.10 Spider bolted connection connecting cross members, brackets and frames. 26
3.11 Basic setup of rear camelback suspension configuration. 26
3.12 Locations and connections of compensating masses. 27

4.1 Simple spring mass system experiment and a quarter truck model. . 29
4.2 Correlation between recorded and calculated force signals using identified system parameters. 33
4.3 Displacement signals produced by multi-body dynamic simulation using force data. 35
4.4 Multi-body dynamic simulation results using m_1's acceleration data. 36

5.1 Two degree of freedom quarter truck model (Alvarez-Sánchez, 2013). 39
5.2 Two degrees of freedom front quarter truck model. 40
5.3 Three degrees of freedom rear quarter truck model. 41
5.4 Fast Fourier transform of acceleration signal recorded by accelerometer 1. 41
5.5 Original and bandpass filtered accelerometer 1 data. 42
5.6 Correlation between recorded and estimated wheel forces for the left and right front wheels. 45

5.7 Correlation between recorded and estimated wheel forces for the left middle and left rear wheels. 47
5.8 Correlation between recorded and calculated wheel forces using an alternative dataset and identified parameters to validate results. . . 48
5.9 Sum of forces experienced by the truck chassis at the front left and right suspension attachment points. 51

6.1 Experimental cantilever beam setup used by Hunter (2018). 55
6.2 Unit loads applied to the FE model to generate a sensitivity matrix. 57
6.3 Application of all reaction forces and moments to the FE model. . . 59
6.4 Recovery accuracy of vertical reaction forces when using different numbers of virtual strain gauges. 60
6.5 Strain gauge positions and labels as instrumented on the truck. . . 62
6.6 Payload position optimised with wheel force transducer data. 64
6.7 Load case setup used to determine the sensitivity matrices used for load recovery of the payload size with field data. 67
6.8 Further simplified beam element FE model of the truck. 70
6.9 Correlation between variation in recovered vertical reaction forces with the number of strain gauges used. 73
6.10 D-optimal strain gauge locations on the truck chassis of $\boldsymbol{A}_{10}$. 75
6.11 Variation in recovered loads using D-optimal sensitivity matrices with random errors added to data. 75

B.1 Filtered and unfiltered acceleration signals captured by accelerometers on the truck's chassis. 86
B.2 Filtered and unfiltered vertical acceleration signals captured at the front and middle wheels. 87
B.3 Filtered and unfiltered vertical front and middle wheel forces. . . . 88
B.4 Filtered and unfiltered vertical accelerations and forces of the left rear wheel. 89

List of Tables

3.1 Route description for payload pickup and delivery on 28/02/2018. . 20
3.2 Comparison of vertical reaction forces at wheels with compensating masses as determined using wheel force transducer data. 28

4.1 Accuracy of system parameter identification for the experimental setup using force and acceleration data. 33
4.2 Estimated system parameters for 10 independent parameter identification optimisations using only acceleration data. 34

5.1 Identified parameters for the front left and front right quarter truck models. 44
5.2 Identified parameters for the left rear quarter truck models. 46
5.3 Identified parameters for the front left quarter truck model using only acceleration data. 50
5.4 Identified parameters for the front right quarter truck model using only acceleration data. 50
5.5 Relationship between identified system parameters for the rear quarter truck model using only acceleration data. 52

6.1 Accuracy of load recovery process for an ideal test case. 58
6.2 Reaction forces and moments measured by wheel force transducers for the unloaded truck in Run 1. 59
6.3 Accuracy of recovered vertical forces when using 14 virtual strain gauges. 61
6.4 Recovered vertical reaction forces experienced by the wheels during Run 2 and 3. 62
6.5 Comparison of vertical reaction forces at wheels due to payload as determined using WFT and strain gauge data. 66
6.6 Recovered payload size using one strain gauge at a time for the Run 2 dataset. 67
6.7 Recovered payload size using one strain gauge at a time for the Run 3 dataset. 68
6.8 Comparison of the vertical reaction forces as calculated by NX for a load case simulating Run 3. 70

6.9 Comparison of load recovery accuracy of vertical reactions when using data generated from the beam FE model. 71
6.10 Vertical loads recovered when using D-optimal sensitivity matrices for a gravity load case. 76
6.11 Load recovery results using $\boldsymbol{A}_{10}$. 77

A.1 Measurements of made available from which the FE models were developed. 83

B.1 Frequency ranges used for the bandpass filters applied to datasets captured with sensors. 85

C.1 Recovered payload size using one strain gauge at a time for the Run 2 dataset. 90
C.2 Recovered payload size using one strain gauge at a time for the Run 3 dataset. 91

Chapter 1

Introduction

1.1 Background

In the automotive design and development industry there is a constant drive for design improvement to achieve safer vehicles for the general public while reducing costs to manufacturers and satisfying client requirements. A significant expense to manufacturers is the physical testing of prototypes, which is cost and time intensive. Greater emphasis is currently placed on numerical techniques to validate designs, rather than with physical prototyping.

The finite element (FE) method has become an indispensable tool for most structural design applications in the engineering industry. Increasing sophistication in software and computing power in recent years has brought the technology into the economic grasp of most of the transport industry. When set up correctly, FE models can produce accurate simulations of real world load scenarios. One of the causes for inaccuracies in the FE analysis is undefined input loading. There is limited use for FE results when analysing a structure if the input loading is not well defined, as the results will not reflect real world scenarios.

Several methods for obtaining the input loading a truck experiences during operation will be researched in this thesis. There are a number of ways to calculate or recover these loads, each with their own advantages and disadvantages.

1.2 Motivation

In the automotive industry there is constant competition between manufacturers. The manufacturer with the best product at the lowest cost captures the market and there is always room for improvement.

New products need to be tested before release for commercial and public use. Testing, however, is both costly and time consuming. If input loading could be properly defined, FE analyses of higher quality could be performed. This would reduce the time required to perform physical prototype testing, allowing faster approval of concepts and earlier release to the market.

1.3 Aim

The research in this thesis will investigate current methods used to recover the input loading a truck experiences when in operation. The main objective being to identify a method that is accurate and cost effective. This method could be used to expedite the truck testing phase in the design of new vehicles, potentially saving time, money and improving the safety of designs for users and the general public.

Current methods can be divided into two groups namely: direct methods and indirect methods. Direct methods instrument force transducers in the load path to directly capture applied forces. Indirect methods measure the structure's response to an input force. The relationship between the response and the input is then used to recover the applied force. These responses are changes in quantities such as strain or acceleration. Indirect methods will be the focus of this research.

The objectives of this research are to:

1. Analyse the truck as a multi-body dynamic system to calculate input loads from accelerometer data.
2. Recover the input loading experienced by a truck using strain gauge data.
3. Make recommendations on which method would be best to map the input loading experienced by a truck.

Results produced using direct methods were made available for this research by an external company. Results produced with indirect methods will be compared with provided results.

1.4 Scope

The feasibility of using indirect methods rather than direct methods to recover the input loading experienced by a truck, will be extensively researched in this thesis. The two indirect methods considered in this research are:

1. Load recovery through a multi-body dynamic simulation.
2. Load recovery using strain gauge data.

These two methods utilise different types of data namely acceleration signals and strain responses. The relationship between both of these data types and truck's input loading will be determined.

The data used in this thesis was generated by a particular company which instrumented a truck with various sensors and performed experiments on that test vehicle. These sensors included wheel force transducers on wheel hubs, strain gauges and accelerometers. Data was gathered to assist in their design processes. This data has been made available to conduct research. It is important to note that no further in-house experiments were possible on the test vehicle and that data was not gathered solely with load recovery in mind.

Chapter 2

Literature review

There are different methods for investigating the input loading of trucks, requiring different sources of input data and approaches. Strain gauge, accelerometer and wheel force transducer data have been made available for this research. These datasets determined which methods that needed to be researched in the literature study.

2.1 Different methods of load recovery

Load inputs to a system are obtained from either simulation, direct or indirect measurements. System in this context refers to the truck. These loads can be used as inputs for stress analyses that can be either dynamic, quasi-static or static. Fatigue analyses are then based on these stress results (Wannenburg, 2007). A couple of different methods of load recovery are listed below with some of their advantages and disadvantages.

2.1.1 Measuring input loading directly with load transducers

This method introduces specialised load transducers between the structure and the body transferring the load (Gupta, 2013). The loads acting on the structure can be directly measured. This method was applied by an external company and the resulting data made available to use in this research. Load transducers were instrumented on the wheel hubs of a truck that directly measured the input loading that resulted from contact between the wheels and the road. The truck was then operated as usual performing deliveries of cargo. The truck was subjected to different terrain and driving conditions during these deliveries. Delivery routes included on-road, off-road, on highway and inner city driving conditions. A full description of the input loading experienced by each wheel during truck operation was captured. This method has some limitations as the

load transducers can change the system's dynamic properties that could lead to inaccurate load measurements. In other words, it could affect how loads are transmitted to the structure. In addition, these transducers are expensive to instrument. More details concerning the transducer instrumentation and data gathered by these systems is provided in the following chapter.

2.1.2 Rigid body dynamic simulation

A rigid body dynamic simulation is another important method to determine the load response of vehicle structures. In this technique, a dynamic model of the truck system is constructed. The model truck is then traversed over a terrain with known geometric profiles through simulation to solve for the dynamic input loading (Wannenburg and Heyns, 2010). Alternatively, if the geometric profile (road profile) is not available, the wheel forces or wheel accelerations could be used as inputs to the dynamic model. Certain complexities accompany this method such as the double integration of acceleration measurements. This method also relies on the availability of all suspension parameters such as the spring stiffness and damping to set up the dynamic model. The methodology for the application of this method is provided in the following sections.

2.1.3 Load recovery from strain response

Within the context of load recovery on a dynamic structure the FE analysis can be considered as quasi-static in many cases. Load recovery with this approach involves calculating the stress/strain response for system elements caused by applying all static unit loads acting on the structure one by one (Wannenburg, 2007). These responses are then used to construct a quasi-static transfer matrix between element stresses and loads. The stress/strain histories are then multiplied with the inverse of the transfer matrix to solve for the input loading. Load recovery in this manner avoids difficulties that accompany methods using specialized load cells and acceleration measurements. Instead, the structure becomes its own load transducer (Hunter, 2018). This method has complexities such as where and how many strain gauges on the structure to capture load histories among others. Furthermore, if the input loads need to be recovered for another road event, loading condition or road surface strain gauge data needs to be captured and available for these conditions. Thus, the instrumented vehicle must be tested under these conditions of interest. The methodology for the application of this method is provided in the sections that follow.

2.2 Problem solving methodolody

Load recovery using rigid body dynamic simulations or using the structure's strain response, require different methodologies for their application. Steps outlining the process for load recovery with either of these methods are laid out below.

2.2.1 Problem solving methodology for rigid body dynamics

To accomplish load recovery using wheel acceleration data, certain steps have to be taken. Without the availability of a road profile a physical experiment to gather acceleration data is required. The following steps were used to accomplish load recovery without the availability of a road profile (Wannenburg and Heyns, 2010):

- Measure accelerations experienced by the wheels while the truck is in operation.
- Derive a mass-spring-damper model of the truck.
- Identify the system parameters of the truck model, if they are unknown.
- Derive a transfer function that relates input and output loads on the system.
- Calculate the loads acting on the system components of interest using the developed transfer function and acceleration data.
- Compare recovered load's quality and accuracy produced by using different sets of input data.

2.2.2 Problem solving methodology for load recovery from strain response

A methodology developed by Ford Motor Co. can be used to solve for loads acting on the system from strain gauge data (Pountney and Dakin, 1992). The methodology's purpose is to do a numerical durability assessment on a subassembly or component using remote measurements of strain experienced by system components, to determine quasi-static loading. Remote meaning not at the location where the input loading was applied. The steps to apply this approach on the truck are (Wannenburg and Heyns, 2010):

- Build a finite element model of the truck chassis.
- Determine strain gauge locations from the strain field information. The number of gauges should be more or equal to than the number of unknown forces.

- Take strain gauge measurements of the system components under consideration.
- Identify a constraint set and apply unit loads to the finite element model.
- Derive a sensitivity matrix (gauge-to-load transfer matrix).
- Invert the sensitivity matrix and recover the loads acting on system components using measured strain gauge data.
- Derive a load-to-response transfer matrix. This can be done from the results of the FE model when inducing unit loads. Without performing the FE analysis again, a rapid solution of component stresses can be obtained for each time-step load set.

2.3 Rigid body dynamics

2.3.1 Background

A rigid body can be described as a conjunction of a large number of particles that remain at a fixed distance from each other before and after a force is exerted (Hibbeler and Yap, 2012). The body is rigid since it does not deform or change shape, so the material from which the body is made does not need to be considered. This type of analysis is suitable to cases where deformations are relatively small.

Rigid body dynamics is also known as multi-body dynamics when more than one mass is considered. In the case of a vehicle there are generally 3 bodies to consider: the vehicle's body mass and the fore and rear suspension's unsprung masses. All bodies are considered to be rigid and deformations are therefore considered negligible. Dynamic simulation starts with the derivation of a dynamic (mass-spring-damper) model, that represent the real structure, in this case a truck. By traversing this truck model over a terrain of known geometrical or statistical profiles through simulation, the dynamic input loading can be recovered.

There are generally 3 different types of multi-body simulation. Type 1 obtains input loading without the availability of measurements. Digitised road profiles are used as inputs for the model. Through simulation input loading can be solved. One of the fundamental difficulties of this method is the complexity of vehicle tyre modelling. Significant errors arise when tyre models are simplified (Wannenburg, 2007). In type 2, load inputs are obtained on suspension hard points by measuring wheel spindle loads. This method requires specialized load cells that are expensive to implement. Type 3 obtains inputs on suspension hard points by measuring wheel accelerations. A drawback of this approach is difficulties associated with the double integration of acceleration measurements.

Results of dynamic simulation by implementation of type 2 and 3 will be compared in this document. In order to do this, it is important to determine the impact that wheel force transducer data has on load recovery quality and accuracy. For these approaches to be employed a truck model must be available. This means that the suspension parameters such as stiffness and damping must be known.

2.3.2 Systems and system models

A system is defined as a combination of components that act together to perform a certain objective (Kulakowski *et al.*, 2007). Systems change over time. In dynamic systems the rate of change is significant. A vehicle driving over a road can be considered as a dynamic system and it therefore makes sense to build a dynamic model of the system. The value of such a model lies in the possibility for testing and developing how the physical system will react to inputs from its surroundings. A model allows designers to experiment with different system parameters at a fraction of the cost associated with physical prototype testing. In one of the approaches researched in this thesis, a dynamic model will be used to estimate the input loading, bypassing the need to implement expensive load transducers on test vehicles. Instead, a process that utilises accelerometer data and a dynamic simulation will be used to recover these loads.

A system interacts with its surroundings through inputs that originate outside the system and are not affected by what happens inside the system. The results of this interaction are outputs that are of primary interest (Kulakowski *et al.*, 2007). Outputs, such as displacements and velocities, are required to describe the system itself. This set of variables is the minimum number of variables required to completely describe the system's state at any given instant in time and these can be measured.

Given the input and output variables and the initial state of the system, an instant-to-instant response of the system can be described (Kulakowski *et al.*, 2007). Outputs usually measured on vehicles are displacements, accelerations, wheel forces and strains. A discrete dynamic system may be described with the equation:

$$\boldsymbol{M\ddot{u} + C\dot{u} + Ku = p} \tag{2.1}$$

where $\boldsymbol{M}$ is the mass matrix, $\boldsymbol{\ddot{u}}$ the acceleration vector, $\boldsymbol{C}$ the damping matrix, $\boldsymbol{\dot{u}}$ the velocity vector, $\boldsymbol{K}$ the stiffness matrix, $\boldsymbol{u}$ the displacement vector and $\boldsymbol{p}$ the load vector (Wannenburg and Heyns, 2010). The mass, damping and

stiffness matrices are known as the system parameters. These parameters are not always known and can be determined with the methods outlined below.

2.3.3 System parameter identification

The basic concept of parameter identification is to compare the actual system responses with a parameterised model based on a performance function which provides a measure of how well the system response correlates with the model (Alfi and Modares, 2010). Parameter estimation is an inverse problem and can be constructed as an optimisation problem. Conventional methods to determine suspension parameters have been extensively researched using optimisation algorithms and accompanying objective functions (Alfi and Fateh, 2010).

The gradient based optimisers have fundamental problems. These include the differentiability of the performance function and unimodal performance landscapes, as well as trapping in local minima (Ursem and Vadstrup, 2004). This is where swarm intelligence and evolutionary algorithms (EAs) are promising alternatives, as they can escape local minima and are not as affected by the previously mentioned fundamental problems (Alfi and Fateh, 2010). These algorithms do require parameter tuning and more function evaluations than gradient based optimisers.

A widely used method to determine unknown parameters in a model is by minimising the Sum Square of Errors (SSE) that is defined as follows:

$$SSE = \sum_{i=1}^{n} \big(y(i) - \hat{y}(i)\big)^2, \tag{2.2}$$

where n is the length of data used for parameter identification, $y(i)$ and $\hat{y}(i)$ are the real and estimated function values at each sample time point, i, respectively. The objective is the system parameters that would minimise the SSE value. The calculation of system parameters is a complicated engineering problem. The objective function might have multimodality that can cause problems for gradient-based methods.

A more robust optimisation algorithm such as a genetic algorithm (GA) or particle swarm optimisation (PSO) would be ideal to determine system parameters as they have an increased probability of finding the global minimum (Alfi and Modares, 2010). In general, no algorithm can guarantee the global optimum solution. PSO methods have been compared to other optimisation methods for parameter identification, such as genetic algorithms. It has been proven that PSO is more robust and avoids premature convergence problems

effectively (Alfi and Fateh, 2010). Furthermore, PSO is easier to implement and less computationally complex but more computationally expensive than a GA. With modern processing power available, the computing power required for PSO was not considered to be a problem. For these reasons PSO will be used to identify the required suspension parameters of the truck in this thesis.

2.3.4 Basic PSO

PSO uses the simulation of the flocking and movement of birds to search for the best solution (Kennedy and Eberhart, 1995). The algorithm starts by initialising a flock of birds/particles over the search space. Every particle is encoded as a set of possible solutions for the problem (Alfi and Modares, 2010). These particles then 'fly' into the search space with certain velocities and inertia and find the global best solution after some iteration (Alfi and Fateh, 2010).

All information is shared between particles at each iteration. This allows each particle to adjust its velocity vector that depends on its inertia and the best position in the group's history. The particle then moves to a new calculated position and the process is repeated until convergence. If the search space is n-dimensional, then the velocity and position of particle i are represented by $\boldsymbol{v}_i = \left[\begin{array}{cccc} v_{i1}, & v_{i2}, & \cdots, & v_{in} \end{array} \right]^T$ and $\boldsymbol{x}_i = \left[\begin{array}{cccc} x_{i1}, & x_{i2}, & \cdots, & x_{in} \end{array} \right]^T$ respectively. Every particle's fitness is then evaluated according to the objective function setup as with Equation 2.2 for the problem optimised in this thesis. Particle i's best position visited earlier is stored as $\boldsymbol{p}_i = \left[\begin{array}{cccc} p_{i1}, & p_{i2}, & \cdots, & p_{in} \end{array} \right]^T$ and the particle with the current best global position is noted as $\boldsymbol{g} = \left[\begin{array}{cccc} g_1, & g_2, & \cdots, & g_n \end{array} \right]^T$. Each particle's velocity and position is updated for every iteration as follows:

$$\boldsymbol{v}_i(t+1) = \omega \boldsymbol{v}_i(t) + c_1 r_1(\boldsymbol{p}_i - \boldsymbol{x}_i) + c_2 r_2(\boldsymbol{g} - \boldsymbol{x}_i) \tag{2.3}$$

$$\boldsymbol{x}_i(t+1) = \boldsymbol{x}_i(t) + \boldsymbol{v}_i(t+1) \tag{2.4}$$

where t is the previous iteration number, and ω is the momentum or inertia weight that determines the impact of the previous iteration's velocity on the current one. r_1 and r_2 are random variables in the range of [0,1] that are generated uniformly and independent from each other. c_1 and c_2 are acceleration coefficients (typically $c_1, c_2 = 2$) that are known as the cognitive and social parameters. These parameters are constant and positive and control the maximum step size. Convergence is achieved by applying equations 2.3 and 2.4 to every particle (Alfi and Modares, 2010).

The tuning of parameters ω, c_1 and c_2 has a significant impact on PSO performance. If these parameters are not set correctly for the specific objective function at hand, inaccurate results will be produced by the optimisation. When $c_1 \ll c_2$ the PSO converges prematurely as particles are more attracted to the current global best position than their personal best positions. When $c_2 \ll c_1$ the PSO may converge slowly or not at all. This is due to particles being more attracted to their personal best solution rather than the global best (Agrawal and Agrawal, 2015). For these reasons c_1 and c_2 are chosen to be close to each other. Values that are too large cause swarm divergence.

Inertia weight, ω, can be determined by various different strategies (Bansal *et al.*, 2011). Literature concludes highest accuracy is achieved when using Chaotic Inertia Weight and the best efficiency of PSO is achieved when Random Inertia Weight is applied. Inertia weights are calculated with

$$\omega = 0.5 + \frac{\text{Rand}(0.4, 0.9)}{2} \tag{2.5}$$

when using the Random Inertia Weight approach.

2.4 Load recovery from stain gauge data

2.4.1 Background

Load recovery is possible because of the linear relationship between loads and strains. Superposition can be used because of this linear relationship. External loads applied to a structure impose changes in quantities, such as strains, stresses, displacements etc. (Dhingra *et al.*, 2013). It is possible to determine the loads a structure experiences through indirect measurements. By measuring another quantity such as strain, the loads could be calculated by looking at the linear relationship between the applied load and the measured quantity.

A transfer function relating measured and desired quantities can be determined numerically using finite element analysis. The use of strain gauges to measure loading has become quite popular, as they are relatively cheap. The location, orientation and quantity of strain gauges used for measurements have an influence on the quality of the load estimates. These influences are discussed in a following section.

The problem in this thesis is the estimation of k quasi-static input loads acting on a truck by using m strain gauges mounted on it where $m \geq k$. The system is assumed to be linear where strains are assumed to be proportional to the applied loads. The strain can then be calculated with

$$\boldsymbol{\varepsilon} = \boldsymbol{A}\boldsymbol{f} \tag{2.6}$$

where $\boldsymbol{\varepsilon}$ is a $m \times 1$ vector of strains, $\boldsymbol{A}$ an $m \times k$ matrix of sensitivity coefficients and $\boldsymbol{f}$ is a $k \times 1$ vector of loads (Dhingra *et al.*, 2013). The sensitivity matrix $\boldsymbol{A}$ can be determined from an FE model of the truck chassis, explained in more detail below, and the $\boldsymbol{\varepsilon}$ vector is constructed from the strain gauge measurements. With these two parameters known, the unknown load vector can be estimated as:

$$\hat{\boldsymbol{f}} = (\boldsymbol{A}^T\boldsymbol{A})^{-1}\boldsymbol{A}^T\boldsymbol{\varepsilon} \tag{2.7}$$

Where $\hat{\boldsymbol{f}}$ denotes a least-squares estimate of the unknown load $\boldsymbol{f}$. Note that uncertainties in the load estimates can be minimised by selecting measurement points for which the matrix $(\boldsymbol{A}^T\boldsymbol{A})^{-1}$ is well conditioned. The best estimates for loads are made when the determinant of $\boldsymbol{A}^T\boldsymbol{A}$ is maximised (Dhingra *et al.*, 2013). These designs are called D-optimal (Mitchell, 1974).

2.4.2 D-optimal design

The D-optimal design is needed to ensure the best estimates for loads by ensuring that the matrix $(\boldsymbol{A}^T\boldsymbol{A})^{-1}$ is well-behaved. This is done by selecting the best measurement locations for the strain gauges from a candidate list of locations provided to the algorithm. D-optimal designs have a wide range of applications in many fields. The D-optimal criterion is attractive here as it produces designs that are invariably 'good' in many respects (Mitchell, 1974). These include low variance and correlation between parameters. In the context of load recovery with strain gauge data, a D-optimal design can be implemented to assist in the determination of (Dhingra *et al.*, 2013):

- Locations on the structure's surface where strain gauges should be mounted.
- At what orientation these gauges should be mounted.
- The number of gauges that should be used.

To apply the D-optimal algorithm a sensitivity matrix must first be established. Steps outlining the process to achieve this are provided in the following section. Every strain gauge position on the structure being analysed is a candidate point for inclusion in the sensitivity matrix. First, from the set of all possible strain gauge positions a random subset of n strain gauges is selected. Each candidate gauge location not currently selected is adjoined to the $\boldsymbol{A}$ matrix one by one. Then the determinant of the adjoined matrix with $n + 1$ gauges

is calculated. The row that resulted in the largest increase of the determinant of the adjoined matrix is retained, and the inverse is updated. The addition of the most, and removal of the least, sensitive gauges is repeated until the determinant cannot be further improved (Mitchell, 1974).

2.4.3 Generating the sensitivity matrix $\boldsymbol{A}$

The process starts with the generation of an FE model of the truck chassis. The elements in this model should allow for the availability of surface strain information, as strain gauges will be mounted on the surfaces of components. The mesh size of the FE model must be compatible with the strain gauge's physical dimensions (Dhingra *et al.*, 2013).

Unit loads corresponding to each load which needs to be estimated are then applied to the chassis FE model. Strain fields that result from each of the unit loads are computed at each of the candidate locations for the strain gauges. Strain transformation relations are applied to the FE analysis to generate a strain response at each component of the chassis for all gauge angular orientations θ, where $0 \leq \theta \leq 180$ (Dhingra *et al.*, 2013). In practice only a few different angles are considered, for example angles in increments of 15 degrees between $0 \leq \theta \leq 180$. These angles represent the orientation with which strain gauges need to be instrumented on structure components.

Strain data provided for this research was produced as a result of strain gauges that were already instrumented on a test truck before the conception of this project. More detail on the truck instrumentation is provided in the following chapter. These mounted strain gauges were fixed in location and in orientation. Thus, there was no need to set up rotation matrices to optimise strain measurements. The combination of strain gauges to include in the $\boldsymbol{A}$ matrix is important as some strain gauges are more responsive to the input loading than others. Each row of the $\boldsymbol{A}$ matrix represents the response of a strain gauge to each individual load. D-optimal design is done to select which strain gauges to include in the $\boldsymbol{A}$ matrix.

Elements in the FE model have their own orientation according to their local coordinate systems in the $x'y'z'$ coordinate space, which do not always align with the global coordinate system in the xyz space. The direction of elemental vectors are purely based on node numbering of the four corner nodes of each shell element as shown in Figure 2.1.

Thus, the strain tensors of elements at locations of interest must be rotated so that their local coordinate system aligns with the global coordinate system. This is necessary if the simulated strains are to be compared with the measured data that was captured with strain gauges instrumented in accordance with

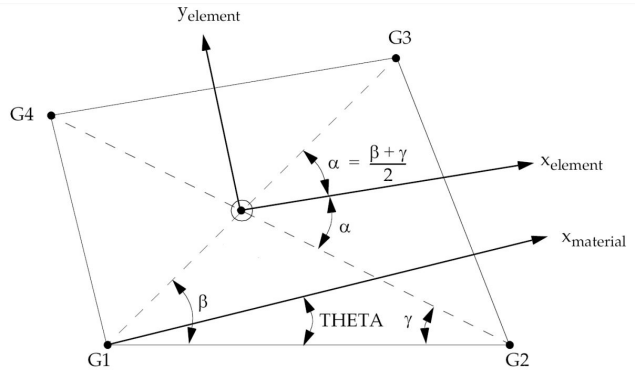

Figure 2.1: CQUAD4 Element geometry and coordinate systems (Siemens, 2017).

the global coordinate system. Strain tensors can be transformed as (Budynas, 1999):

$$[\varepsilon_{xyz}] = [\boldsymbol{Q}][\varepsilon_{x'y'z'}][\boldsymbol{Q}]^{\boldsymbol{T}} \tag{2.8}$$

where $\boldsymbol{Q}$ denotes the transformation matrix. $\boldsymbol{Q}$ contains the direction cosines that relate the global coordinate system, xyz, and the elemental coordinate system, $x'y'z'$, with each other (Cook *et al.*, 2007). The transformation matrix $\boldsymbol{Q}$ can be written as:

$$\boldsymbol{Q} = \begin{bmatrix} Q_{xx'} & Q_{xy'} & Q_{xz'} \\ Q_{yx'} & Q_{yy'} & Q_{yz'} \\ Q_{zx'} & Q_{zy'} & Q_{zz'} \end{bmatrix}$$

where $Q_{xx'}$ is the cosine between the global x vector, $\boldsymbol{x}$, and the elemental x vector, $\boldsymbol{x'}$. It is thus important to determine the vectors that describe $\boldsymbol{x'}$, $\boldsymbol{y'}$ and $\boldsymbol{z'}$. Coordinate data for points denoted as G1, G2, G3, and G4 in Figure 2.1 are available in the Nastran output files. From this, vectors describing $\boldsymbol{g}_{13}$, $\boldsymbol{g}_{12}$ and $\boldsymbol{g}_{24}$ can be determined. The dot product of these various vectors produce angles β, γ and finally α. The dot product of two vectors $\boldsymbol{u}$ and $\boldsymbol{v}$ is:

$$\boldsymbol{u} \cdot \boldsymbol{v} = ||\boldsymbol{u}||||\boldsymbol{v}||cos\phi = u_1v_1 + u_2v_2 + u_3v_3 \tag{2.9}$$

where ϕ is the angle between the two vectors. In order to determine the elemental vectors it is necessary to go back to the fundamentals of vector cross products. The cross product between the two vectors $\boldsymbol{u}$ and $\boldsymbol{v}$ can be written as (Hibbeler and Yap, 2012):

$$\boldsymbol{u} \times \boldsymbol{v} = \begin{vmatrix} i & j & k \\ u_1 & u_2 & u_3 \\ v_1 & v_2 & v_3 \end{vmatrix} = \begin{vmatrix} u_2 & u_3 \\ v_2 & v_3 \end{vmatrix} i - \begin{vmatrix} u_1 & u_3 \\ v_1 & v_3 \end{vmatrix} j + \begin{vmatrix} u_1 & u_2 \\ v_1 & v_2 \end{vmatrix} k \quad (2.10)$$

Vectors $\boldsymbol{g}_{13}$ and $\boldsymbol{g}_{24}$ are always in plane with each other and the element. Their cross product will always produce a vector perpendicular to CQUAD4 element's plane, which is $\boldsymbol{z'}$. By applying an in-plane anticlockwise rotation of $\boldsymbol{g}_{24}$ by the angle α around $\boldsymbol{z'}$:

$$\boldsymbol{x'} = \begin{bmatrix} cos\ \alpha & sin\ \alpha & 0 \\ -sin\ \alpha & cos\ \alpha & 0 \\ 0 & 0 & 1 \end{bmatrix} \boldsymbol{g}_{24} \begin{bmatrix} cos\ \alpha & sin\ \alpha & 0 \\ -sin\ \alpha & cos\ \alpha & 0 \\ 0 & 0 & 1 \end{bmatrix}^T \quad (2.11)$$

$\boldsymbol{x'}$ is determined. Next, $\boldsymbol{y'}$ can be determined by simply taking the cross product of $\boldsymbol{z'}$ and $\boldsymbol{x'}$. Finally, $\boldsymbol{Q}$ can be populated and the transformation matrix determined. This process was implemented in Python and used to transform all virtual strain gauge data generated by FE models in later chapters. This made it possible to compare virtual strain gauge data with actual strain gauge data, where the gauges were instrumented in accordance with the global coordinate system.

2.4.4 Inertia Relief

Boundary conditions play a big factor when setting up an FE model. Constraining the model incorrectly leads to inaccurate and unusable results. In this model the loads of interest that need to be estimated act on the suspension system, which are the points that need to be constrained. The load recovery process depends on the potential to apply unit loads to build up a sensitivity matrix. Constraining the model at points where unit loads are applied is problematic as there will be no deformation and no strains in the model. Unconstrained structural systems can be effectively modelled using inertia relief analysis (Siemens, 2014).

The inertia relief calculation assumes that the unconstrained structure is in a state of static equilibrium (Liao, 2011). An acceleration is calculated at all nodes of the structure that result in a total force that is in equilibrium with the applied force. A unique solution can be produced for an unsupported load case (Johannesson and Speckert, 2013). Nodal accelerations are applied in a manner that only accounts for rigid body modes and does not induce any deformation. Calculated deformations are only due to input loads applied to the inertia relief load case. This method provides an alternative way to apply

unit loads to the FE model at points that would otherwise be constrained with boundary conditions, without altering the model's stiffness matrix. Note that since accelerations are used to counter applied loads, loads such as gravity will be cancelled out leading to no deformation results.

2.5 Summary

This literature review has presented all the required theory pertaining to the chapters that follow. The two different approaches of load recovery discussed in detail, as well as the underlying background information, have discussed how to implement these approaches.

Rigid body dynamics will require modelling a dynamic system where all the system parameters are unknown and need to be identified first. These parameters will be identified using a basic particle swarm optimisation algorithm as the method of optimisation.

Load recovery with strain gauge data will require the generation of a sensitivity matrix that relates the input loading to strain response. This will require the application of unit loads to a developed truck FE model to determine the strain response at strain gauge locations due to each individual unit load. This is possible by appropriately using inertia relief and tensor rotation. Furthermore, the effect of D-optimal design application on load recovery will be investigated.

Chapter 3

Truck instrumentation and models

3.1 Background

A six-wheeled truck that is driven by the back four wheels as shown in Figure 3.1a was instrumented with various sensors, including: strain gauges, accelerometers and wheel force transducers. Data was recorded concerning what the truck experiences in regular day-to-day operation. These operations included static load cases, off-road and on-road driving, driving at landfill sites, in-city and highway commutes. Payloads varied as this was a roll-off truck transporting containers filled with different loads. Roll-off trucks have a hydraulically operated bed that uses a cable winch system to load and unload roll-off containers as shown in Figure 3.1b.

(a) Similar truck model (My Little Salesman, Inc., 2019).

(b) Roll-off mechanism (Wikimedia Commons, 2019).

Figure 3.1: Truck model similar to the truck used to gather field data and the roll-off mechanism.

Data collection did not form part of this research effort and was conducted by

a company that specialises in truck design. The data was collected before this research project was formulated and started. Data was thus not collected with this project in mind. However, the data was made available to this project as a real life test case of the methodologies developed and investigated here.

3.2 Instrumentation

The truck was outfitted with various instrumentation to determine what magnitude and type of loading this truck experiences while in operation. As the data was not gathered with the current project in mind, strain gauges and accelerometers were placed at non-optimal points from a load recovery perspective. Instrumentation fixed to the truck included strain gauges stuck at 41 locations, 6 wheel force transducers and 9 accelerometers. Strain gauges were of the KFGS series (350 Ω) available from Kyowa. The wheel force transducers were rented from Michigan Scientific and were the model: LW-2T-60K-S & LW-2T-100K-S heavy duty wheel force transducer. Accelerometers were procured from Silicon Designs and were the model: 2260-025 single axis. Not all these sensors were used during the investigation of the different methods. Sensors that were used during investigations were located on the truck as shown in Figure 3.2. These sensors recorded data from the truck's day-to-day operation. Sensor numbers/labels were kept the same as those provided by the company to avoid confusion when working with the data.

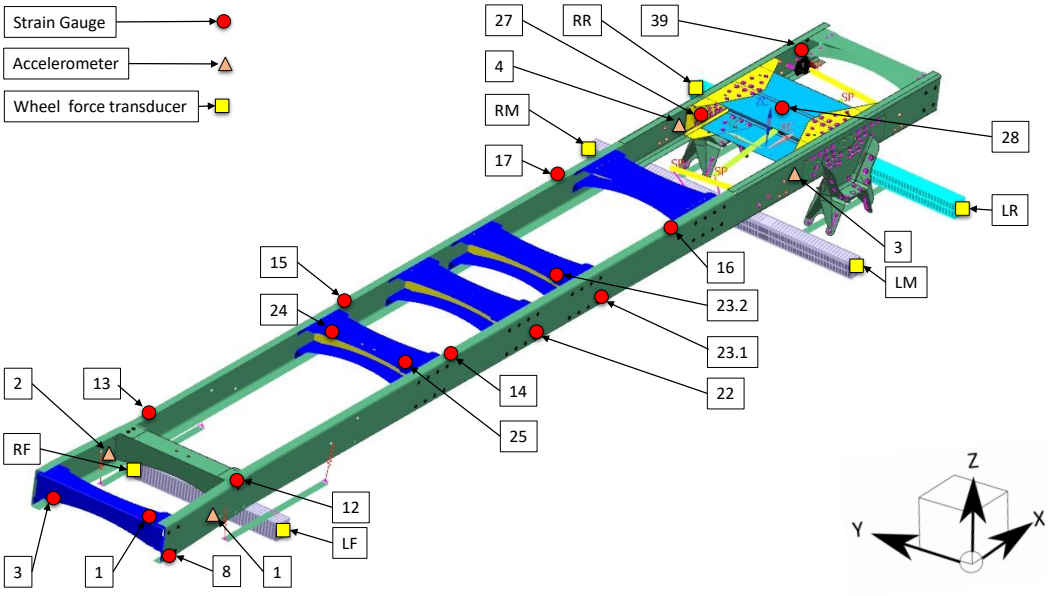

Figure 3.2: Position and labels of various sensors fixed on the truck.

From all of the strain gauges placed on the truck, there were only 17 gauge locations that were useful. A location was considered useful if it was on the truck chassis' main frame and not on secondary brackets, the exhaust stack or cab for example. Strain gauges 12, 13, 14, 15, 16 and 17 were set up with a full bridge configuration to account for bending. All other locations were instrumented with strain gauge rosettes that measured in the 0, 45 and 90 degree orientations in quarter bridge configurations. Thus, there was a total of 39 strain gauges that captured data that was useful for research purposes. Only 4 of the accelerometers were fixed on the frame and were considered 'useful'.

Wheel force transducers were mounted as shown in Figure 3.3 at the right rear (RR), left rear (LR), right middle (RM), left middle (LM), right front (RF) and left front (LF) wheels. All 6 wheel force transducers recorded forces and accelerations experienced by the wheels of the truck while in operation.

(a) Front wheel force transducer setup.

(b) Rear wheel force transducer setup.

Figure 3.3: Wheel force transducer configuration on the test vehicle.

3.3 Experimental data

Different sets of field data were provided for this project. The first set was raw unaltered and unfiltered data generated by the truck performing a regular delivery of a payload on the 28th of February 2018. The route description is shown in Figure 3.4 and Table 3.1. This data set was selected to conduct analysis on as it contained a combination of driving conditions.

In the load recovery considered here, this data will be used in the multi-body dynamic simulations. As a result, a double integration of the acceleration signals were required to produce velocity and displacements of truck components over time. This integration was performed using commercial software

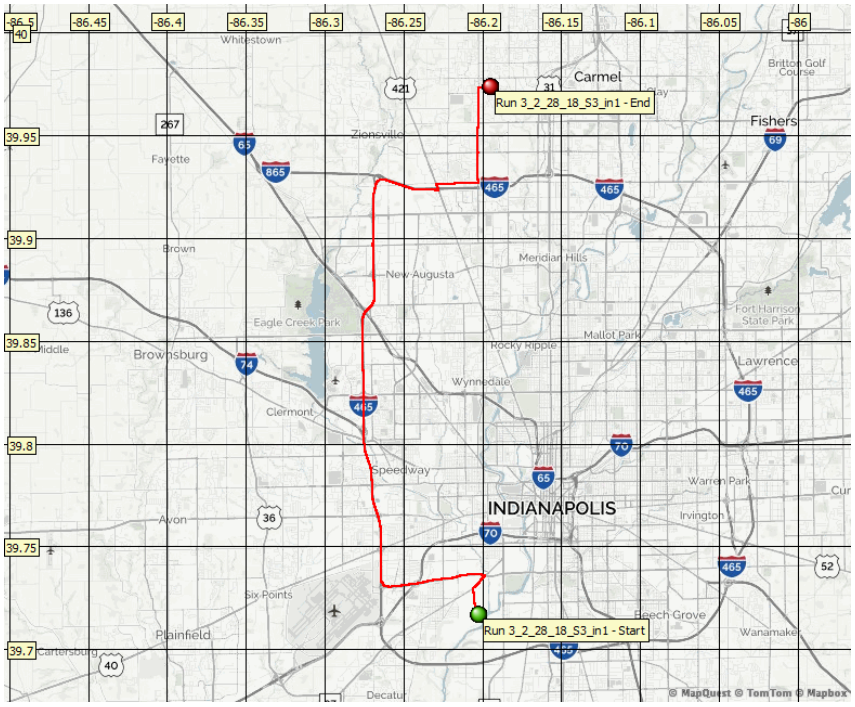

Figure 3.4: GPS track of payload pickup and delivery on 28/02/2018.

Table 3.1: Route description for payload pickup and delivery on 28/02/2018.

Section	Time start [hr:mm:ss]	Time end [hr:mm:ss]	Description
A	00:00:00	00:03:36	Stationery at South Side Landfill
B	00:03:36	00:07:56	Landfill driving
C	00:07:56	00:15:19	Off highway driving
D	00:15:19	00:31:24	On highway driving
E	00:31:24	00:45:00	Off highway driving to 12855 Birdcage Drive, Carmel, IN
F	00:45:00	01:01:11	Container Exchange

known as nCode Glyphworks (HBM, 2015). Glyphworks contains a powerful set of pre-defined tools used for digital signal processing. This software is designed to handle large data sets in a graphical, process-orientated environment. A workflow analysis is created by graphically connecting analysis building blocks. This allows users to track the result of each process on the input signals.

Integration quality was assessed by integrating the acceleration signal twice and then plotting the double differential of that signal alongside the original for comparison. An example of this comparison for the acceleration signal

recorded by Accelerometer 2 is shown in Figure 3.5. Accelerometer 2 recorded vertical accelerations experienced by the truck's frame and also captured the static offset generated by gravity. This static offset was removed from the original signal when checking integration quality and is the reason why the blue signal is centred around 0. Both signals were detrended and passed through a low pass filter after integration and plot in Figure 3.5b. Delta is the difference between the original and the double integrated and differentiated acceleration signals after filtering and detrending. Minimal data quality was lost during the double integration followed by a double differentiation process.

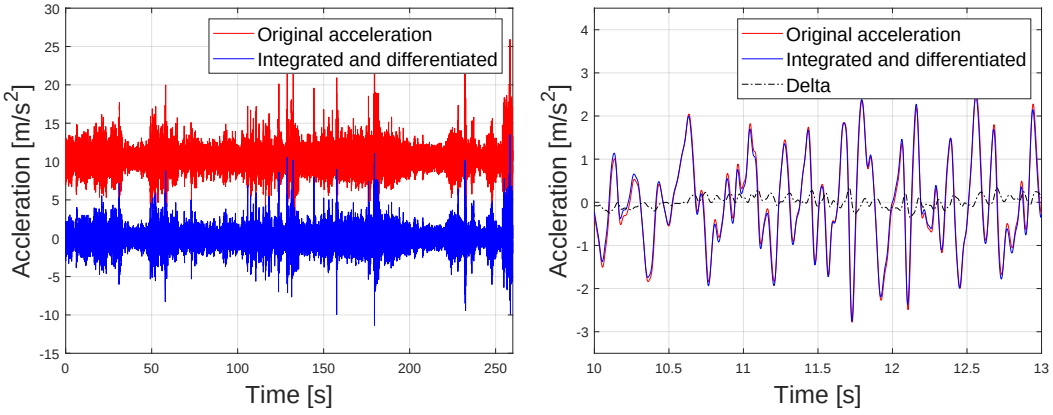

(a) Unaltered signals

(b) Filtered and detrended signals

Figure 3.5: Comparison of recorded acceleration signal with double integrated and differentiated acceleration signal of accelerometer 2 for data Section B.

Three additional field data sets were provided. For all three of these sets the truck was stationary under different loading conditions. These data sets were named Run 1, 2 and 3, where Run 1 was for an unloaded truck, for Run 2 an empty container rested on the truck, and for Run 3 the truck was loaded with 3.7 tons logged at a weigh bridge. These data sets were identified as ideal for load recovery with strain gauge data as loading conditions were well known. Once load recovery with static strain gauge data was achieved, dynamic strain gauge data could be used to recover the dynamic input loading the truck experienced during operation.

Readings from strain gauges for unloaded conditions, as in Run 1, should be zero in theory, as this was the same loading condition as when the strain gauges were initially instrumented. This was not the case in the data, as non-zero strains were recorded by most of the strain gauges. These strains could be due to temperature effects, or the truck being stationary on a non-flat surface with wheels displaced non-uniformly inducing strains, etc. As shown in Figure 3.6 strains recorded in Run 1 were quite large in comparison with

readings from Run 2. In reality, data for Run 2 was recorded 100 seconds after Run 1. It was shifted in the graphs simply for illustration purposes. The net strain resulting from the addition of the payload was determined by subtracting averaged strains of Run 1 from the averaged recorded strains of Run 2. The same process was repeated to determine the net strain resulting from the addition of a payload in Run 3.

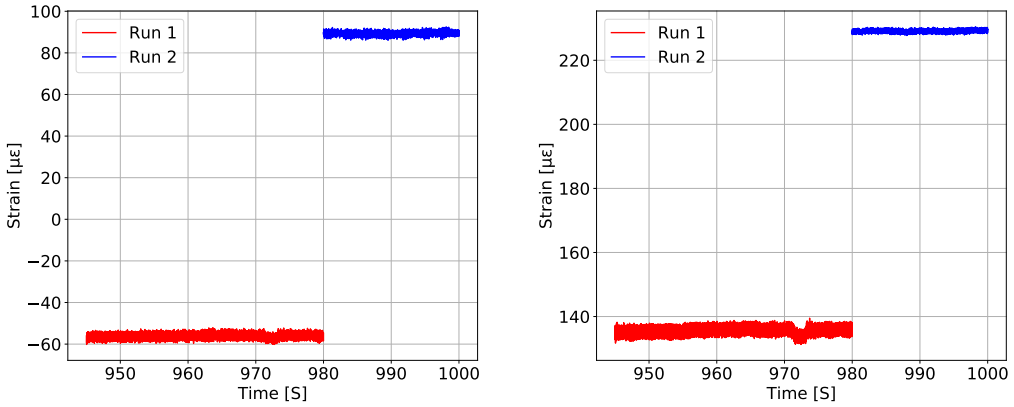

(a) Strains measured by strain gauge 15. (b) Strains measured by strain gauge 17.

Figure 3.6: Measured strains for Runs 1 and 2 by certain strain gauges.

Furthermore, some strain gauges were more sensitive than others to the deformations caused by the addition of a payload. Most of the instrumented strain gauges had very low sensitivity when the difference between strains measured for Run 1 and Run 2 was compared. Of the 39 useful strain gauges, the most sensitive 11 had a minimum difference between measured strains for Run 1 and Run 2 of 15 με. 15 με is still very small. Typically, the lower bound for strain measurements is 100 με. The strain gauges identified having the highest sensitivity were labelled: 12, 13, 14, 15, 16, 17, 23.2 (0°orientation), 27 (0°, 45°orientations), 28 (0°orientation) and 39 (45°orientation). Note that all strain gauges that were in full bridge configuration fixed to the chassis frame are included in this group. This is due to the full bridge configuration being four times more sensitive to deformations than the quarter bridge configurations as well as four times more robust against errors and noise (Agilent Technologies, 1999).

3.4 Finite element model

No engineering drawings or models were available for this truck. This lack of detailed technical information, complicated the development of a correspond-

ing FE model for the truck. General dimensions and measurements were taken of key components with measuring tapes and photos were provided. A general schematic with accompanying component measurements were provided as seen in Figure 3.7. These schematics were accompanied with measurement components as shown in Table A.1 of Appendix A.

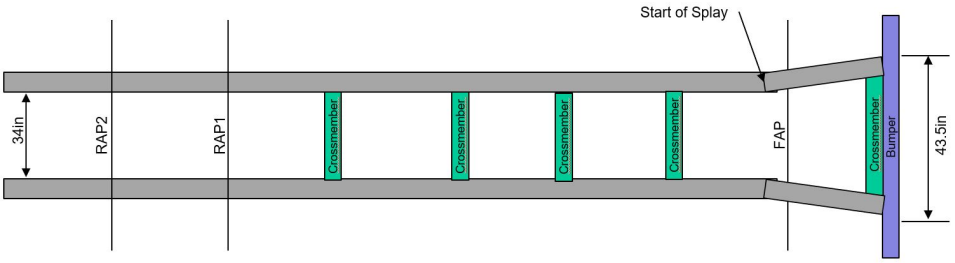

(a) Top view of the truck.

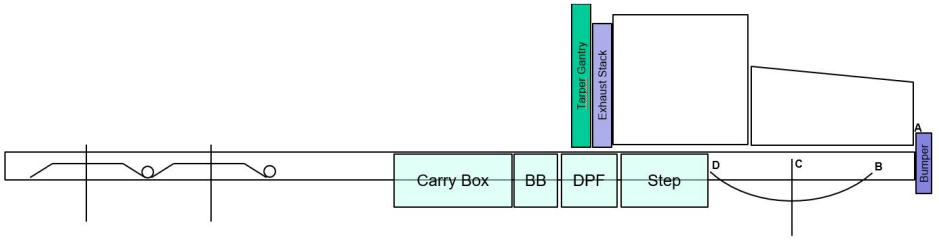

(b) Right hand side view of the truck.

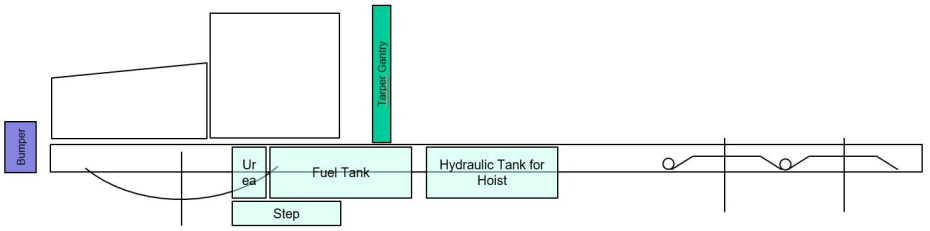

(c) Left hand side view of the truck.

Figure 3.7: Truck schematics as provided that indicate key component positions.

An FE model was developed on which experimentation and analysis could be done using NX version 11 by Siemens PLM Software. This model is shown in Figure 3.8 and consists of beam, shell and solid elements. All masses such as the fuel tank, battery box, engine, transmission, tarper gantry, carry box, cab, hydraulic tanks, and payload were modelled as point masses. Point masses were connected to the frame using RBE2 (pink), RBE3 (orange) and PBUSH (red) elements. These elements use a master and slave node system. Only a

single master node can govern over multiple slave nodes. For example the engine block was modelled as a point mass and was made the master node. The nodes that connect the master node (engine) to the frame would be the slaves. RBE2 elements were used where there were rigid connections between components, as they are infinitely stiff e.g. the bolted connections between brackets and cross members. Relative motion between slave nodes is constrained and all nodes are displaced in the same manner. RBE3 elements closely relate to RBE2 elements but do not have stiffness and allow the slave nodes to move relative to each other. They allow the transfer of loads without adding stiffness. For example, RBE3 connections were used to distribute the payload on the chassis on which it was resting. PBUSH elements are a spring type of element. Stiffness can be added in all 6 degrees of freedom to the element. This allows the user to free up motion of components connected with PBUSH elements by assigning the appropriate directional stiffness. These were used to simulate pivot motion at suspension attachment points.

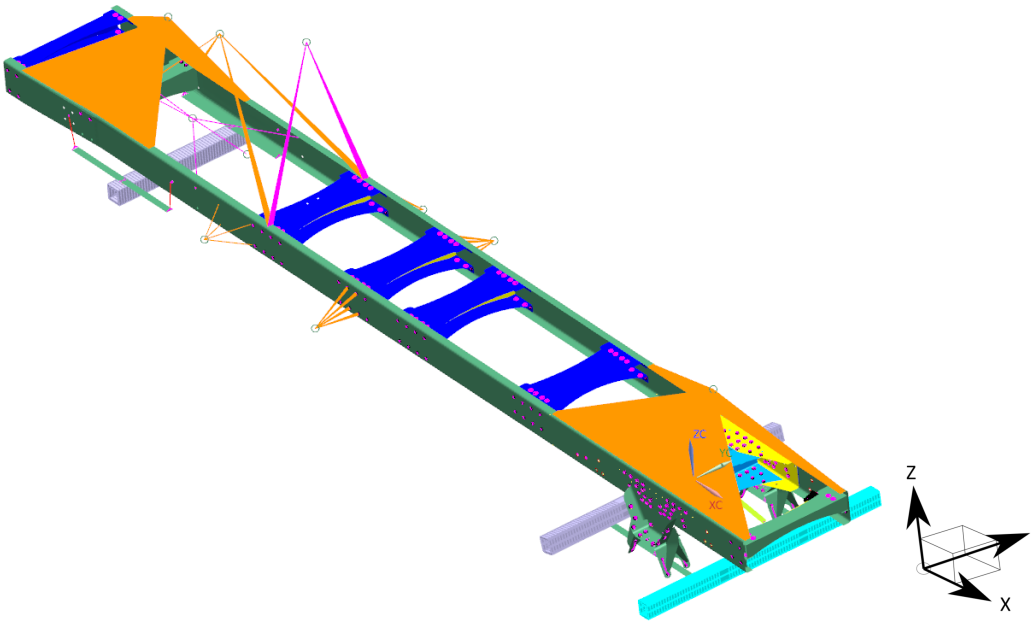

Figure 3.8: Finite element model developed to model the truck.

Frame components, cross members and brackets were modelled with rolled steel as material. These components have different thicknesses according to dimensions provided. The axle components were not the focus of this FE model and were only required to transfer loads from the boundary conditions to the chassis. Axles were simply modelled with beam elements.

Figure 3.9a depicts how the front suspension was modelled as well as how engine and transmission masses were mounted. This truck model utilises a

leaf spring suspension system as in Figure 3.9b to connect the front axle to the chassis. This setup was modelled using a shell plate element in bending to function as the spring component. PBUSH elements were used to simulate the front bracket and rear shackle by adjusting the stiffness appropriately for each degree of freedom. The pivot in Figure 3.9a only allowed rotation about the Y-axis and thus had no stiffness in the Y-rotational direction. The shackle element allowed translation in X-direction and rotation about Y-axis, while all other degrees of freedom were fixed.

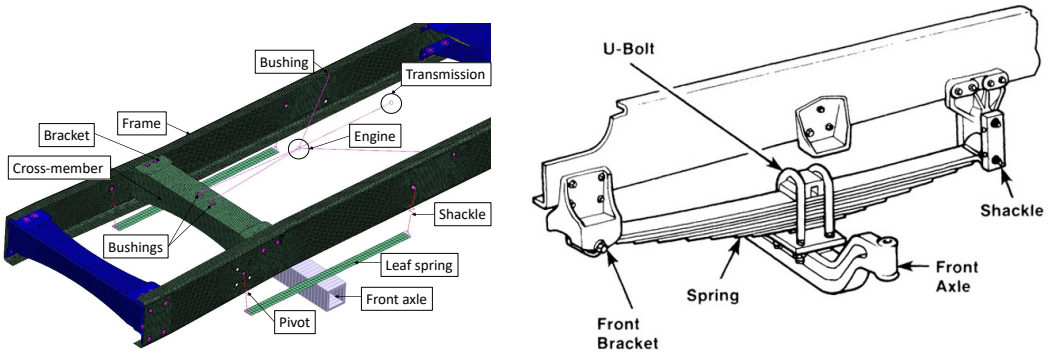

(a) Front suspension connections.

(b) Components of a leaf spring (SubbaReddy *et al.*, 2018).

Figure 3.9: Basic setup of the front leaf spring configuration.

Point masses simulating engine and transmission mass were mounted as in Figure 3.9a. RBE2 elements rigidly connected the engine and transmission components. PBUSH elements between RBE2 elements and the frame allowed small translation freedom in X-, Y-, and Z-directions of the engine and transmission at the cross-member and small translations in X- and Z-directions at frame connections. All other point masses were connected with RBE2 and RBE3s as seen in Figure 3.8. Spider bolted connections were used to connect all cross-members and brackets to the frame as shown in Figure 3.10. Spider connections used here consisted of 5/8 inch bolts modelled as a steel beam element with two spider RBE2 meshes connecting the bolt ends to the edge nodes of the holes.

The rear suspension is a camelback suspension system modelled as in Figure 3.11a. This setup involves an inverted leaf spring that connects to the frame at a single mounting point on either side of the chassis and with torque rods. Two axles are connected to the leaf ends. The torque rods transfer longitudinal and transverse torques experienced by the axles to the frame and cross-member. The longitudinal torque rod setup can be seen in Figure 3.11b. These rods were modelled as steel CBEAM elements. Again, these rods were not a focus point of the FE model as they were only required to transfer loads.

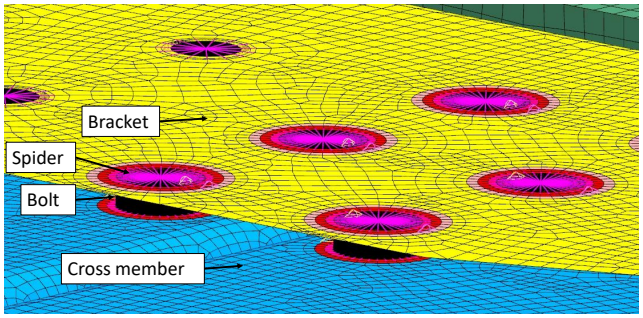

Figure 3.10: Spider bolted connection connecting cross members, brackets and frames.

Longitudinal rods were allowed to rotate about the Y-axis at cross-member attachment points. Transverse torque rods can rotate about the X-axis at frame attachment points. The front and rear suspension systems are modelled very simply in the FE models.

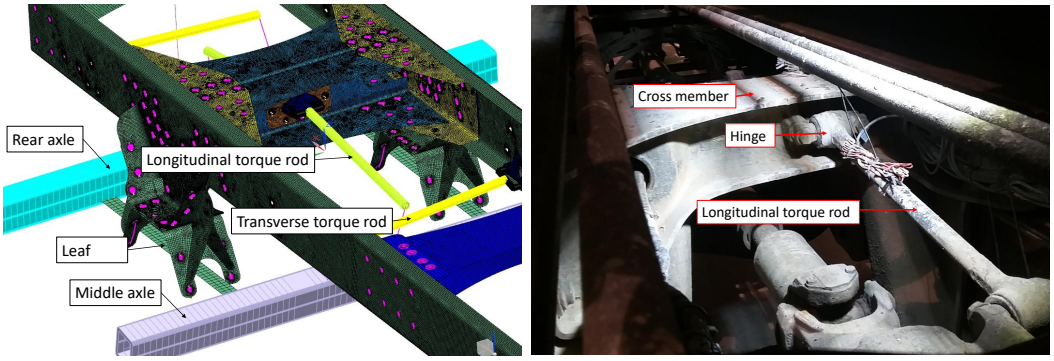

(a) Rear suspension connections. (b) Longitudinal torque rod of truck

Figure 3.11: Basic setup of rear camelback suspension configuration.

The purpose of these simplified front and rear suspension systems was to transfer reaction forces generated by boundary conditions to the chassis frame, and more accurately model the real world scenarios. The applied boundary conditions assume that the truck was resting on a perfectly flat and horizontal surface with no friction, which allowed the wheels to settle in plane as gravity was applied. Boundary conditions were applied to prevent rigid body modes and avoid generating unnecessary reaction forces.

3.5 Compensating for unaccounted masses

Although major mass contributing components were added into the model, some mass was still unaccounted for. With wheel force transducer data avail-

able, it was apparent that about 7000 kg of mass was unaccounted for. Unaccounted for components such as the drivetrain, lift mechanisms, cool packs etc. were lumped together as two compensating masses located at the front and rear of the FE model as shown in Figure 3.12.

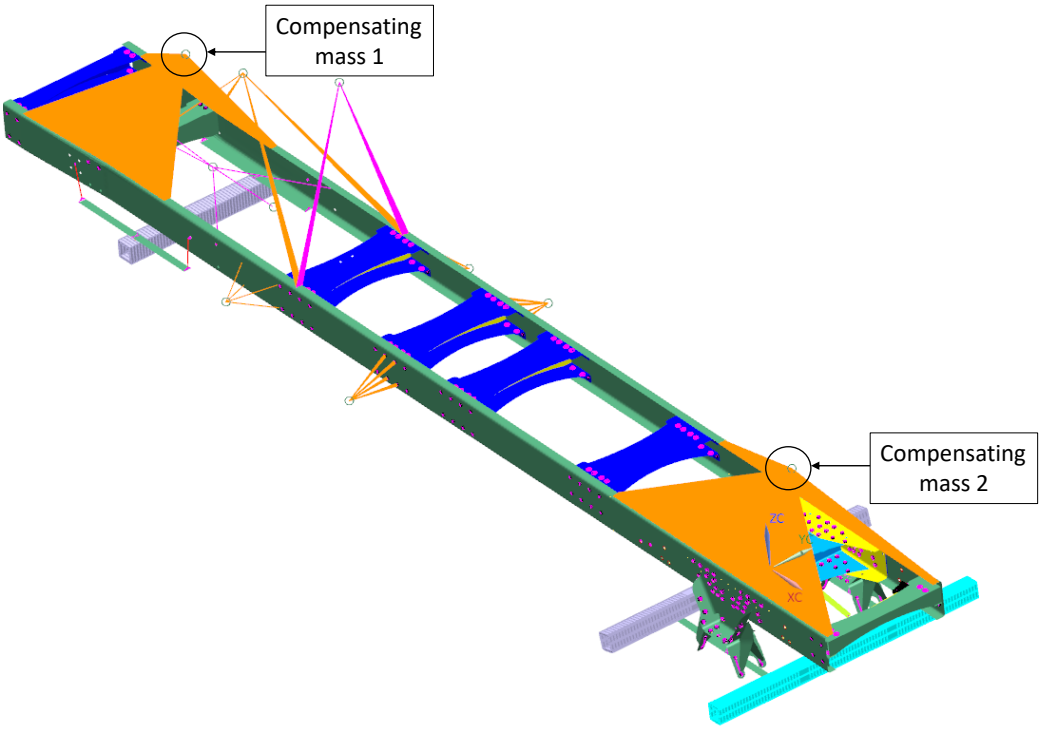

Figure 3.12: Locations and connections of compensating masses.

It was necessary to determine the appropriate size and position of these compensating masses. Genesis (Vanderplaats Research & Development, Inc., 2018) was used to perform a load optimisation. Genesis is a fully integrated FE analysis and optimisation tool (Vanderplaats Research & Development, Inc., 2011). It uses the Design Optimisation Tools (DOT) optimiser. DOT is a computer library that provides gradient-based optimisation functionality. Primarily, DOT is used to minimise or maximise a calculated quantity (objective function value) by automatically adjusting parameters while satisfying constraints. This process of finding the minimum or maximum objective value is accomplished by various numerical search methods. Linear and non-linear functions can be solved by DOT. Determination of the size and position of the compensating masses is a constrained optimisation problem.

Determination of compensating masses started with importing the FE model into Design Studio (Vanderplaats Research & Development, Inc., 2018) which is the graphical user interface for Genesis. The objective function was defined as minimising the differences between the measured (from the wheel force

transducer data for Run 1) and calculated wheel forces for the unloaded truck. By altering the compensating masses' position and size, the wheel forces could be matched within a 5% margin as seen in Table 3.2. Compensating masses 1 and 2 were estimated to be 1638.0 kg and 5157.8 kg respectively. Strain gauge data could not be used in this application because for an unloaded case, such as Run 1, strain gauges should theoretically have a zero reading.

Table 3.2: Comparison of vertical reaction forces at wheels with compensating masses as determined using wheel force transducer data.

Reaction force	**Measured value [kN]**	**Optimized with WFT data [kN]**	**% Error**
RR Z-reaction	18.220	17.580	3.5
RM Z-reaction	18.700	19.634	5.0
RF Z-reaction	26.220	25.280	3.6
LF Z-reaction	24.530	25.267	3.0
LM Z-reaction	19.660	19.921	1.3
LR Z-reaction	18.860	18.654	1.1

Chapter 4

Rigid body dynamics experiment

In order to demonstrate the validity of the process of rigid body dynamics for load recovery, a controlled experiment was constructed to test developed equations and processes. A simple spring mass system seen in Figure 4.1a closely resembles a quarter truck suspension model as in Figure 4.1b, minus the dampers. The initial application of rigid body dynamics processes to the simple experiment, where all system parameters are known, revealed potential expectations for modelling the real truck. Instrumentation on the simple system recorded the same data types as were available for the actual truck, i.e. accelerations and input forces.

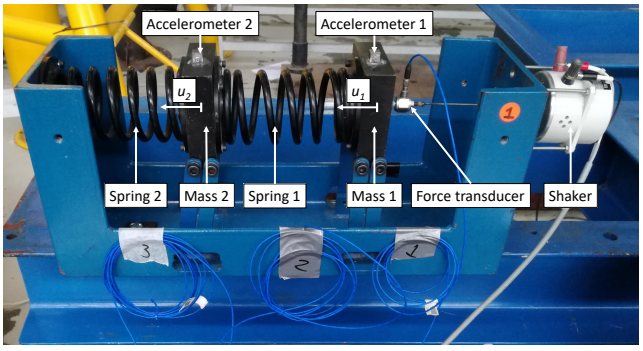

(a) Simple spring mass system.

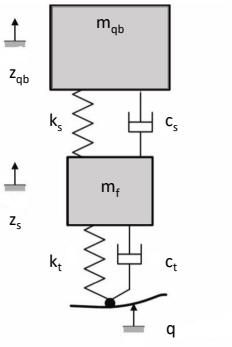

(b) Two degrees of freedom quarter truck model

Figure 4.1: Simple spring mass system experiment and a quarter truck model.

4.1 Derivation of required equations

Firstly, the equations of motion for the system were derived using Equation 2.1. There are no dampers in the system. This experiment was setup to minimise

the friction using ball bearings at the supports. Friction from these supports were seen as negligible and the system was modelled without any damping, with Equation 2.1 reducing to

$$\boldsymbol{M}\ddot{\boldsymbol{u}} + \boldsymbol{K}\boldsymbol{u} = \boldsymbol{p} \tag{4.1}$$

where $\boldsymbol{M}$, $\boldsymbol{K}$, $\boldsymbol{u}$ and $\boldsymbol{p}$ are respectively,

$$\boldsymbol{M} = \begin{bmatrix} m_1 & 0 \\ 0 & m_2 \end{bmatrix} \tag{4.2}$$

$$\boldsymbol{K} = \begin{bmatrix} k_1 & -k_1 \\ -k_1 & k_1 + k_2 \end{bmatrix} \tag{4.3}$$

$$\boldsymbol{u} = \begin{bmatrix} u_1 & u_2 \end{bmatrix}^T \tag{4.4}$$

$$\boldsymbol{p} = \begin{bmatrix} p_1 & 0 \end{bmatrix}^T \tag{4.5}$$

where m_1 and m_2 are mass 1 and mass 2, k_1 and k_2 are the stiffness of springs 1 and 2, u_1 and u_2 are the horizontal displacements of masses 1 and 2 respectively, and p_1 is the input loading on mass 1.

The system parameters, such as spring stiffness and the masses of m_1 and m_2, were known for this setup. In most real word scenarios these parameters are not available. This was the case for the truck model that was analysed in the following chapter. This prompted the development of a parameter identification methodology to identify these system parameters. The developed methodology was also tested using the simple spring mass experiment.

With the acceleration available for each mass as well as the input loading applied by the shaker, the equations of motion provided by Equation 4.1 could be substituted into Equation 2.2 to produce an objective function. The system parameters (k_1, k_2, m_1, m_2) were identified by finding the minimum of this objective function. Matlab's particle swarm optimiser was used to optimise this objective function and determine the system parameters.

The focus in this thesis was to investigate alternative approaches of load recovery that do not use force transducer data. Ideally the process of system parameter identification with the end goal of load recovery would be achieved

using only accelerometer data. Therefore, two different parameter identifications were conducted: firstly using both force and acceleration data, and secondly using only acceleration data. With force data available, both equations of motion describing masses 1 and 2 could be used. For the second parameter identification only the equation of motion describing mass 2 could be used as the input loading on mass 1 would be unknown. In order to make the parameter identifications possible, the displacements of both masses over time were required. Mass displacements were acquired by integrating acceleration signals twice.

4.2 Integration problem

Integration of sampled time signals is a common task in signal processing. Various methods have been investigated to accomplish this. The displacement histories of masses 1 and 2 are required to perform the system parameter identification. A relatively straightforward method was implemented to determine displacement signals from recorded acceleration data. The system shown in Figure 4.1a was excited with a simple sinusoidal forcing function:

$$F = A\sin(2\pi ft) \tag{4.6}$$

where A is the amplitude (N), f is the frequency (Hz), and t the time-step (s). Data sets were recorded where f was constant at: 5, 8, 15 and 30 Hz. The integration method outlined in this section exploited the fact that f was held constant for the different data sets. Integration in this manner was a simple division by a constant in the frequency domain, due to f being constant.

The method involved integration in the frequency domain by firstly using a discrete Fourier transform (DFT), then dividing by the frequency, $i\omega$, followed by an inverse DFT (IDFT) back to the time domain (Brandt and Brinker, 2014). This approach outperforms traditional integration methods, such as the trapezoidal rule, in terms of accuracy with little extra effort.

This method of integration by a long DFT requires that the Fourier transform of the full signal be possible without reaching memory limitations. This is rarely a problem with modern computing capabilities. To avoid anti-aliasing, the time signal should be detrended and zero-padded before computing its DFT. Taking a sampled input signal $x(n), n = 0, 1, \ldots, L-1$, sampled at a sampling frequency f_s, a $2L$ size DFT is computed by

$$X(k) = \sum_{n=0}^{2L-1} x_z(n)e^{-i2\pi kn/(2L)}, \quad k = 0, 1, \ldots, L-1 \tag{4.7}$$

where $x_z(n)$ is the zero-padded time signal with L values $x(n)$ followed by L zeros. Only the positive frequencies are computed in Equation 4.7. Next, the integration operator is computed by

$$H_i(k) = \begin{cases} 1/i\omega_k, & k = 1, \ldots, L \\ 0, & k = 0 \end{cases} \tag{4.8}$$

since division by zero is not possible. Frequencies in Equation 4.8 are the DFT frequencies $\omega_k = 2\pi k f_s/(2L)$. Integration in the frequency domain is accomplished with the product $Y(k) = X(k)H(k)$. Before the inverse transform can be computed, $Y(k)$ should be extended with an odd imaginary part and an even real part for the negative frequencies, by defining

$$Y(L+k) = Y^*(L-k), \quad k = 1, 2, \ldots, L-1 \tag{4.9}$$

where the complex conjugate is represented by *. Ultimately, integral $y(n)$ of the original signal $x(n)$ in the time domain can be computed with the IDFT

$$y(n) = \frac{1}{2L} \sum_{k=0}^{2L-1} Y(k) e^{i2\pi nk/(2L)}, \quad n = 0, 1, \ldots, L-1 \tag{4.10}$$

It is best practice to detrend $y(n)$ in order to correct for errors that can occur due to leakage in the DFT/IDFT processes. This method would also be applicable to data gathered at non-constant frequencies, but the integration operator would no longer be constant.

4.3 Experimental setup parameter identification

Firstly, the identification process was conducted using recorded acceleration and force data. Matlab's particle swarm optimiser was utilised to solve for the objective function's minimum by identifying the experimental setup's system parameters. A single set of field data was not sufficient to solve for the unknown model parameters as there were too many possible solutions that satisfied the objective function (local minima). Two objective functions were set up using 2 different sets of field data. For each data set the forcing function was applied using a different constant frequency. A unique solution was produced when data sets were captured with the forcing function applied at 8 and 30 Hz. Estimated system parameters and their accuracies are shown in

Table 4.1. The objective function could be expanded to use all the datasets, but it was deemed unnecessary as the accuracy with which parameters were identified was sufficient. The actual values of Mass 1 and 2 were determined by weighing each mass. The spring constants of the two springs were determined by measuring the change in spring length due to the addition of a known mass that compressed it. With the original and deformed spring length known the spring constants were calculated.

Table 4.1: Accuracy of system parameter identification for the experimental setup using force and acceleration data.

Parameter	**Actual value**	**Identified value**	**% Error**
Mass 1 [kg]	3.350	3.346	0.1
Mass 2 [kg]	3.400	3.071	9.7
Spring constant 1 [kN/m]	20.500	21.062	2.7
Spring constant 2 [kN/m]	20.500	20.474	0.1

High accuracy was achieved and the system parameters were identified with minimal error. Error was attributed to the omission of friction/damping in the equations of motion. The input loading on m_1 was calculated by substituting the identified parameters and measured accelerations into Equation 4.1. Plots displaying the fit between the recorded and calculated input loading for the two datasets captured at 8 and 30 Hz are shown in Figure 4.2 as a measure of the accuracy of the obtained parameters. A spline was fitted over the results produced with the forcing function applied at 30 Hz for better visualisation.

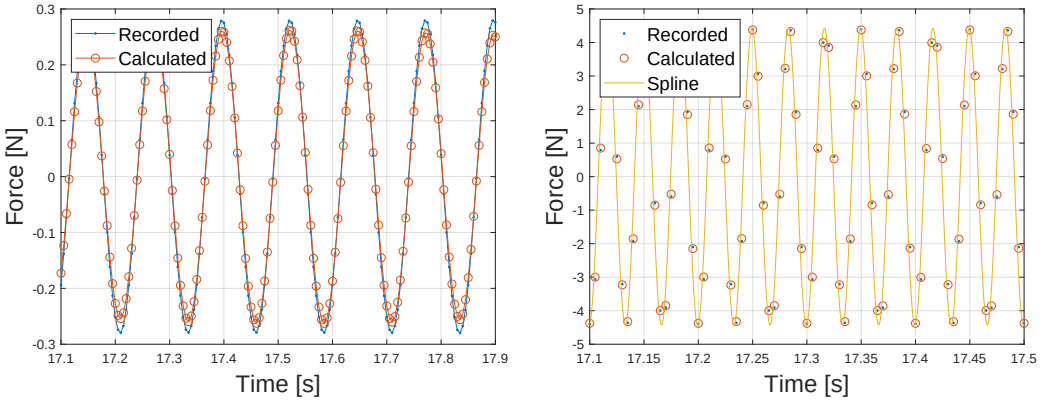

(a) 8 Hz (b) 30 Hz

Figure 4.2: Correlation between recorded and calculated force signals using identified system parameters.

The results shown in Figures 4.2 and 4.3 proved that the parameter identification is reliable and applicable to spring mass systems. With all the system parameters known, the input loading experienced by the frame of the experimental setup could be recovered accurately with

$$F_{frame} = k_2 u_2 \tag{4.11}$$

where F_{frame} is the force experienced by the frame.

Next, the system parameter identification process was repeated using only accelerometer data. For this scenario only m_2, k_1 and k_2 could be approximated as the input loading on m_1 would be 'unknown'. An interesting phenomenon occurred. When parameters were estimated the true parameter values could not be identified. Over 10 independent parameter identifications the same minimum objective function value was reached, but with different parameter values satisfying the objective function as shown in Table 4.2.

Table 4.2: Estimated system parameters for 10 independent parameter identification optimisations using only acceleration data.

Optimisation	$\boldsymbol{m_2}$ [kg]	$\boldsymbol{k_1}$ $\left[\frac{\text{kN}}{\text{m}}\right]$	$\boldsymbol{k_2}$ $\left[\frac{\text{kN}}{\text{m}}\right]$	$\frac{\boldsymbol{k_1}}{\boldsymbol{m_2}}$ $\left[\frac{\text{kN}}{\text{m·kg}}\right]$	$\frac{\boldsymbol{k_2}}{\boldsymbol{m_2}}$ $\left[\frac{\text{kN}}{\text{m·kg}}\right]$	$\frac{\boldsymbol{k_1}}{\boldsymbol{k_2}}$
1	41.84	249.85	250.51	5.97	5.99	1.0
2	3.82	22.83	22.89	5.97	5.99	1.0
3	1.22	7.29	7.31	5.97	5.99	1.0
4	7.05	42.08	42.19	5.97	5.99	1.0
5	6.34	37.85	37.95	5.97	5.99	1.0
6	9.06	54.11	54.26	5.97	5.99	1.0
7	42.02	250.97	251.63	5.97	5.99	1.0
8	13.73	82.00	82.21	5.97	5.99	1.0
9	12.30	73.49	73.67	5.97	5.99	1.0
10	1.08	6.46	6.48	5.97	5.99	1.0

These parameters consistently held the same relationship to one another. If a larger mass was identified, the spring constant was adjusted to account for the higher mass, balancing the objective function. Thus there are multiple local minima for this problem, all at the same global minimum. There were many possible solutions to fit the data because the signals captured were accelerations due to the same forcing function being excited at different frequencies and amplitudes. Using these estimated parameters with Equation 4.11 to recover the input loading would produce inaccurate results. If a single system

parameter such as m_2, k_1 or k_2 were known, all others could be determined using the inter-parameter relationships.

4.4 Multi-body dynamic simulation

The spring mass system was modelled as a multi-body dynamic system. For this to be possible it was assumed that all system parameters were available and known in order to set up the model as described with Equation 4.1. The process entails solving Equation 4.1 as a differential equation using either force or acceleration as an input. Matlab's ode45 function was used to solve the differential equations. Identified system parameters in Table 4.1 and a dataset captured where f and A of the forcing function were equal to 5 Hz and 1.05 N respectively was used. This dataset did not form part of the parameter identification process.

First, the differential equations were solved using the force data as an input. This produced approximates for the displacement and velocity signals of masses 1 and 2. Initial conditions (mass position and velocity) were known. Force data was smoothed using linear interpolation. The calculated displacement signals for m_1 and m_2 are shown in Figure 4.3.

The double-integrated experimental acceleration data signals were plot alongside the solved displacement signals for comparison. Using these results the input loading on the setup's frame could be determined using Equation 4.11. This process does not require acceleration measurements as long as the system parameters are known and available.

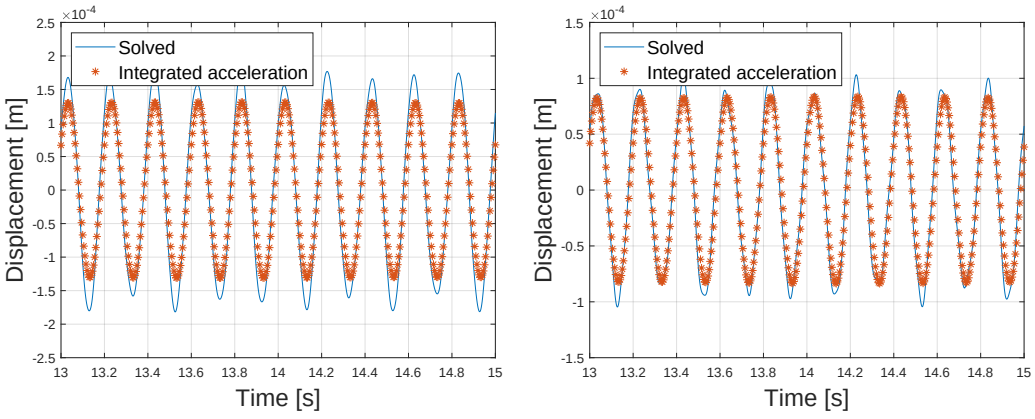

(a) Mass 1 displacement

(b) Mass 2 displacement

Figure 4.3: Displacement signals produced by multi-body dynamic simulation using force data.

Next, the differential equations were solved using only the acceleration data of m_1 as an input. Thus, the force data was assumed to be unavailable or unknown. This produced calculated displacement and velocity signals of m_2. The calculated displacement signal m_2 is shown in Figure 4.4a. Once again, the double-integrated experimental acceleration data signal was plotted alongside the solved displacement signals for comparison.

Substituting the solved displacement signal of m_2 alongside m_1's acceleration data into Equation 4.1, the input loading experienced by m_1 can be solved for, as shown in Figure 4.4b. The input loading was solved for accurately in terms of the amplitude and period. Deviations between the solved input loading and the recorded input loading were attributed to the use of identified parameters that contained errors as shown in Table 4.1. From these results it was clear that this process is very sensitive to the accuracy with which the dynamic model was set up. Small errors present in the parameters used caused noticeable error in recovered signals.

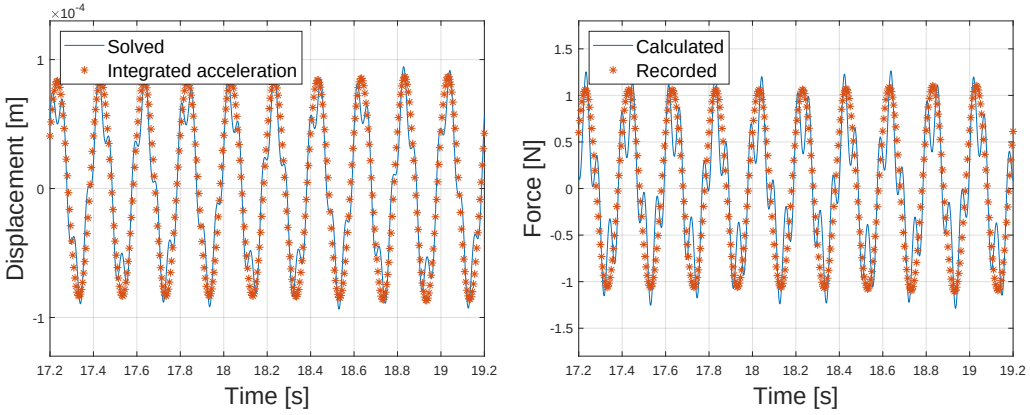

(a) Mass 2 solved displacement.

(b) Input loading on m_1.

Figure 4.4: Multi-body dynamic simulation results using m_1's acceleration data.

In conclusion, it is possible to recover the input loading that the spring mass system experienced using only acceleration data captured at m_1 using multi-body dynamic simulation. This approach requires that all the parameters of the spring mass system must be known.

Alternatively, if a single parameter, such as m_2, is known and the accelerations of masses 1 and 2 are recorded, a parameter identification could be performed. The reaction force experienced by the experimental setup's frame could then be determined. The input loading induced by the shaker, however, would not

be obtainable, as m_1 cannot be identified with parameter identification using only acceleration data.

Chapter 5

Truck multi-body dynamic simulation

The input loading a truck experiences while in operation can be determined through multi-body dynamic simulation. This process relies on the derivation of an equivalent mathematical model of the truck. Generation of such a model requires that the system parameters be known, including the chassis' mass, suspension stiffness and damping, etc. For the truck in question, none of these parameters were known. Drehmer *et al.* (2015) used the same processes as in this chapter to optimise suspension parameters of a vehicle for ride comfort. Here, instead, these methods will be employed to identify the unknown system parameters.

5.1 Quarter truck model

5.1.1 Background

A classic quarter truck model is shown in Figure 5.1. Despite being the simplest of the truck models (half and full truck models are also possible), it is very popular in suspension research and has a couple of advantages over more complex models (Maher and Young, 2011). These advantages include:

- Having fewer system parameters.
- Being a single input system that is less computationally intensive.
- Being relatively quick and easy to set up compared to more detailed models.

A cost of the quarter truck model's simplicity is that it does not account for the roll and pitch motion of the truck body. The parameters in Figure 5.1 are defined as: the truck quarter body mass m_{qb}; the front suspension unsprung

mass m_f; the suspension stiffness and damping are k_s and c_s respectively; the tyre stiffness and damping are k_t and c_t respectively; z_s and z_{qb} are the displacement of the unsprung suspension mass and the quarter truck body mass respectively. Lastly, the road profile is q. Wheels are modelled as having independent suspension. Thus, the unsprung mass accounts for a single tyre, wheel, suspension knuckle, shock absorber and a contributing mass.

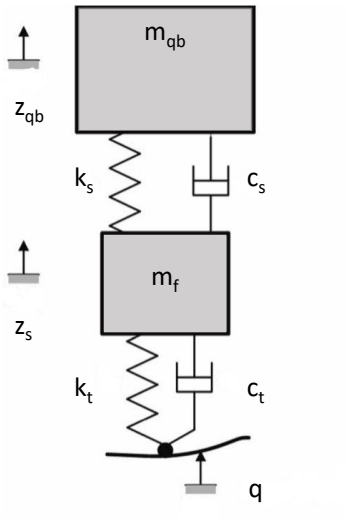

Figure 5.1: Two degree of freedom quarter truck model (Alvarez-Sánchez, 2013).

Neglecting damping, the quarter truck model closely resembles the simplified experiment conducted in Chapter 4. The same parameter identification procedures were applied here. Once again load recovery was done using different data sets, one using force data alongside acceleration data and one without the availability of force data using only acceleration data. Two quarter truck models were set up modelling the front and rear quarters of the truck.

5.1.2 Front quarter truck model

The quarter truck model shown in Figure 5.1 relies on the availability of the road profile. The road profile was unavailable in the dataset used in the current study and the model was modified to use the input loading from the road that was measured with wheel force transducers. Figure 5.2 presents the modified model for the front quarter truck where F_f is the wheel forces measured with the front wheel force transducers.

Equations describing the motion of m_{qb} and m_f were derived using Newton's second law of motion that reduce to:

$$m_{qb}\ddot{z}_{qb} = -k_s(z_{qb} - z_s) - c_s(\dot{z}_{qb} - \dot{z}_s) \tag{5.1}$$

$$m_f\ddot{z}_s = F_f + k_s(z_{qb} - z_s) + c_s(\dot{z}_{qb} - \dot{z}_s) \tag{5.2}$$

where it was assumed that $z_{qb} > z_s$ so that the suspension is in tension.

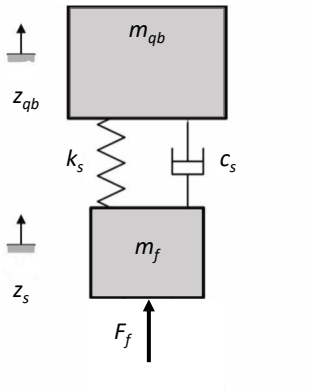

Figure 5.2: Two degrees of freedom front quarter truck model.

5.1.3 Rear quarter truck model

The truck analysed in this thesis has a middle and rear axle. The quarter truck model in Figure 5.2 was modified to account for the middle and rear axles. Figure 5.3 provides the three degrees of freedom rear quarter truck model. Parameters in Figure 5.3 are defined as: rear quarter body mass m_{rqb}; middle and rear suspension unsprung masses m_m, m_r; middle and rear suspension vertical stiffness k_{sm}, k_{sr}; middle and rear suspension vertical damping c_{sm}, c_{sr}; rear quarter body mass' vertical displacement z_{rqb}; middle and rear unsprung mass displacements z_{sm}, z_{sr} and lastly the wheel forces transmitted to the middle and rear unsprung masses F_m and F_r.

Equations describing the motion of m_{rqb}, m_m and m_r were derived in the same manner for the front quarter truck model:

$$m_{rqb}\ddot{z}_{rqb} = -k_{sm}(z_{rqb} - z_m) - c_{sm}(\dot{z}_{rqb} - \dot{z}_m) - k_{sr}(z_{rqb} - z_r) - c_{sr}(\dot{z}_{rqb} - \dot{z}_r) \tag{5.3}$$

$$m_m\ddot{z}_m = F_m + k_{sm}(z_{rqb} - z_m) + c_{sm}(\dot{z}_{rqb} - \dot{z}_m) \tag{5.4}$$

$$m_r\ddot{z}_r = F_r + k_{sr}(z_{rqb} - z_r) + c_{sr}(\dot{z}_{rqb} - \dot{z}_r) \tag{5.5}$$

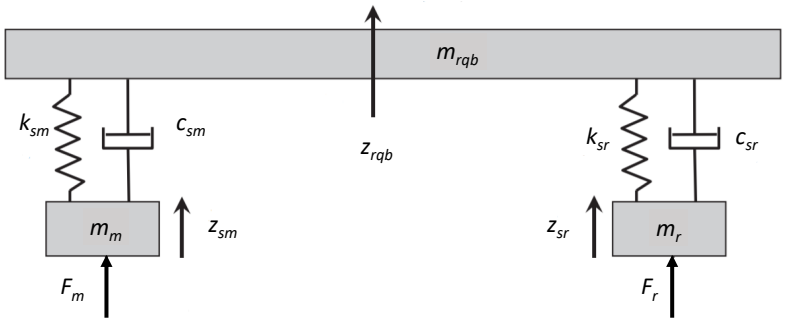

Figure 5.3: Three degrees of freedom rear quarter truck model.

5.2 Data post processing

The provided field data sets were unfiltered and contained noise. Noise would have to be removed to conduct sufficiently high quality analysis. Measured field data signals were converted from the time domain to the frequency domain with a Fast Fourier Transform (FFT) in Matlab. This made it possible to analyse the frequency content of the various field data signals. The FFT of accelerometer 1 positioned on the front left of the truck's chassis is shown in Figure 5.4. The data that is displayed is a segment of the dataset Section B described in Table 3.1 that was recorded while the truck was driving off-road at a landfill site.

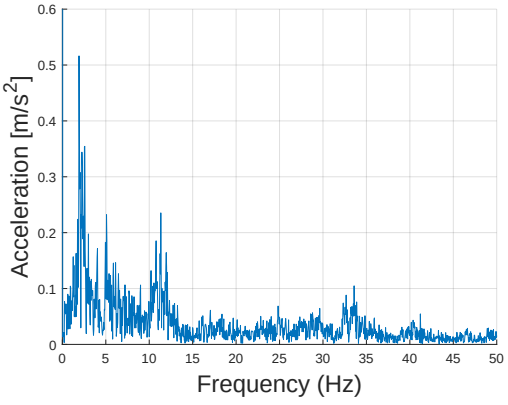

Figure 5.4: Fast Fourier transform of acceleration signal recorded by accelerometer 1.

From Figure 5.4 it is clear that the majority of the recorded signal density was at lower frequencies. A bandpass filter was selected as the appropriate filter to remove unwanted noise. The bandpass frequency range for the data captured by accelerometer 1 was selected as 1-10 Hz. A comparison between the original and filtered signals are shown in Figure 5.5. Note that the original signal was detrended to remove static offset due to gravity.

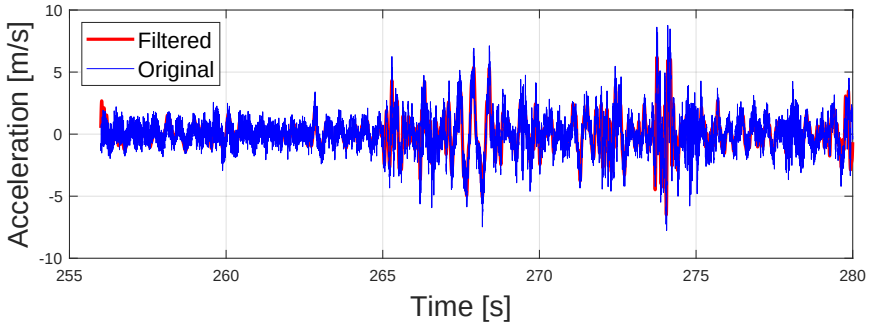

(a) Full length of data signal used in analyses.

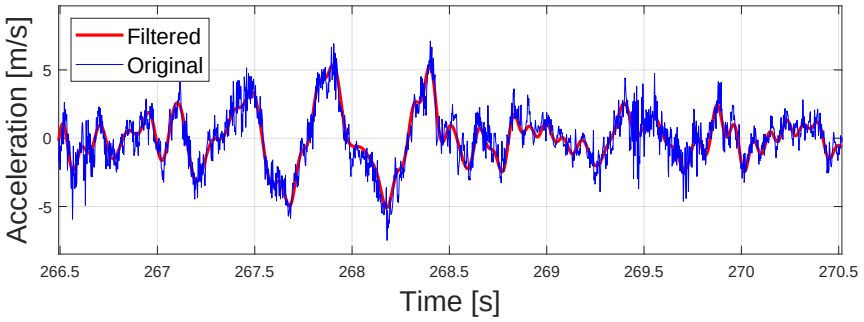

(b) Snippet between 266.5 and 270.5 s

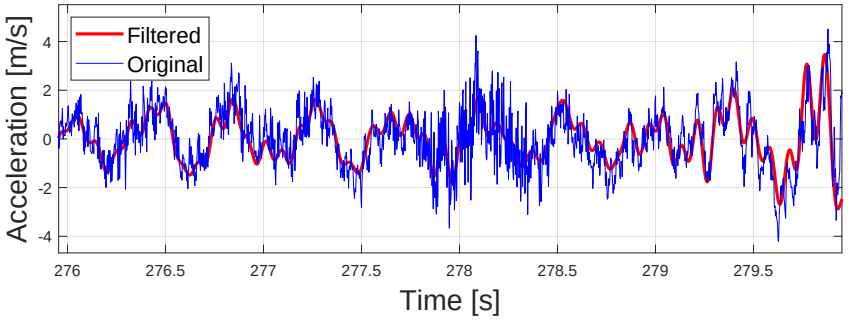

(c) Snippet between 276 and 280 s

Figure 5.5: Original and bandpass filtered accelerometer 1 data.

The filtered signal is much smoother than the original signal, whilst still capturing the general trend of the data. The same methods were applied to all

the other signals, such as the wheel force and wheel acceleration signals, to identify the appropriate bandpass frequency ranges to use for their respective bandpass filters. A complete list of the bandpass filters used for other data signals is provided in Appendix B. Comparison plots of the original and filtered signals are also provided.

5.3 System parameter identification using force and acceleration data

The same system parameter identification methods from Chapter 4 were applied to the front and rear quarter truck models. Here both sets of acceleration and force data were utilised.

5.3.1 Front quarter truck model parameter identification

Two quarter truck models were developed for the front left and front right quarters of the truck. Instrumentation positioned on the truck as seen in Figure 3.2 captured the wheel and chassis accelerations and the wheel forces experienced by the wheels from the road. With this data available for the left and right sides of the truck, the accuracy of parameter estimation and load recovery could be compared as the results should be similar.

Large data sets were available, but using all of the data would increase simulation times without the added benefit of higher accuracy. A segment of Section B from Table 3.1 was identified and used for parameter identification. This segment was 64 seconds long and contained 32000 data points. This was deemed sufficient for accurate parameter identification, based on the observation that by using more data points, the parameters that were identified altered minimally.

A modified version of Equation 2.2 was used as the objective function for the system parameter identification. The mass component in Equations 5.1 and 5.2 was shifted to the right hand side so that $\hat{\ddot{z}}_{qb}$ and $\hat{\ddot{z}}_s$ remain on the left hand side. The SSE of Equations 5.1 and 5.2 were normalised and combined in the full objective function. Normalisation was added into the SSE to balance the weight of Equations 5.1 and 5.2 so that the PSO does not favour one or the other equation. If, for example, Equation 5.1 contributed much more to the SSE than Equation 5.2. The PSO would determine optimal parameters to satisfy Equation 5.1, regardless if these parameters were non-optimal for Equation 5.2. Finally, the full objective function could be written as:

$$SSE = \sum_{i=1}^{n} \frac{\left(\ddot{z}_{qb}(i) - \hat{\ddot{z}}_{qb}(i)\right)^2}{\max\left(|\ddot{z}_{qb} - \hat{\ddot{z}}_{qb}|\right)} + \sum_{i=1}^{n} \frac{\left(\ddot{z}_{s}(i) - \hat{\ddot{z}}_{s}(i)\right)^2}{\max\left(|\ddot{z}_{s} - \hat{\ddot{z}}_{s}|\right)}, \tag{5.6}$$

where n is the number of sampling points. Once again Matlab's particle swarm optimiser was used to identify the appropriate system parameters that minimise the sum of square of errors calculated with Equation 5.6. Twenty-five independent optimisations for the two models were conducted. The final objective function values were compared and the best model parameters were selected. Table 5.1 provides the identified system parameters after optimisation.

Table 5.1: Identified parameters for the front left and front right quarter truck models.

Parameter	**Left side**	**Left parameter** m_{qb}	**Right side**	**Right parameter** m_{qb}
m_{qb} [kg]	3215.7	1.00	3578.5	1.00
m_f [kg]	1489.2	0.46	1370.6	0.38
c_s [Ns/m]	5615.6	1.75	5067.9	1.42
k_s [N/m]	487581.0	151.62	573524.9	160.26

The test vehicle was a 2012 model with an odometer reading of 358,000 mi (572,800 km) at purchase. It was understandable that the suspension on the left and right side did not behave exactly symmetrically, due to wear and tear over years of operation. The front left and right force transducers measured respective averages of 32356 N and 29164 N for the dataset used in analyses. This translates to 3298.2 kg and 2972.9 kg supported by the front left and right suspensions. When comparing these values with the identified left and right m_{qb} values, the parameter identification was reasonably accurate, considering the simplicity of the quarter truck models.

The wheel forces could be estimated using a rearranged version of Equation 5.2:

$$F_{est} = -m_f \ddot{z}_s + k_s(z_{qb} - z_s) + c_s(\dot{z}_{qb} - \dot{z}_s) \tag{5.7}$$

where F_{est} is the estimated wheel force using the identified model parameters. Correlation plots between the recorded and estimated wheel forces for the front left and right wheels are shown in Figure 5.6. Despite the simplicity of the quarter truck models, the wheel forces were estimated accurately. If the sum of forces experienced by the chassis ($\sum F_{chassis}$) were the only item of interest, it could be determined with either:

$$\sum F_{chassis} = m_{qb}\ddot{z}_{qb}, \tag{5.8}$$

or

$$\sum F_{chassis} = -k_s(z_{qb} - z_s) - c_s(\dot{z}_{qb} - \dot{z}_s), \tag{5.9}$$

which are rearranged versions of Equation 5.1. These equations calculate the input loading using either the frame acceleration data and a m_{qb} estimate or using the suspension parameters and both wheel and frame integrated acceleration signals. The quarter truck models assume that the suspension attaches to the frame at a single point. In reality, the suspension attaches at two points as shown in Figure 3.9b. Thus, $\sum F_{chassis}$ will be divided into two components that are absorbed by the front bracket and rear shackle.

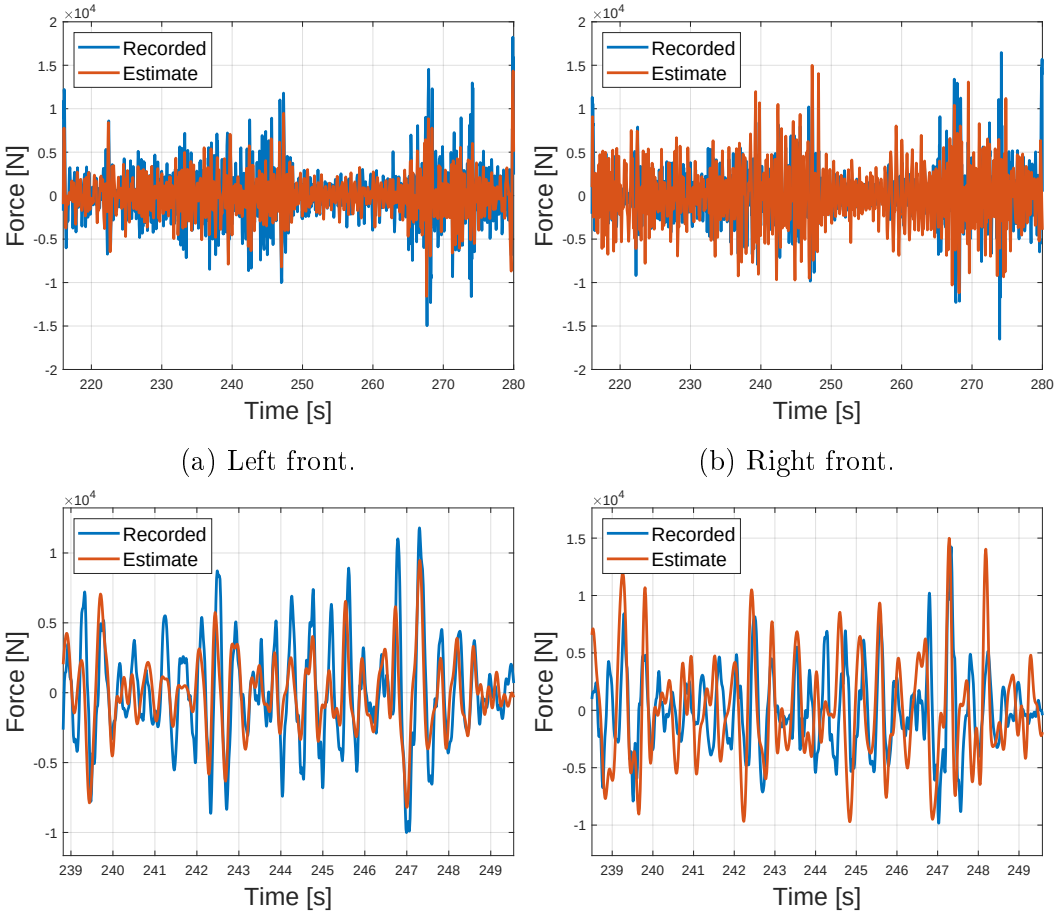

(a) Left front.

(b) Right front.

(c) Left zoomed.

(d) Right zoomed.

Figure 5.6: Correlation between recorded and estimated wheel forces for the left and right front wheels.

5.3.2 Rear quarter truck model parameter identification

Next, parameter identification was applied to the rear quarter truck model with the ultimate goal of load recovery. The wheel force transducer on the right rear wheel did not record data during operation on 28/02/2018. As a result, the right rear wheel's acceleration and force data was unavailable. Thus, only the left rear quarter of the truck could be modelled. The transducer captured data for the other datasets (static load cases) that were recorded on other days.

A segment of data from Section B described in Table 3.1 was used for parameter identification. This was the same segment as the segment used previously in Section 5.3.1. The same approach was used to set up the objective function to be optimised as in Section 5.3.1. Acceleration components of Equations 5.3, 5.4 and 5.5 were isolated, normalised and added to Equation 2.2 to produce the objective function:

$$SSE = \sum_{i=1}^{n} \frac{\left(\ddot{z}_{rqb}(i) - \hat{\ddot{z}}_{rqb}(i)\right)^2}{\max\left(|\ddot{z}_{rqb} - \hat{\ddot{z}}_{rqb}|\right)} + \sum_{i=1}^{n} \frac{\left(\ddot{z}_{sm}(i) - \hat{\ddot{z}}_{sm}(i)\right)^2}{\max\left(|\ddot{z}_{sm} - \hat{\ddot{z}}_{sm}|\right)} + \sum_{i=1}^{n} \frac{\left(\ddot{z}_{sr}(i) - \hat{\ddot{z}}_{sr}(i)\right)^2}{\max\left(|\ddot{z}_{sr} - \hat{\ddot{z}}_{sr}|\right)}. \tag{5.10}$$

In Equation 5.10 there were 7 parameters that needed to be identified through optimisation. Once again 25 independent optimisations with Matlab's particle swarm optimiser were conducted. The best system parameters were identified and used in the quarter truck model to simulate most accurately the quarter truck's response. The best parameters were those that produced the smallest objective function value. Identified parameters and their relationship with m_{rqb} are shown in Table 5.2.

Table 5.2: Identified parameters for the left rear quarter truck models.

Parameter	**Optimised value**	**Normalised value** $\left[\frac{\textbf{Value}}{m_{rqb}}\right]$
m_{rqb} [kg]	4167.5	1.00
m_m [kg]	1298.7	0.31
m_r [kg]	1366.5	0.33
c_{sm} [Ns/m]	5445.1	1.31
c_{sr} [Ns/m]	0	0
k_{sm} [N/m]	814518.9	195.45
k_{sr} [N/m]	1469354.0	352.58

The left middle and rear wheel force transducers measured that the average wheel forces experienced were 22907.9 N and 22959.8 N respectively. This

translates into a total mass of 4675.6 kg supported by the left middle and rear wheels. Comparing this value to the identified m_{rqb} value gives a reasonably accurate parameter identification considering the simplicity of the model. Estimated wheel forces were calculated with Equation 5.7 using the appropriate model parameters. The correlation between recorded and estimated wheel forces for the middle and rear wheels is shown in Figure 5.7.

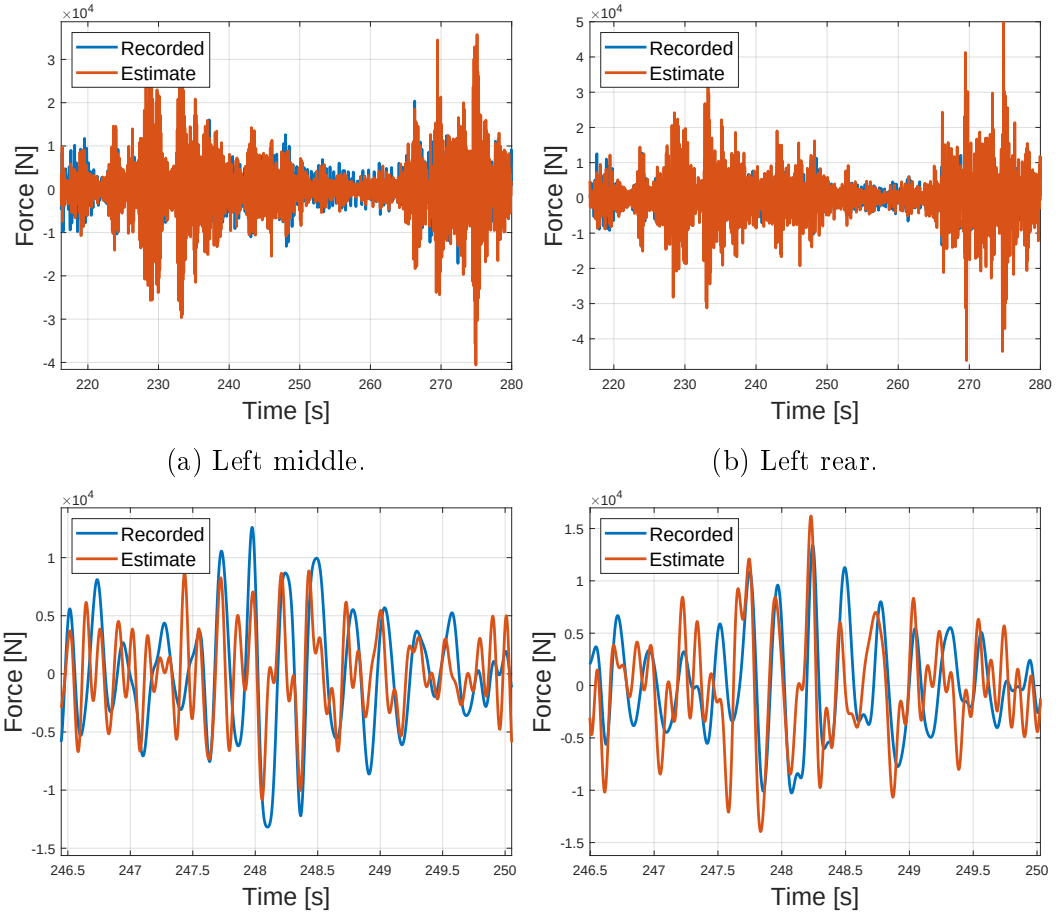

(a) Left middle.

(b) Left rear.

(c) Left middle zoomed.

(d) Left rear zoomed.

Figure 5.7: Correlation between recorded and estimated wheel forces for the left middle and left rear wheels.

The sum of forces experienced by the truck chassis at the rear suspension attachment points could be calculated with either:

$$\sum F_{chassis\ rear} = m_{rqb}\ddot{z}_{rqb}, \tag{5.11}$$

or

$$\begin{aligned}\sum F_{chassis\ rear} = &- k_{sm}(z_{rqb} - z_{sm}) - c_{sm}(\dot{z}_{rqb} - \\ &\dot{z}_{sm}) - k_{sr}(z_{rqb} - z_{sr}) - c_{sr}(\dot{z}_{rqb} - \dot{z}_{sr}).\end{aligned} \tag{5.12}$$

5.3.3 Calculated force accuracy validation

The accuracy of calculated forces using identified parameters from Subsections 5.3.1 and 5.3.2 was validated. This was carried out by calculating the wheel forces using a dataset not previously used in the identification process. This dataset was from Segment B described in Table 3.1 recorded from 00:07:48-00:07:56. The LF, RF, LM and LR wheel forces were calculated using Equation 5.7 with the resulting correlation plots shown in Figure 5.8.

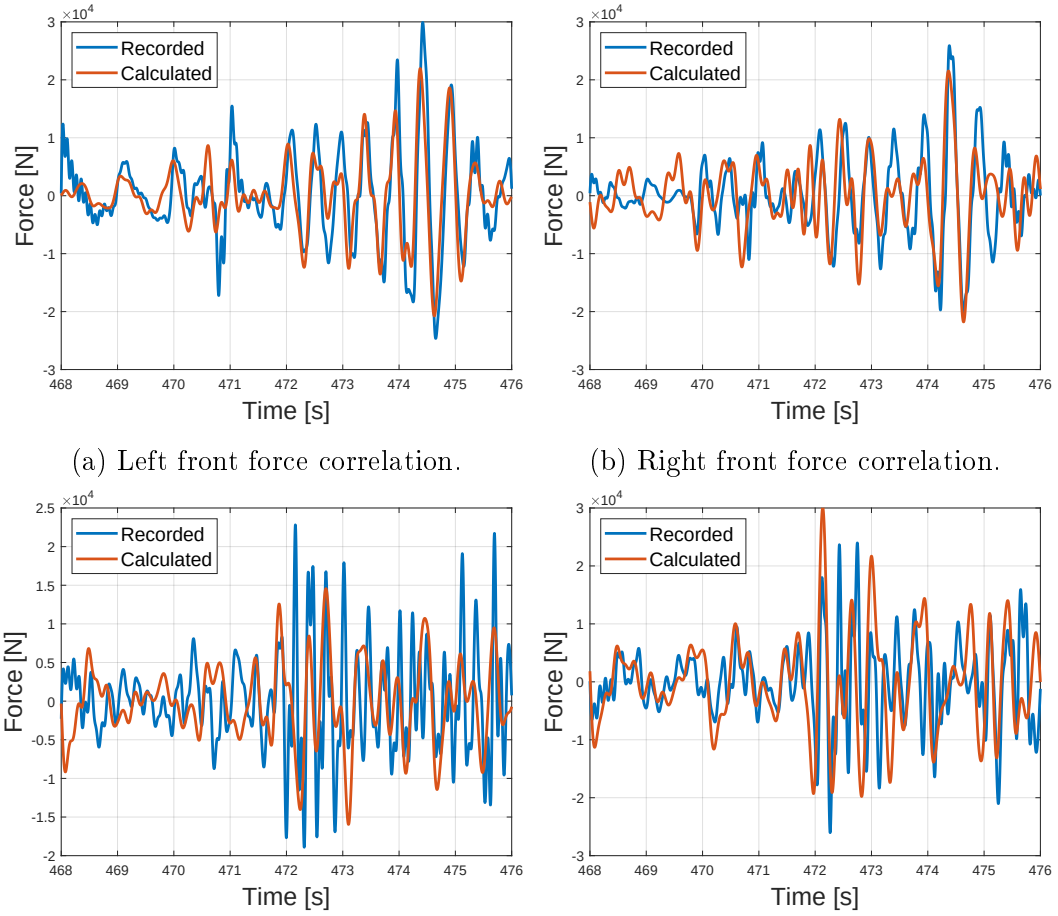

(a) Left front force correlation.

(b) Right front force correlation.

(c) Left middle force correlation.

(d) Left rear force correlation.

Figure 5.8: Correlation between recorded and calculated wheel forces using an alternative dataset and identified parameters to validate results.

The wheel forces were calculated accurately using the independent dataset. This concluded that even though the identified parameters were not necessarily the true system parameters, they related suspension components with high accuracy, i.e. a transfer function was determined. This transfer function accurately related the accelerations of wheel and chassis components to the input

forcing that originated from the wheels. The calculated middle and rear wheel forces correlated well in terms of peak to peak loading but did not match as well as for the front wheels. Inaccuracies were attributed to the simplifications present for the quarter truck models, such as modelling of suspension as independent, that did not take the axle motion into account.

The peak to peak loading of input forces from the road are of main importance to designers so that they know how to plan for loads. It was deemed unnecessary to add complexity to the quarter truck models if the peak information could be determined using the current models.

5.4 System parameter identification using only acceleration data

Further analysis was conducted to determine the contribution of wheel force transducer data. The system parameter identification process was repeated using only the acceleration data measured at wheels and at the suspension attachment points on the truck chassis.

5.4.1 Front quarter truck model parameter identification

The parameter identification process conducted in Section 5.3.1 was repeated with some alterations as the force data was not considered. Without the availability of force data Equation 5.2 could no longer be used. This reduced the objective function that is optimised for parameter identification to:

$$SSE = \sum_{i=1}^{n} \frac{\left(\ddot{z}_{qb}(i) - \hat{\ddot{z}}_{qb}(i)\right)^2}{\max\left(|\ddot{z}_{qb} - \hat{\ddot{z}}_{qb}|\right)}. \tag{5.13}$$

Matlab's particle swarm optimiser optimised Equation 5.13 and identified system parameters m_{qb}, k_s and c_s as introduced in Figure 5.1. The results of parameter identification conducted for 10 independent optimisation runs for the left and right quarter truck models are shown in Tables 5.3 and 5.4. The PSO converged to the same minimum objective function value for all 10 independent optimisation runs.

Similar results were witnessed to those in Section 4.3 where the experimental setup's parameters were identified using only acceleration data. The relationship between m_{qb}, c_s and k_s was determined, but not the exact values. If one of the parameters were known, the other two could be determined from their relationships with the known parameter. Using the results from Tables 5.3

and 5.4 directly to recover input loading on the truck chassis would lead to inaccurate load predictions.

Table 5.3: Identified parameters for the front left quarter truck model using only acceleration data.

Optimisation	m_{qb} [kg]	c_s $\left[\frac{\text{kN·s}}{\text{m}}\right]$	k_s $\left[\frac{\text{kN}}{\text{m}}\right]$	$\frac{c_s}{m_{qb}}$ $\left[\frac{\text{N·s}}{\text{m·kg}}\right]$	$\frac{k_s}{m_{qb}}$ $\left[\frac{\text{N}}{\text{m·kg}}\right]$
1	7220.9	0	1106.7	0	153.267
2	6862.5	13.692	1033.7	1.995	150.624
3	9785.6	19.522	1474.1	1.995	150.643
4	9483.1	18.919	1428.6	1.995	150.642
5	9882.0	0	1514.6	0	153.265
6	9826.9	19.597	1480.5	1.994	150.659
7	8888.8	0	1362.4	0	153.270
8	8992.6	17.941	1354.7	1.995	150.645
9	9539.4	19.031	1437.0	1.995	150.643
10	9700.1	19.334	1460.7	1.993	150.590

Table 5.4: Identified parameters for the front right quarter truck model using only acceleration data.

Optimisation	m_{qb} [kg]	c_s $\left[\frac{\text{kN·s}}{\text{m}}\right]$	k_s $\left[\frac{\text{kN}}{\text{m}}\right]$	$\frac{c_s}{m_{qb}}$ $\left[\frac{\text{N·s}}{\text{m·kg}}\right]$	$\frac{k_s}{m_{qb}}$ $\left[\frac{\text{N}}{\text{m·kg}}\right]$
1	9.7969	19.168	1554.6	1.957	158.683
2	8.5615	16.759	1358.6	1.958	158.689
3	6.6908	13.097	1061.8	1.958	158.688
4	6.7040	13.130	1063.8	1.959	158.682
5	9.2744	18.153	1471.7	1.957	158.689
6	6.4019	12.531	1015.9	1.957	158.686
7	9.9999	19.574	1586.9	1.958	158.688
8	9.9143	19.404	1573.3	1.957	158.690
9	8.4275	16.493	1337.3	1.957	158.684
10	8.5759	16.786	1360.9	1.958	158.688

This method does provide useful information. In most design applications, knowledge about the suspension would be known, or the stiffness could be easily determined through simple measurements such as measuring the displacement of a wheel under a known load. These measurements were not possible as the truck was not available for further testing and measurements. Once the parameters are known, the input loading on the truck chassis can be determined using Equations 5.8 and 5.9. Unfortunately, it is not possible to

determine the input loading the truck wheels experience with this method, as the motion of m_f can not be modelled. However, it is possible to determine the loading experienced by the truck chassis.

Using the previously identified values of k_s for the left and right front quarter truck models in Table 5.1, and the determined parameter relationships in Tables 5.3 and 5.4, the sum of forces experienced by the truck chassis was determined with Equations 5.8 and 5.9 and plot in Figure 5.9. Note that if m_{qb} were known with some accuracy, the curve corresponding to Equation 5.8 in Figure 5.9 could be produced. This required only a single accelerometer instrumented on the truck chassis at the suspension attachment location.

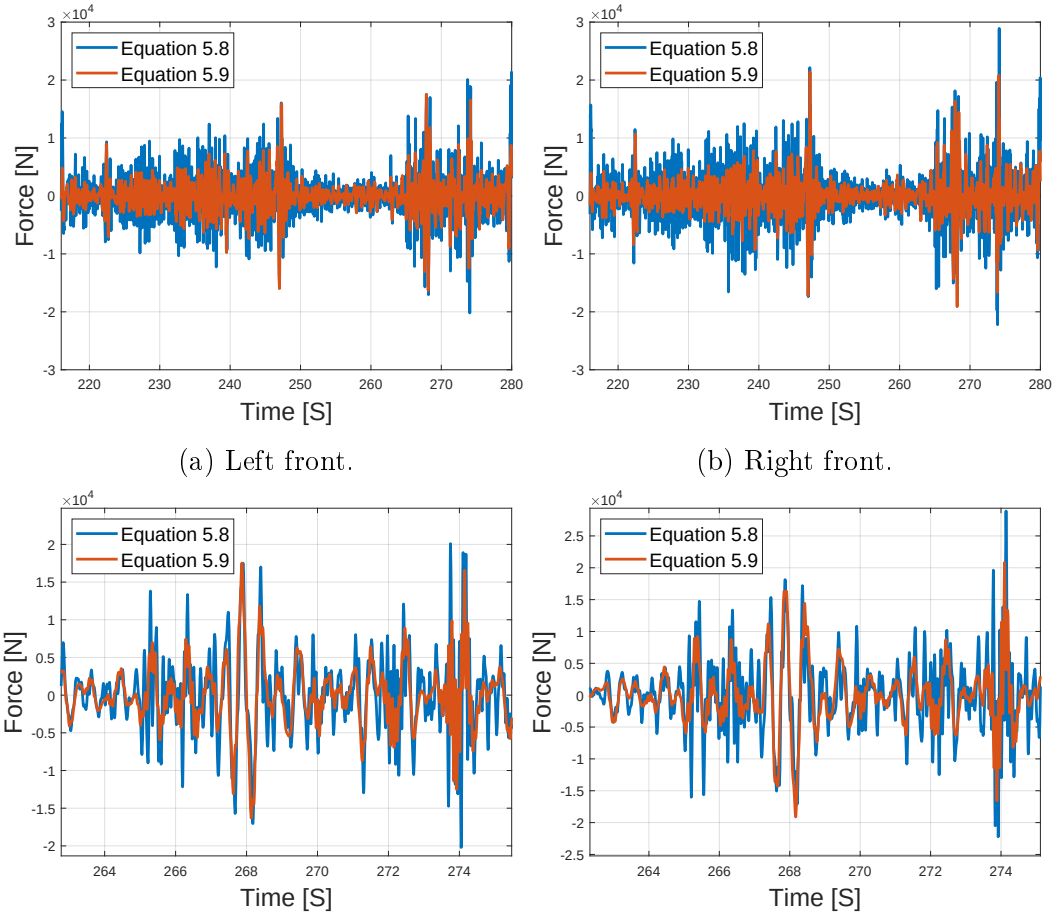

(a) Left front.

(b) Right front.

(c) Left front zoomed.

(d) Right front zoomed.

Figure 5.9: Sum of forces experienced by the truck chassis at the front left and right suspension attachment points.

The front suspension system is a leaf spring suspension system as described in Section 3.4. Thus, the sum of forces shown in Figure 5.9 does not act through

a single attachment point on the truck chassis. Rather, it is distributed to the chassis through the pivot and shackle attachment points. This distribution of forces can be calculated using strength of material approaches where the leaf spring is considered as a simply supported beam with a hinge on the one side and a roller connection on at the other side with the force acting through the beam centre. Using statics, the force inputs experienced at the chassis attachment points could be calculated.

5.4.2 Rear quarter truck model parameter identification

Parameter identification of the rear quarter truck model was conducted without the availability of wheel force data. The objective function that was optimised reduced to:

$$SSE = \sum_{i=1}^{n} \frac{\left(\ddot{z}_{rqb}(i) - \hat{\ddot{z}}_{rqb}(i)\right)^2}{\max\left(|\ddot{z}_{rqb} - \hat{\ddot{z}}_{rqb}|\right)}. \tag{5.14}$$

As expected, the particle swarm optimiser converged to the same objective function value for each run, but with different identified parameters. These parameters consistently had the same relationship with one another as shown in Table 5.5 for 10 independent optimisation runs.

Table 5.5: Relationship between identified system parameters for the rear quarter truck model using only acceleration data.

Run	$\boldsymbol{m_{rqb}}$ [kg]	$\frac{\boldsymbol{c_{sm}}}{\boldsymbol{m_{rqb}}}$ $\left[\frac{\text{N·s}}{\text{m·kg}}\right]$	$\frac{\boldsymbol{c_{sr}}}{\boldsymbol{m_{rqb}}}$ $\left[\frac{\text{N·s}}{\text{m·kg}}\right]$	$\frac{\boldsymbol{k_{sm}}}{\boldsymbol{m_{rqb}}}$ $\left[\frac{\text{N}}{\text{m·kg}}\right]$	$\frac{\boldsymbol{k_{sr}}}{\boldsymbol{m_{rqb}}}$ $\left[\frac{\text{N}}{\text{m·kg}}\right]$
1	10000.0	1.2113	0	191.3856	352.8145
2	9994.1	1.2114	0	191.3780	352.7996
3	8112.9	1.2113	0	191.3852	352.8137
4	9993.4	1.2110	0	191.3796	352.8148
5	9997.8	1.2113	0	191.4050	352.8237
6	10000.0	1.2113	0	191.3856	352.8139
7	9989.8	1.2116	0	191.3800	352.8040
8	10000.0	1.2113	0	191.3860	352.8159
9	8356.7	1.2113	0	191.3708	352.7972
10	9018.1	1.2113	0	191.3845	352.8130

In Table 5.5 m_{rqb} is determined as 10000 kg multiple times. This was simply the PSO converging to the upper boundary condition set for the range wherein it could optimise for m_{rqb}. Altering the boundary conditions did not produce

a unique convergence. The optimiser simply assigned each parameter a value and determined the other parameters accordingly.

The parameters determined using only acceleration had the same relationship with one another as the parameters determined using both acceleration and force data shown in Table 5.2. For both scenarios c_{sr} was identified as zero. This phenomenon also occurred for the front quarter truck model as seen in Table 5.3 where c_s was identified as zero for three of the 10 runs. Note that the spring constant k_s was assigned a higher value, resulting in a stiffer spring constant to account for the zero damping. The lower bound set for c_{sr} was set as zero as damping could never be negative. If the lower boundary condition increased, k_{sr} was adjusted to accommodate for the damping while the other parameters remained unchanged. And vice versa, if k_{sr} was fixed, c_{sr} would adapt accordingly. If k_{sr} was known, all other parameters could be determined.

The sum of forces experienced by the truck chassis at the rear suspension attachment points could be determined by repeating the process outlined in Section 5.4.1 using Equations 5.11 and 5.12. Correlation plots were not included here as the same response was seen in Figure 5.9. Note that the sum of forces does not act through a single attachment point on the truck chassis. Rather, it is distributed to chassis components with the torque rods and other suspension components.

5.5 Summary

In this chapter the input loading experienced by a truck was recovered through multi-body dynamic simulation. Quarter truck models were developed that simulated how loads are transmitted through the wheels and to the chassis. Model parameters were unknown and had to be identified using data captured with various instrumentation and optimisation methods. These parameters were used in equations of motion to develop transfer functions that related input loading with sprung and unsprung mass motion. Of interest was the accuracy with which input loading could be recovered rather than the parameters themselves. The input loading was accurately calculated, as shown in Figure 5.8.

With the wheel force data available, a dynamic model was still required to determine how the wheel forces were transmitted to the chassis. An alternative approach that utilised only acceleration data provided a method to determine the relationship between system parameters. If one of these system parameters were known, all the other parameters could be determined. This provided a way to develop a transfer function to estimate the input loading on the truck chassis using wheel and chassis acceleration data, with no need for wheel force transducers.

Furthermore, if an accurate approximation of the body mass distributed at the suspension point were known, the sum of forces experienced by the chassis could be determined using only a single accelerometer. This accelerometer must be instrumented at the suspension attachment location. Note that with only a single accelerometer instrumented, the relative displacements and velocities between wheels and the chassis cannot be determined. This makes it impossible to decompose the sum of forces into its comprising components.

The system was not solved as a differential equation as had been done previously in Section 4.4. This process allows the recovery of wheel forces using only wheel accelerations, but it requires a more complex model and that all the parameters pertaining to that model be known. As seen in Section 4.4, if the model is simplified (damping not included), the recovered input loading loses accuracy. The quarter truck models used in this chapter would have to be expanded (half or full truck models) to apply this approach. Furthermore, these model parameters could not be determined using only wheel accelerations. For these reasons this approach was not applied.

Chapter 6

Load recovery from strain gauge data

6.1 Background

Previous studies by Dhingra *et al.* (2013) and Hunter (2018) achieved load recovery in structural components using dynamic and static strain gauge measurements. These studies developed approaches that allow a structure become its own load transducer, and are outlined in Section 2.4. Simple cantilever beam structures were analysed in these papers, one example of which is provided in Figure 6.1.

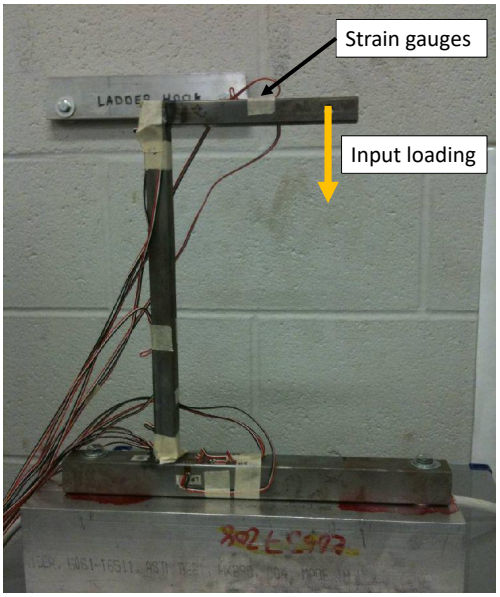

Figure 6.1: Experimental cantilever beam setup used by Hunter (2018).

The relevance of this approach for load recovery on a truck was investigated

in this chapter. The loads of interest which need to be recovered for the truck originate from the wheels which are the boundary conditions. This is where the load recovery investigated in this chapter differs from previous work by Hunter (2018). The recovered input loading on the cantilever beam did not originate at the boundary conditions, as shown in Figure 6.1. This allowed Hunter (2018) to apply unit loading numerically at input loading locations using an FE model of the setup to generate $\boldsymbol{A}$ and ultimately load recovery was achieved. A different approach was developed and tested for the application of unit loads on the truck to generate $\boldsymbol{A}$.

Dhingra *et al.* (2013) and Hunter (2018)'s experiments had isolated input loading conditions and all input loading could be accounted for. Reaction forces from wheels are not solely vertical and contain moments and reaction forces in directions that are not of interest. These were not of interest since they were far smaller than the vertical reaction forces. Chassis design focusses on the largest forces experienced, to ensure that the chassis can handle these inputs. Although these other reactions were not of interest, they did generate strain responses in the system that was in turn captured in strain gauge measurements. The influence of these reactions on the accuracy of load recovery was also investigated.

6.2 Load recovery with shell model

Load recovery started with checking the process with simpler applications and then progressing to more complex models. The theory was tested by recovering reaction forces in the Z-direction experienced by the FE model for the same loading conditions as for Run 1 mentioned in Section 3.3. Shell elements corresponding to strain gauge locations as instrumented on the actual truck shown in Figure 3.2 were identified. These elements were used as virtual strain gauges in the FE model from which virtual strain measurements could be recorded.

In order to test the load recovery process the vertical reaction forces were recovered for the FE model simulating the truck (no payload or container) resting on a frictionless horizontal flat surface while experiencing gravity. Only six vertical reaction forces would be experienced by the FE model at wheel attachment points due to imposed boundary conditions. Load recovery usually determines the input loading experienced by a structure. In this case and in the cases that follow the resulting reaction forces at the boundary conditions due to the input loading (gravity) will be recovered rather than the input loading itself.

The first step in the load recovery process with strain gauge data is to compile the sensitivity matrix, $\boldsymbol{A}$, required to solve Equation 2.6. Six unit loads (red

arrows) were applied, one at a time, at wheel attachment points on axles as shown in Figure 6.2. During the application of unit loads, the FE model had no boundary conditions with inertia relief active to balance the rigid body modes. Resulting strains at virtual strain gauge positions are purely due to each individual unit load. Using these strains $\boldsymbol{A}$ was compiled. This sensitivity matrix was then used to recover the reaction forces experienced by the FE model due to the gravity load case.

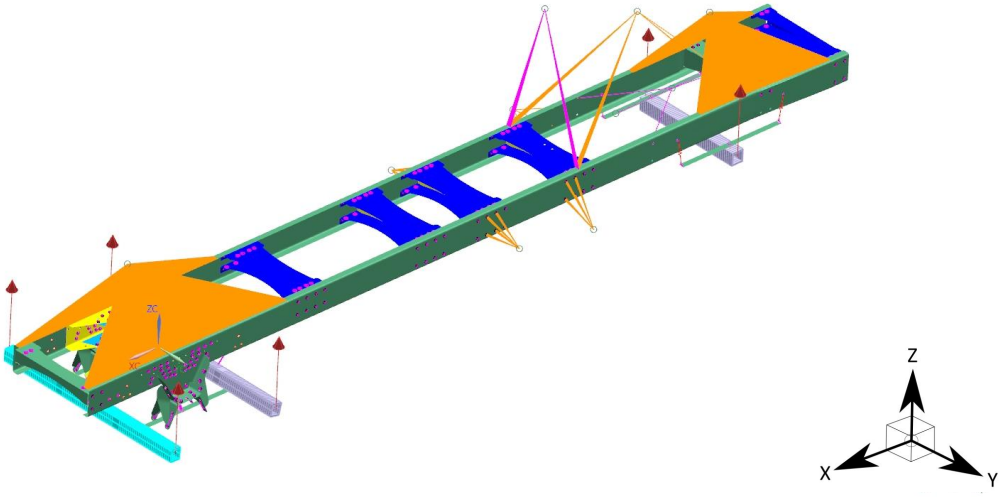

Figure 6.2: Unit loads applied to the FE model to generate a sensitivity matrix.

A script was coded in Python using the pyNastran library to perform the load recovery using the data files generated by NX. NX uses Nastran as a solver. The pyNastran software interfaces to Nastran's complicated input and output files. This provides a simplified interface to write, read and edit the various files (Doyle, 2019).

Strain data recorded by virtual strain gauges was recorded in each element's local coordinate system and output in this format by Nastran. Virtual strain data was rotated to align with the global coordinate system using the theory discussed in Section 2.4.3. Rotation is not necessary for the load recovery testing procedure conducted here, but it will be important when working with field data recorded by the actual strain gauges that were instrumented according to the global coordinate system.

Results of this load recovery test are given in Table 6.1. There was no difference between reaction forces at wheel locations determined by NX and the recovered reaction forces using load recovery theory. This is due to the same FE model being used to generate both $\boldsymbol{A}$ and the virtual strain gauge data for the gravity load case. Virtual strain gauges recorded data perfectly and introduced no

error into the system. This proved that the load recovery theory was being applied correctly.

Table 6.1: Accuracy of load recovery process for an ideal test case.

Location	Reaction force with NX [kN]	Recovered reaction force [kN]	% Error
RR	17.580	17.580	0
RM	19.634	19.634	0
RF	25.280	25.280	0
LF	25.267	25.267	0
LM	19.921	19.921	0
LR	18.654	18.654	0

6.3 Impact of dominating forces

The boundary conditions experienced by the real truck, when stationary, were not the same as the conditions applied to the FE model in Section 6.2. In reality, the truck was resting on a surface that has friction and that is not perfectly flat. Due to these conditions, the truck did not solely experience vertical reaction forces at the wheels. A combination of reaction forces and moments in all directions were transmitted to the axles from the wheels.

Table 6.2 summarises all reaction forces and moments experienced by the truck wheels during the data collection of Run 1. Column names were shortened for display purposes. Here, the letters **F** and **M** refer to a force or moment respectively, followed by the directional components **X**, **Y** and **Z** for the X-, Y- and Z-directions respectively. Vertical reaction forces (**FZ**) were much larger than the other reaction forces and moments.

As a result, the truck would have deformed due to each of the reaction forces and moments which introduced strains. As seen in Table 6.2, not all reaction forces and moments have the same magnitude and their contribution to the total strain experienced by the truck is not equal. Greater emphasis was placed on accurately recovering the vertical reaction forces rather than the other reactions. This is due to their being much larger than the other reaction forces and moments. This information is important for design purposes. Wannenburg (2007) concluded in his study of the fatigue loading on automotive structures, that the vertical loads represent by far the largest proportion of fatigue damaging loads on a vehicle structure. The study concluded that accurate analyses can be conducted while only applying the vertical loading to the FE models. This section investigates the possibility of the accurate

recovery of vertical reaction forces, while not taking into account the resulting strain from other reaction forces and moments.

Table 6.2: Reaction forces and moments measured by wheel force transducers for the unloaded truck in Run 1.

Location	FX [kN]	FY [kN]	FZ [kN]	MX [kN/m]	MY [kN/m]	MZ [kN/m]
RR	1.015	3.508	18.220	-1.396	-0.176	0.060
RM	-3.554	6.559	18.700	-0.825	-0.985	-0.400
RF	1.045	0.767	26.220	-2.120	0.042	0.224
LF	0.365	-2.919	24.530	2.259	-0.126	0.082
LM	-1.172	-5.403	19.660	0.542	-0.028	-0.347
LR	0.116	-2.995	18.860	1.575	-0.121	-0.241

Another load recovery was conducted using a numerical experiment that produced virtual strain gauge data. The sensitivity matrix for this experiment was generated in exactly the same manner as done in Section 6.2 using six vertical unit loads applied one at a time. Next, a load case was set up for which the vertical reaction forces need to be recovered. In this load case, all the reaction forces and moments measured by the wheel force transducers, as provided in Table 6.2, were applied at wheel attachment points in the FE model as depicted in Figure 6.3.

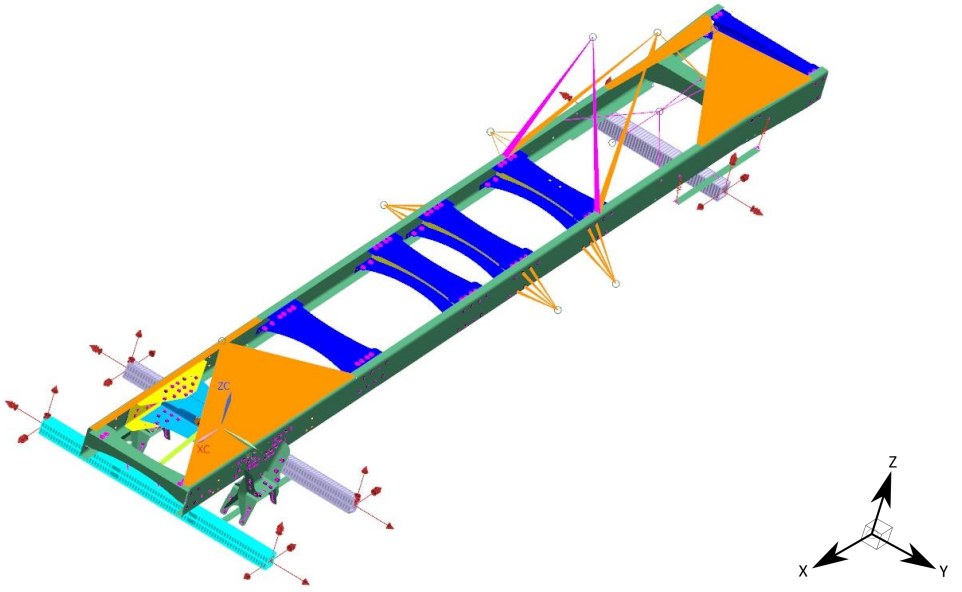

Figure 6.3: Application of all reaction forces and moments to the FE model.

Inertia relief made it possible to apply al the reaction forces provided in Table 6.2 to the FE model without the need for boundary conditions. Only the vertical forces are to be recovered and thus the smallest size of sensitivity matrix that can be used is six by six. This requires the use of a minimum of six strain gauges to set up six equations to solve for the six unknowns (vertical reaction forces). By using more gauges than recovered loads, the sensitivity matrix expands and the system becomes overdetermined, meaning that there are more equations than unknowns. This reduces the variability in recovered loads. More detail about this characteristic of load recovery with strain gauge data is provided in a following section. This characteristic was employed when the current load recovery was conducted. Load recovery was repeated using various different sizes of the sensitivity matrix. The subset of virtual strain gauges used for these sensitivity matrices was randomly selected.

The results of the recovery accuracy of the vertical reaction forces are shown in Figure 6.4. Higher precision in recovered vertical reaction forces was achieved when an increased number of virtual strain gauges were utilised. Not all strain gauges are equally sensitive to input loadings as discussed earlier in Section 3.3. This is true for the virtual strain gauges as well. Recovered forces with the lowest errors were recovered when using 14 virtual strain gauges. The recovered forces using this sensitivity matrix are provided in Table 6.3 alongside the true **FZ** values as applied to the FE model load case shown in Figure 6.3.

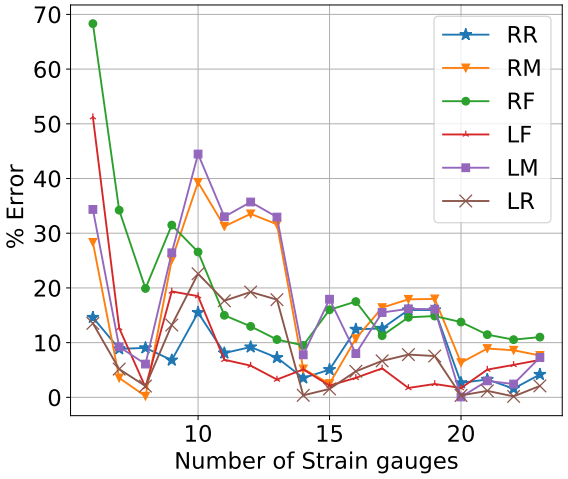

Figure 6.4: Recovery accuracy of vertical reaction forces when using different numbers of virtual strain gauges.

Recovered forces had higher accuracy due to a better conditioned sensitivity matrix that resulted from using strain gauges that are more sensitive to the input loading and more robust to noise. One method to determine which strain

gauges to use when compiling the sensitivity matrix is to perform a D-optimal design. This approach is discussed in a following section.

Table 6.3: Accuracy of recovered vertical forces when using 14 virtual strain gauges.

Location	True value [kN]	Recovered value [kN]	% Error
RR	18.220	17.577	3.5
RM	18.700	19.672	5.2
RF	26.220	23.730	9.5
LF	24.530	25.784	5.1
LM	19.660	18.132	7.8
LR	18.860	18.791	0.4

From the results in Figure 6.4 and Table 6.3, it is clear that strains resulting from vertical reaction forces dominated the strains as a result of the other reaction moments and forces. There was some loss in the accuracy of recovered forces due to the influence of other reactions. If the sensitivity matrix was compiled using the correct strain gauges, then load recovery would be possible with strain gauge data recorded from the actual truck in operation.

6.4 Load recovery using strain gauge field data

In Section 6.3 it was determined that the vertical reaction forces that the truck experienced could be recovered with reasonable accuracy, even though other reaction forces were present when using virtual strain gauge data. The same process was repeated to recover the reaction forces experienced by the actual truck due to the addition of a payload by using strain data recorded during Runs 1, 2 and 3. Analysis of the experimental field data recorded during Runs 1, 2 and 3 in Section 3.3 indicated that only 11 strain gauges were sensitive to the addition of a payload onto the truck. These strain gauges were numbers: 12, 13, 14, 15, 16, 17, 23.2 (0°orientation), 27(0°, 45°orientations), 28 (0°orientation) and 39 (45°orientation) with their locations on the truck as indicated in Figure 6.5.

Six vertical reaction forces at wheel locations needed to be recovered, requiring the use of a minimum of six strain gauges to accomplish load recovery. In Section 6.3 it was determined that the load recovery process is very susceptible to error when using only the minimum required strain gauges. During load recovery all the available strain gauges were utilised.

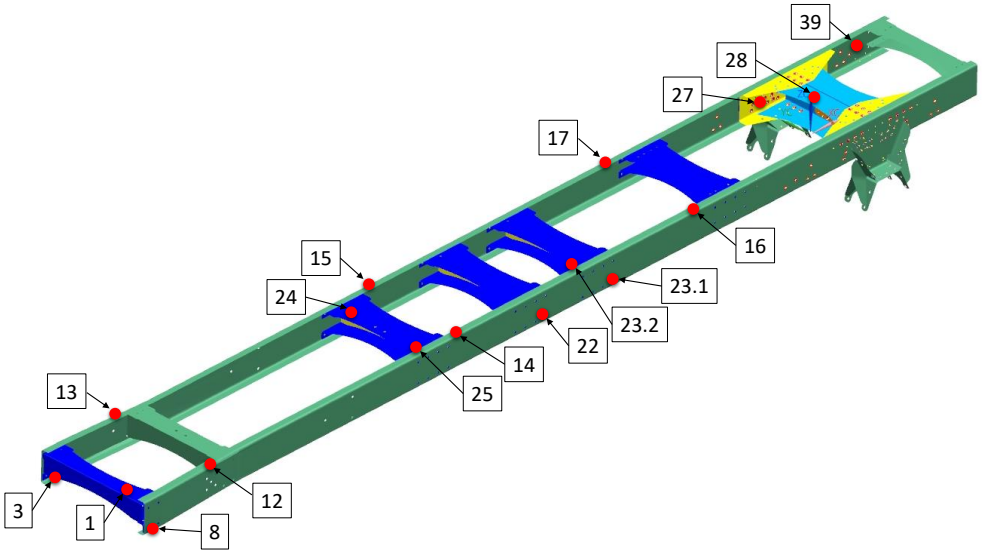

Figure 6.5: Strain gauge positions and labels as instrumented on the truck.

Two load recoveries were carried out using the strain gauge data recorded during Run 2 and Run 3 to determine the wheel forces experienced by the truck under these loading conditions. Once again the sensitivity matrix developed in Section 6.2 was used. The net recorded strain gauge values (e.g. Run 2 - Run 1) were summed to the virtual strain gauge values generated by NX. This simulates the strains experienced at virtual strain gauge positions for a loaded truck experiencing gravity. The results of load recoveries and their accuracies using the two data sets are provided in Table 6.4. The measured wheel force transducer values are also provided for comparison.

Table 6.4: Recovered vertical reaction forces experienced by the wheels during Run 2 and 3.

Load	**Measured Run 2 [kN]**	**Recovered [kN] (% Error)**	**Measured Run 3 [kN]**	**Recovered [kN] (% Error)**
RR	22.500	-44.262 (296.7)	28.834	-14.868 (151.6)
RM	22.514	-35.036 (255.6)	28.460	17.446 (38.7)
RF	31.284	32.836 (5.0)	30.531	25.993 (14.9)
LF	29.286	18.342 (37.4)	32.053	19.469 (39.3)
LM	26.785	-28.893 (207.9)	32.242	35.766 (10.9)
LR	26.061	-52.871 (302.9)	28.405	-31.729 (211.7)

Vertical reaction forces were recovered with higher accuracy using data from Run 3 than from Run 2. The vertical reaction forces at the right front (RF) and

the left middle (LM) wheels were recovered with some accuracy using Run 3's data. All other vertical reaction forces were not recovered accurately. Reasons for inaccuracies are that there were very few sensitive strain gauges available to use in the load recovery process, leading to a load recovery that was very sensitive to errors and noise in the data. Some of these strain gauges recorded strain measurements that were just above 15 με. This value is very small when working with strain gauge measurements. Furthermore, the simplifications to the FE model due to a lack of detail concerning the real truck led to virtual strain gauges that responded differently to input loading when compared to the real strain gauges.

Hunter (2018) concluded that very stable sensitivity matrices have a condition number less than 10. Acceptable sensitivity matrices have condition numbers of 50 or less. The best condition number for $\boldsymbol{A}$ used here, was produced when all 11 strain gauges were used. $\boldsymbol{A}$ that produced the results in Table 6.4 had a condition number of 119.76. This was far outside the range for acceptable sensitivity matrices, proving that the strain gauges were not instrumented ideally for load recovery purposes.

Another load recovery approach was possible with the strain gauge data. Rather than recovering the wheel force reactions at six locations due to a single payload, the size of the single payload could be estimated. In order to estimate the payload size, this approach would require only a single virtual strain gauge to generate the sensitivity matrix (1x1) as well as data recorded by the corresponding strain gauge. For generation of the sensitivity matrix, the payload position must be precisely known, as the corresponding unit load for the payload must be applied in the FE model. This prompted a repeat of the processes from Section 3.2 to determine the payload position through optimisation.

6.5 Payload optimisation

Payload size and position differed for the different datasets. This was due to the container resting on the truck is loaded in different ways for separate deliveries. During Run 1 the truck was unloaded. For Run 2 the payload position was known, as it was an empty container resting on the truck's rear. During Run 3 the container was filled. Mass was not necessarily distributed equally throughout the whole container. The payload position is of importance for the load recovery process when using strain gauge data. This prompted a repeat of the precesses used in Section 3.5 to determine the payload position through optimisation.

By using data from Run 3 Genesis could optimise and determine the payload size and position for this run by minimising the root mean square error differ-

ence between the measured and calculated strains or wheel forces. Data from either the strain gauges or the wheel force transducers could be used. The accuracy of payload estimates using one or the other data set was compared. RBE3 elements were selected to connect the payload to the truck's frame as in Figure 6.6. This would transmit the force resulting from the payload to the frame while not adding stiffness to the structure. The other mass components and their connections were hidden in Figure 6.6 for display purposes.

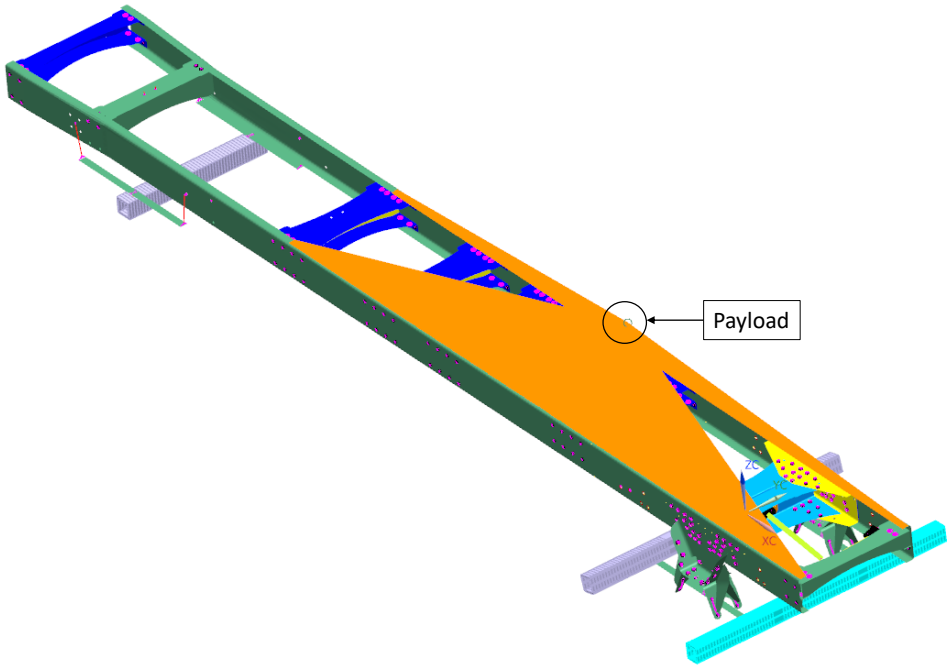

Figure 6.6: Payload position optimised with wheel force transducer data.

The payload optimisation started with the use of strain gauge data. Note that the strain gauges were instrumented on an unloaded empty truck that experiences gravity. Thus, strain gauges are only capable of measuring changes to the system such as the addition of a payload etc. In Section 3.3 it was mentioned that the net strain result due to the addition of the payload onto the truck was determined by subtracting the strains recorded during Run 1 from strains recorded during Run 2 and Run 3.

NX calculates strains seen by virtual strain gauges due to gravity. The FE model simulating the unloaded truck experiencing gravity while resting on a flat frictionless surface from Section 6.2 was utilised again. With the addition of a payload on the truck the strains at the virtual strain gauge positions must increase with the same net field data strain values recorded while the truck was in operation. By altering the payload size and position Genesis could

introduce additional strains at the virtual strain gauge positions to match these objectives. Strain gauges used in optimisation processes were numbers 14 through 17 as their positions were well known and they were sensitive to the addition of a payload as shown in Figure 3.6.

By subtracting the summed wheel force transducer's vertical force data of Run 1 from Run 3 it was determined that the true payload size was 54.414 kN or 5546.79 kg. This was the ideal size of the payload that Genesis should produce. Optimisation started with the payload's size initially set to 6000 kg for the first iteration. A sizing constraint limited Genesis' alteration of the payload size to between 0 and 20000 kg. Alongside the sizing constraints, translational constraints were also in effect determining how far Genesis was allowed to move the payload in the X- and Y-directions. The vertical Z-direction did not have an influence on the resulting strains at strain gauge positions as the load height had minor influence on the way in which it is distributed into the model. Translational constraints allowed translation of the payload 3 m in the positive and negative X-direction and 0.5 m in the Y-direction. These dimensions are the same as the space available between the tarper gantry and the truck's rear where the container was resting. The starting position for optimisation was in the centre of this area.

The optimisation converged and estimated a payload size of 20000 kg that was positioned 1.195 m in the negative X-direction and 0.5 m in the Y-direction. Two of the three boundary conditions were reached. Further simulations were run with more lax boundary conditions for sizing and translation and different starting positions were used for the optimiser. Results did not indicate accurate payload size or position estimates using strain gauge data.

Strains recorded by instrumented strain gauges were very small and sensitive to errors. Most of the strain gauges were not activated and did not register the addition of the payloads during Run 2 and Run 3 as discussed in Section 3.3. This prompted the use of wheel force transducer data of high accuracy (as there is little room for human error in sensor implementation and the locations of these sensors were known precisely).

Optimisation was repeated with the root mean square error between calculated and recorded wheel force reactions set as the objective function. The same sizing and translational constraints were used as in the previous optimisation. Optimisation converged to a payload size of 5407.17 kg displaced 0.3 m in the negative X-direction from the centre between tarper gantry and the truck's rear. Compared to the ideal value of payload size determined earlier this payload size estimate had an error of only 2.5%. Figure 6.6 provides the optimal payload position as determined with the wheel force transducer data. A comparison of vertical reaction forces predicted by the shell FE model for

the static gravity load case of Run 3 can be seen in Table 6.5. Wheel forces were matched with an error margin ranging between 0.9% and 8.5%.

Table 6.5: Comparison of vertical reaction forces at wheels due to payload as determined using WFT and strain gauge data.

Reaction force	Measured value [kN]	Optimized with WFT data [kN]	% Error
RR	28.833	27.326	5.2
RM	28.460	30.877	8.5
RF	30.531	30.805	0.9
LF	32.053	30.757	4.0
LM	32.242	30.966	4.0
LR	28.405	28.648	0.9

6.6 Recovery of payload size with strain gauge data

In Section 6.5 an attempt was made to determine the payload size and position using optimisation with Genesis and strain gauge data. This was unsuccessful and wheel force transducer data had to be used. In this section, the load recovery approach was used to recover only the payload size using strain gauge data. Here the position of the payload was assumed to be known and as determined in Section 6.5. With the position known it was possible to apply a unit load at the payload's position in the FE model. Sensitivity matrices were developed using each individual strain gauge. These sensitivity matrices would relate the strain response of each strain gauge to the payload unit load. From there it was possible to use the strain data recorded by each gauge to recover the payload's size.

Load recovery was conducted using both the Run 2 and Run 3 datasets. To determine the precise size of the payload resting on the truck for Run 2 and Run 3, the vertical reactions recorded by the wheel force transducers were used. By subtracting Run 1's wheel force reactions from Run 2 and Run 3, it was determined that the payload sizes for these load cases were 32.255 kN and 54.414 kN respectively.

All strain gauges were used, one at a time, to recover the payload's size. In an ideal scenario all strain gauges would recover a payload of the same size. This approach made it possible to compare all the strain gauges and to identify which of these were more sensitive to the input loading caused by the addition

of a payload onto the truck. A load case setup shown in Figure 6.7 generated sensitivity matrices for each strain gauge. Boundary conditions were applied to simulate the truck resting on a frictionless flat surface. A single vertical unit load was applied at the payload position.

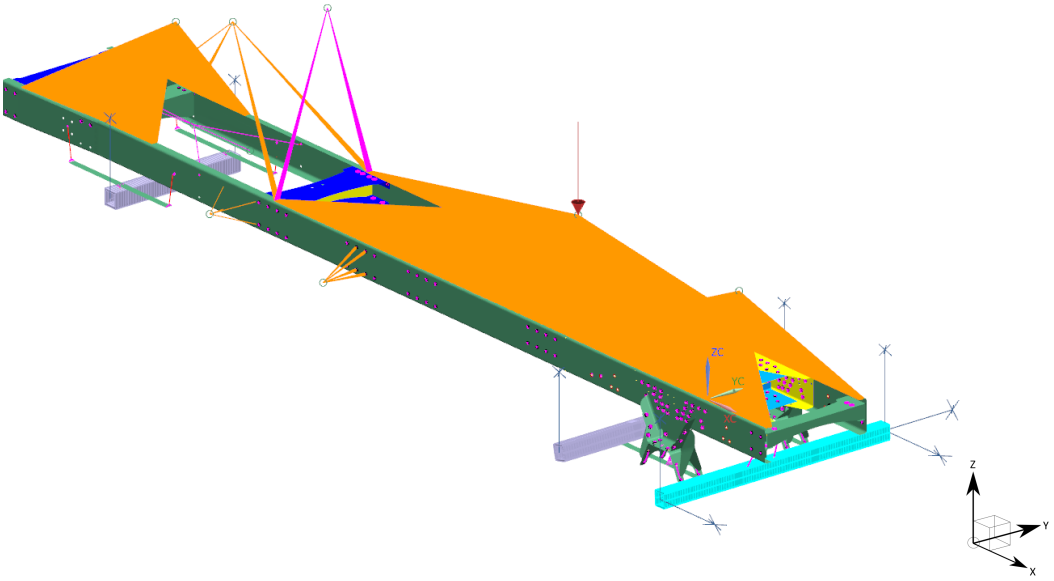

Figure 6.7: Load case setup used to determine the sensitivity matrices used for load recovery of the payload size with field data.

Tables 6.6 and 6.7 provide the summarised results of payload sizes recovered using data from Run 2 and Run 3 respectively. These tables provide the results of the sensitive strain gauges used for load recovery in Section 6.4. The payload size was recovered using all 39 strain gauges. These results are provided in Tables C.1 and C.2 in Appendix C.

Table 6.6: Recovered payload size using one strain gauge at a time for the Run 2 dataset.

Strain gauge (angle)	**Measured payload size [kN]**	**Recovered payload size [kN]**	**% Error**
12	32.255	281.064	771.4
13	32.255	-380.649	1280.1
14	32.255	34.154	5.9
15	32.255	66.457	106.0
16	32.255	27.959	13.3

Continued on next page

Table 6.6 – *Continued from previous page*

Strain gauge (angle)	**Measured payload size [kN]**	**Recovered payload size [kN]**	**% Error**
17	32.255	31.933	1.0
23.2 (0°)	32.255	-1269.50	4035.8
27 (0°)	32.255	585.261	1714.5
27 (45°)	32.255	-10621.457	33030.0
28 (0°)	32.255	-539.689	1773.2
39 (45°)	32.255	-4208.342	13147.1

Table 6.7: Recovered payload size using one strain gauge at a time for the Run 3 dataset.

Strain gauge (angle)	**Measured payload size [kN]**	**Recovered payload size [kN]**	**% Error**
12	54.414	-940.252	1828.0
13	54.414	-2599.416	4877.1
14	54.414	58.798	8.1
15	54.414	35.757	34.3
16	54.414	119.325	119.3
17	54.414	56.215	3.3
23.2 (0°)	54.414	-4933.365	9166.4
27 (0°)	54.414	1188.509	2084.2
27 (45°)	54.414	-21485.631	39585.5
28 (0°)	54.414	-1324.552	2534.2
39 (45°)	54.414	-1599.22	3039.0

Very few strain gauges recovered a payload size that correlated with what was expected. Accurate payload size recoveries for Run 2 were achieved when strain gauges 14, 16, 17 and 22 (45°) were used. Accurate payload size recoveries for Run 3 were achieved when strain gauges 14, 15, 17, 23.1 (90°) were used. Strain gauges 14 and 17 consistently recovered the payload accurately with less than 9% error. Instrumentation locations for strain gauges 14, 15, 16 and 17 were well known and the geometry of the FE model was well defined at these locations, i.e. far from point loads or cross member attachment points that could cause stress concentrations. These strain gauges also proved to be the most sensitive to the addition of the payloads when their strain measurements before and after the payload addition were compared to the other gauges. All of these factors contributed to it being possible to recover the payload size using these specific strain gauges.

6.7 Load recovery using a beam model as experiment

Load recovery using strain gauge data recorded during Runs 1, 2 and 3 was not feasible as shown in Sections 6.4 and 6.6. Various reasons contributed to the inapplicability of strain gauge data being:

1. Simplifications to the FE model due to lack of available detail.
2. Lack of detail regarding locations where strain gauges were instrumented.
3. Possible bad locations for load recovery that led to ill-conditioned sensitivity matrices.
4. Too few strain gauges were sensitive to input loading (low readings).

An alternative approach was employed to generate numerical data to further investigate the applicability of load recovery on trucks using strain gauge data. Numerical data was generated using a simplified version of the FE model consisting of beam elements. Using this model as an experiment, numerical experimental data of higher quality was produced and the various other aspects that influence load recovery with strain gauge data were investigated.

The further simplified beam element model is shown in Figure 6.8. All cross-members and frame components that were originally meshed with 2D shell elements, were meshed with 1D beam elements with the appropriate cross-sectional profile for each component. Brackets were not modelled in the beam element FE model and cross-members were connected to the frame using rigid RBE2 element connections. Point masses accounting for the fuel tank, carry box, battery and hydraulic tanks were connected to the frame using single rigid RBE2 connections. The compensating, payload, cab, engine and transmission mass connections were modelled in the same way as in the original shell element FE model.

The advantages of using the beam element model as an experiment include:

1. Beam model had high fidelity when compared to the original shell FE model (see Table 6.8).
2. High precision regarding strain gauge locations and orientations.
3. Application of D-optimal design is possible to determine ideal virtual strain gauge locations.
4. Cleaner virtual strain gauge data can be generated (not subjected to noise).
5. Large number of virtual strain gauges can be used.

6. Precise loading conditions experienced by the truck model were known, that allowed the evaluation of the accuracy with which loads were recovered.

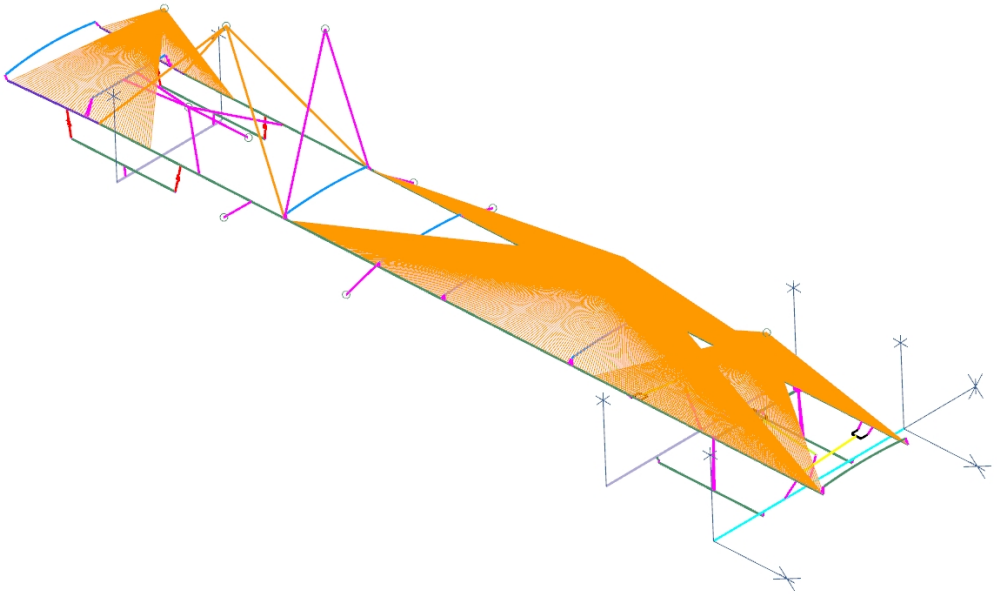

Figure 6.8: Further simplified beam element FE model of the truck.

A load case simulating loading conditions present during Run 3 was set up using the simplified beam element FE model. Table 6.8 provides a comparison between the vertical reaction forces measured by the wheel force transducers and the calculated forces with the original and the simplified FE models. The simplified model closely related to the original shell element model. Deviations in simulated reaction forces were due to the simplified nature of the new model.

Table 6.8: Comparison of the vertical reaction forces as calculated by NX for a load case simulating Run 3.

Load location	**Measured [kN]**	**Original FE model [kN]**	**Simplified FE model [kN]**
RR	28.833	27.326	26.399
RM	28.460	30.877	30.614
RF	30.531	30.805	30.542
LF	32.053	30.757	30.571
LM	32.242	30.966	29.502
LR	28.405	28.648	28.749

Strain gauge locations used for initial virtual experiments were the same as those provided for the real experiments in Figure 6.5. Gauge locations on cross-member brackets were removed from the virtual strain gauge set, as these brackets were not included in the simplified model. Beam elements only measured virtual strains along their length. Thus, locations that were instrumented with strain gauge rosettes only output a single virtual strain measurement. All of these simplifications reduced the number of virtual strain gauges used in the initial experiments to 15.

The original shell FE model from Section 6.2 was used to set up the sensitivity matrix for load recovery. Virtual experimental data was then generated by the beam element model. The simplified model had the same boundary conditions that the shell model had in Section 6.2 to simulate the truck resting on a frictionless flat surface experiencing gravity. In both FE models the payload size was 5407.17 kg.

The results of load recovery of the vertical reactions using the numerical experimental data are shown in Table 6.9. All 15 currently available virtual strain gauges were used for the load recovery as this subset produced the best results. The condition number for this sensitivity matrix ($\boldsymbol{A}_{non-optimal}$) was 111.1. Comparing the results of virtual experiments in Table 6.9 with results using physical strain gauge data in Table 6.4, the load recovery had greater accuracy.

Table 6.9: Comparison of load recovery accuracy of vertical reactions when using data generated from the beam FE model.

Load location	**NX reaction forces for beam model [kN]**	**Recovered reaction forces [kN]**	**% Error**
RR	26.399	41.833	58.5
RM	30.614	36.939	17.1
RF	30.542	24.544	19.6
LF	30.571	25.588	16.3
LM	29.502	46.339	57.1
LR	28.749	35.173	22.3

Inaccuracies of the load recovery were attributed to virtual strain gauges not being at optimal locations and the load recovery process being sensitive to small errors in the virtual experimental data. These errors are due to the simplifications present in the beam element FE model. Virtual strains calculated by NX for this model will deviate from strains predicted by the shell

element FE model. Further investigation was done to determine the impact of these errors and the application D-optimal design has on the accuracy of load recovery with strain gauge data.

6.8 Effect of random error on load recovery accuracy

The load recovery process could be sensitive to the quality of the data provided. The virtual dataset used in the very first load recovery in Section 6.2, with its results shown in Table 6.1, was used for this study. Loads were recovered perfectly using this data as there were no errors present. To test the sensitivity of load recovery to data quality, the dataset was altered by adding random error.

Uniformly distributed random error was added to the virtual strain gauge data generated from a load case simulating Run 3 by the original FE model. Load recovery was then conducted, with the recovered vertical reaction forces stored. This was repeated 100 times, where each time the virtual strain gauge data was altered with new random errors. The standard deviation for each of the recovered vertical reaction forces over the 100 load recoveries was then calculated. A higher standard deviation of the reaction force indicated that $\boldsymbol{A}$ was more sensitive to errors relating strain responses for that reaction force.

This process of checking the load recovery process' sensitivity to error was repeated twice with random errors between different ranges added to the data. Random strain errors were added within a range of 5% and 10% from the real strain values as generated by NX, for both load recovery sensitivity checks. Additionally, the effect of using different sizes of the sensitivity matrix was investigated. Load recovery for each of the 100 datasets with error added to it, was repeated using sensitivity matrices of different sizes. The same set of 15 virtual strain gauges that were used in Section 6.7 was used here. These sensitivity matrices were compiled using random subsets that ranged between 6 to 15 virtual strain gauges.

The results of these load recoveries using data with added errors of different magnitudes are shown in Figure 6.9. Load recovery was very sensitive to errors in the experimental data when using a six virtual strain gauge sensitivity matrix (6x6). Standard deviations in the recovered loads were large, with the right middle vertical reaction force consistently being the most sensitive to erroneous data. As the number of virtual strain gauges used in a sensitivity matrix increased, the recovered reaction forces were more stable and accurate. The use of more strain gauges increased stability up to a point where the standard deviation in recovered forces converged. The same trend was noticed

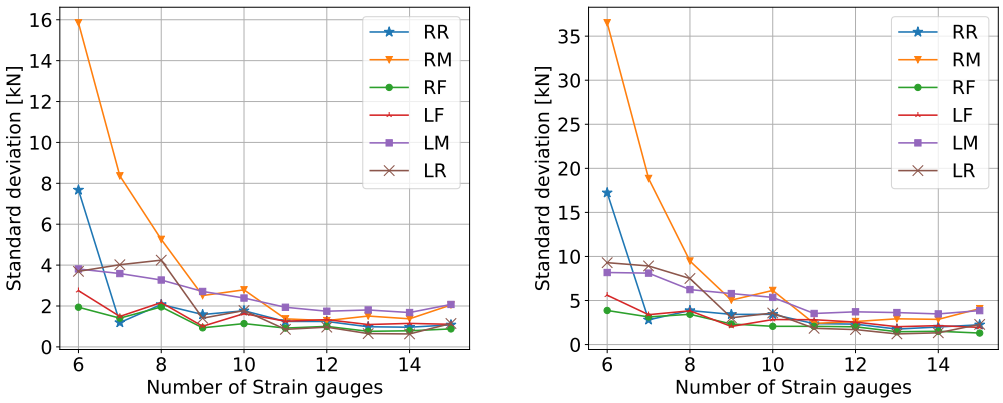

(a) 5 % Random error added to data. (b) 10 % Random error added to data.

Figure 6.9: Correlation between variation in recovered vertical reaction forces with the number of strain gauges used.

for recoveries using data altered by both the 5% and the 10% error ranges. With double the percentage error added, the standard deviation of recovered forces also doubled in magnitude.

To further increase the stability and accuracy of recovered forces, better strain gauge locations were required. These locations could be determined with the use of the D-optimal algorithm.

6.9 Effect of D-optimal design

From Figure 6.9 it is apparent that the number of strain gauges used in the load recovery is a big contributor to the robustness of the process to erroneous data. Another contributing factor is the location of the strain gauge used. Sensitivity of the structure to loads of interest varies throughout the structure. If strain gauges were to be instrumented at better (more sensitive) locations, changes in strain due to loads of interest would be easier to measure and a sensitivity matrix that is more robust to errors could be developed. This is where the D-optimal algorithm can be utilised. The D-optimal algorithm selects the best strain gauge locations from a candidate list of locations provided to the algorithm to ensure that $(\boldsymbol{A}^T\boldsymbol{A})^{-1}$ is well conditioned.

A set of possible element locations was provided to the algorithm. The best subset of these elements was then determined. It is important that care be taken when providing elements to the algorithm. The algorithm will identify the best locations for strain gauge instrumentation regardless of whether or not there are elements already selected at that specific location. For example, if

elements at an ideal location are provided to the algorithm, a group or cluster of elements next to one another could be selected. $(\boldsymbol{A}^T\boldsymbol{A})^{-1}$ would be well conditioned, but duplicate rows could be a result. If, for example, three strain gauges were instrumented right next to one another on the structure, they would measure almost the same strain response due to the input loading. This leads to errors in load recovery. Furthermore, the algorithm only selects unique locations up to a point, after which it selects duplicate locations (same strain gauge position twice) if that would lead to a better conditioned $(\boldsymbol{A}^T\boldsymbol{A})^{-1}$.

To prevent clustering of selected ideal locations, a set of 44 location options on the original FE model were provided to the algorithm. As seen in Sections 3.3 and 6.6, it was noted that the best strain responses to input loading were recorded by strain gauges instrumented on the truck's main frame members. Of the 44 strain gauges, 40 were selected on the truck's main frame and the other 4 were positioned at the centre of cross-members. All possible positions were selected with accessibility in mind as well as the feasibility of instrumenting at these locations on the actual truck to better simulate the real circumstances present when applying load recovery.

The D-optimal algorithm produced five unique sets of strain gauges ranging from six to ten strain gauge locations before duplicate elements were selected. The sensitivity matrices were named $\boldsymbol{A}_{6-10}$, where $\boldsymbol{A}_6$ refers to the sensitivity matrix produced by the D-optimal algorithm for six strain gauges, and so on. The condition numbers of each sensitivity matrix is provided in Table 6.10. $\boldsymbol{A}_6$ had the worst condition number. $\boldsymbol{A}_7$ and $\boldsymbol{A}_8$ had condition numbers inside the acceptable range, whereas $\boldsymbol{A}_9$ and $\boldsymbol{A}_{10}$ were just above the upper limit of the acceptable condition number range. The D-optimal element locations are shown in Figure 6.10. Note that only strain gauge number 17 from Figure 3.2 was placed optimally from a load recovery perspective.

Firstly, the stability of generated sensitivity matrices were investigated. The process used in Section 6.8 was repeated for the same load case using the sensitivity matrices $\boldsymbol{A}_{6-10}$. Load recovery with each optimal sensitivity matrix was repeated 100 times, using virtual strain gauge data that was altered by adding random error to it. The standard deviations in the recovered loads are shown in Figure 6.11. Once again the added error ranged between 5 % and 10 %.

The same trend was noticed when Figures 6.9 and 6.11 were compared. When more strain gauges were used, there was a reduction in sensitivity of the load recovery process to noise. D-optimal designs outperformed non-optimal designs in terms of sensitivity to error during comparison of the load recovery results. All non-optimal designs were outperformed in terms of stability by D-optimal designs except for $\boldsymbol{A}_7$. Standard deviation in recovered loads were

consistently smaller when D-optimal designs were used and faster convergence was achieved, regarding sensitivity to errors, using less strain gauge locations.

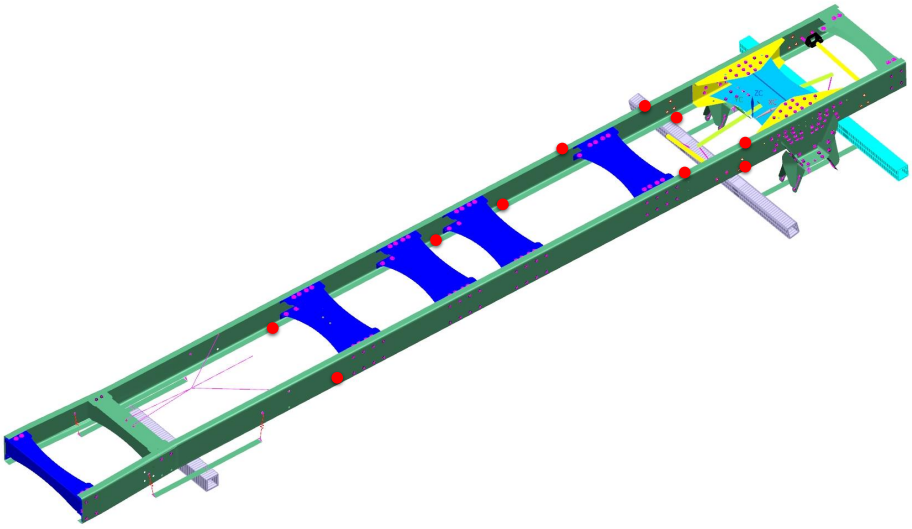

Figure 6.10: D-optimal strain gauge locations on the truck chassis of $\boldsymbol{A}_{10}$.

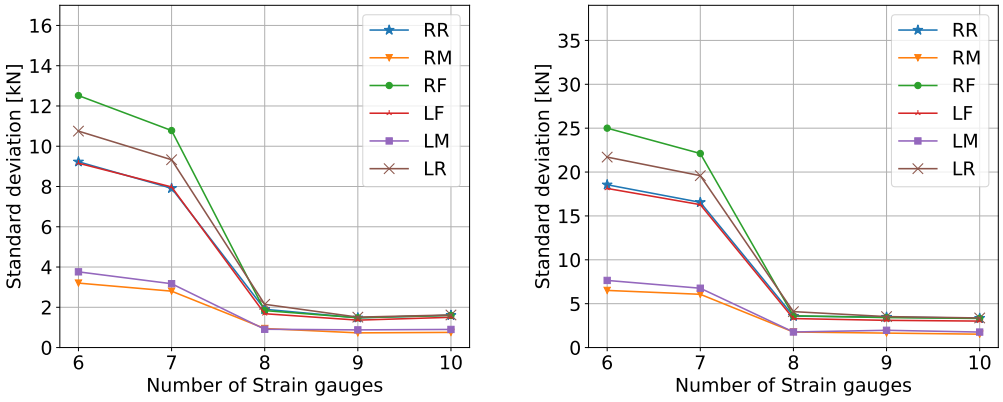

(a) 5% random error added to data. (b) 10% random error added to data.

Figure 6.11: Variation in recovered loads using D-optimal sensitivity matrices with random errors added to data.

Next, the accuracy was investigated concerning the vertical reaction forces which were recovered using D-optimal designs with the beam model as the numerical experiment. The same load recovery was conducted as in Section 6.7 except that in this case sensitivity matrices $\boldsymbol{A}_{6-10}$ were used. The vertical reaction forces recovered at wheel locations are provided in Table 6.10.

Table 6.10: Vertical loads recovered when using D-optimal sensitivity matrices for a gravity load case.

Load location	**Exact [kN]**	$\boldsymbol{A}_{non-optimal}$ **[kN]**	$\boldsymbol{A}_6$ **[kN]**	$\boldsymbol{A}_7$ **[kN]**	$\boldsymbol{A}_8$ **[kN]**	$\boldsymbol{A}_9$ **[kN]**	$\boldsymbol{A}_{10}$ **[kN]**
RR	26.399	41.833	32.436	24.434	25.317	24.504	24.844
RM	30.614	36.939	61.506	26.514	26.782	28.197	28.466
RF	30.542	24.544	24.792	31.263	29.855	30.897	30.936
LF	30.571	25.588	25.323	30.647	29.239	30.307	30.314
LM	29.502	46.339	52.510	25.134	25.415	27.190	27.475
LR	28.749	35.173	40.251	26.043	27.001	26.321	26.620
% Total error	0	190.9	277.8	54.5	43.2	33.4	29.3
Condition number	<50	111.1	192.6	45.4	45.6	54.4	53.8

The % total error refers to the total sum of percentage errors between each of the exact and recovered vertical reaction forces. Results produced by the non-optimal sensitivity matrix ($\boldsymbol{A}_{non-optimal}$) from Section 6.7 was included in Table 6.10. Vertical reaction forces were recovered with the highest accuracy when $\boldsymbol{A}_{10}$ was used. Table 6.11 provides a detailed summary of the results from Figure 6.11b and Table 6.10 when $\boldsymbol{A}_{10}$ was used. Vertical reactions were recovered with high accuracy and had low sensitivity to erroneous data despite $\boldsymbol{A}_{10}$ having a condition number just above 50. The use of more strain gauges counteracted the higher sensitivity of $\boldsymbol{A}_{10}$. Load recoveries with D-optimal sensitivity matrices outperformed non-optimal recoveries in terms of accuracy and robustness to erroneous data.

The application of the D-optimal algorithm is vital when conducting load recovery. The algorithm provides a way to determine where strain gauges need to be instrumented on the structure for effective load recovery. Strain gauges are only instrumented at locations that are sensitive to input loading of interest, thereby preventing the instrumentation of redundant strain gauges, saving time and money. The generated sensitivity matrix is more robust to errors in recorded data leading to higher accuracy of recovered loads.

Table 6.11: Load recovery results using $\boldsymbol{A}_{10}$.

Load Location	**Exact reaction forces [kN]**	**Recovery with beam model data [kN]**	**% Error [kN]**	**Deviation with 10% random error added [kN]**
RR	26.399	24.844	5.9	2.914
RM	30.614	28.466	7.0	1.480
RF	30.542	30.936	1.3	2.700
LF	30.571	30.314	0.8	2.487
LM	29.502	27.475	6.9	1.835
LR	28.749	26.620	7.4	2.898
Sum total	176.377	168.655	29.3	14.314

6.10 Summary

Load recovery using strain data was done. Theory was tested and confidence in the load recovery method was built by using a numerical model under ideal conditions. Loads were recovered perfectly under these circumstances and further investigation was conducted in order to determine how load recovery results were affected when only dominating forces/loads were accounted for.

Next, there was an attempt to recover the vertical reaction forces at wheel locations due to the addition of a payload on the truck's rear with the use of field data recorded during Run 3. This was unsuccessful and the payload size was therefore estimated using load recovery for each individual strain gauge to identify useful strain gauges. This required knowledge of where the payload was located on the truck's rear, which was determined through optimisation. Results using static field data indicated that it would be futile to attempt load recovery of the vertical wheel reaction forces for a truck in motion using dynamic field strain gauge data.

An alternative approach was then used, with a simplified beam FE model which served as a numerical experiment to investigate other influencing factors on load recovery using strain data. The influencing factors were the sensitivity of load recovery to erroneous data and the number of strain gauges used. It was determined that the application of the D-optimal algorithm is essential for load recovery. Recovered loads using D-optimal sensitivity matrices had higher accuracy and the process was more robust to errors present in the datasets.

Load recovery using strain gauges to transform the truck structure into its own load transducer is possible. This process does require an FE model that closely

relates to the actual structure, and precise knowledge of the location and orientation of instrumented strain gauges. Furthermore, a sensitivity matrix that is more robust to erroneous data can be produced with the application of the D-optimal algorithm before strain gauge instrumentation.

Chapter 7

Conclusions and future research

7.1 Conclusions

Alternative approaches for load recovery on a truck chassis using indirect measurements were investigated in this thesis. Two approaches that utilise different types of indirect measurements were investigated extensively. The first approach used multi-body dynamic simulation and acceleration data. The second approach recovered loads using the linear relationship between loads and strains.

An accurate representation of the input loading experienced by the truck chassis was recovered using multi-body dynamic simulation. This process involved the development of two quarter truck models. These models described the motion of the front and rear quarters of the truck. Using only wheel and frame acceleration data, the relative relationships between model parameters were determined. The sum of forces experienced by the chassis at the front and rear suspension attachment points was recovered, assuming that one of the system parameters was known. This method was identified as the best load recovery approach and produced results with the highest accuracy and quality.

In addition, a simplified alternative approach was also developed in order to recover the sum of forces experienced by the truck chassis at suspension attachment points. This approach assumes that a fair estimate of the sprung mass supported at each attachment point is known. Using an accelerometer instrumented at the suspension attachment point and Newton's second law, the sum of forces on the chassis was determined. The sum of forces cannot be decomposed into its components using this method.

An extensive study of load recovery using strain gauge data was then conducted. First, recovery was attempted using strain gauge data recorded while the truck was static. Load recovery for these load cases was inaccurate and

unsuccessful for various reasons. These reasons include: not enough strain gauges were sensitive to the input loading; a $\boldsymbol{A}$ that accurately related the unit loads to the actual loads could not be produced due simplifications to the FE model; and locations where strain gauges were instrumented were not precisely known. For these reasons, recovery of dynamic loads was not possible using strain measurements recorded while the truck was driving.

Numerical models were used to further investigate the feasibility of load recovery on a truck chassis with strain gauge data. Using a numerical approach, experimental field data was produced. With this data available, various other factors that have an influence on load recovery accuracy were investigated. It was concluded that the D-optimal design is essential for accurate load recovery. The D-optimal design also provided a way to determine where to instrument strain gauges on the truck chassis for data collection.

Strain gauge data could be used for load recovery on a truck chassis, but it is not recommended as it has some inherent shortcomings. Besides the previously mentioned pitfalls, a complete detailed FE model has to be setup for each load case scenario. This requires information which is not always available, such as the payload's exact position. Furthermore, the process is very sensitive to noise and errors in the strain gauge data. Great care must be taken to instrument strain gauges precisely as output by the D-optimal design to minimise these errors. This process is very susceptible to human error.

Multi-body dynamic simulation using acceleration data is the best approach for load recovery with the data available at present. This method did not require any alterations to the truck and it does not affect the load path while bypassing the need for expensive wheel force transducers. With this method, the input loadings experienced by a truck chassis in operation could be mapped and used in future FE analysis. FE analysis of higher quality can be conducted, leading to better vehicle designs which are able to handle real world driving conditions better, and are safer for drivers and the general public. Both time and money can be saved by reducing physical prototype testing, due to the higher quality FE analysis that is now possible.

7.2 Recommendations for future work

Further investigation is recommended regarding the effect of greater multi-body dynamic model complexity on load recovery accuracy. The quarter truck model can be expanded into a half and full truck model. The half truck model accounts for the vertical motion of sprung and unsprung masses as well as the pitch motion experienced by the truck body. The full truck model accounts for the axles' roll and vertical motions as well as the truck body's vertical, roll and pitch motions. Due to the availability of more equations of motion,

better parameter identifications could be conducted. This could potentially lead to load recoveries of higher quality. Furthermore, a leaf spring can behave non-linearly. The impact that this characteristic has on load recovery should be investigated in further studies. This can be done by including non-linear stiffness and damping in the quarter truck models.

Based on the findings in Chapter 6, further investigation on load recovery using the linear relationship between strain and input loading should be conducted. It was clear that with currently available datasets, accurate load recovery would not be possible and this method could not be completely validated. Future research into this approach should perform a D-optimal design before the instrumentation of strain gauges. Once successful static load recovery is achieved, the research should be expanded to incorporate dynamic strain responses to recover dynamic input loading.

Appendices

Appendix A

Provided truck dimensions

All truck component measurements that were made available by the external company for development of FE models are shown in Table A.1.

Table A.1: Measurements of made available from which the FE models were developed.

Location A	**Location B**	**Longitudinal Delta [in]**
Bumper	Frame Splay	43.5
Bumper	FAP	55
FAP	BOC	63
BOC	Exhaust Stack	7.5
BOC	Tarper Gantry	10.5
BOC	409 Crossmember	8.5
409 Crossmember	410 Crossmember	42
410 Crossmember	411 Crossmember	29
411 Crossmember	412 Crossmember	57
412 Crossmember	Bogey Crossmember	55
Tarper Gantry	Body SubFrame	10
412 Crossmember	Body Hydraulic Cylinder Pivot	0
FAP	RAP	259
RAP	RA1	23
RAP	RA2	25
Bogey Crossmember	Lateral Torque Rod	32
Tarper Gantry	Battery Box Front Mount	5.5
Bumper	Hood Front Pivot	7.5
Fuel Tank Rear	Body Sub Frame	0

Continued on next page

Table A.1 – *Continued from previous page*

Location A	**Location B**	**Longitudinal Delta [in]**
Front Hanger of Front Suspension	Coolpack	16
Front Hanger of Front Suspension	Engine Crossmember	8
Fuel Tank Rear	Underslung	64
Tarper Gantry	Cab Mount Rear	24.5
Cab Mount Rear	Rear Hanger of Front Suspension	16
Bogey Crossmember	Body Pivot	43
Front Hanger of Front Suspension	A2	13
A2	SG 12/13	5
Tarper Gantry	SG 14/15	9.5
412 Crossmember	SG 16/17	40.5
Top of Frame	Body Hydraulic Cylinder Pivot	Vertical, 23
Longitudinal Torque Rod	Body Hydraulic Cylinder Pivot	Length, 24
Lateral Torque Rod	Body Hydraulic Cylinder Pivot	Length, 19
Hood Front Pivot Left Hand	Hood Front Pivot Right Hand	Lateral, 26.5
Frame Rail Outboard Left Hand	Frame Frail Outboard Right Hand	Lateral, 34
Ground	Lower Frame Flange	Vertical, 30
Outboard Frame	Outboard Battery Box	Lateral, 25
Outboard Frame	Outboard Lower Step	Lateral, 31

Appendix B

Field data post processing

Provided field data sets were unfiltered and contained noise. Noise was removed with bandpass filters. Measured field data signals were converted from the time domain to a representation in the frequency domain with a fast Fourier transform (FFT) in Matlab. This made it possible to analyse the frequency content of the various field data signals. From the frequency content analyses of signals it was clear that a low pass bandpass filter would be required. A complete list of the bandpass frequencies used for each data signal is provided in Table B.1.

Table B.1: Frequency ranges used for the bandpass filters applied to datasets captured with sensors.

Sensor dataset	**Passband frequency range [Hz]**
Accelerometer 1	1-12
Accelerometer 2	1-12
Accelerometer 3	1-10
Accelerometer 4	1-10
LF Wheel acceleration	9-13
RF Wheel acceleration	9-13
LM Wheel acceleration	1-10
RM Wheel acceleration	1-10
LR Wheel acceleration	1-10
LF Wheel force	9-13
RF Wheel force	9-13
LM Wheel force	1-10
RM Wheel force	1-10
LR Wheel force	1-10

Plots of the original and the filtered data sets are provided below. The original signals were detrended to remove the static offset produced by gravity. The plots depict only small segments of the data for visualization purposes. The filtered signals were much smoother than the original signal, whilst still capturing the general trend of the data. The same methods were applied to all the other signals such as the wheel force and wheel acceleration signals, to identify the appropriate bandpass frequencies to use for their respective bandpass filters. Wheel force transducers captured fairly clean data and was not altered much through the filtering process.

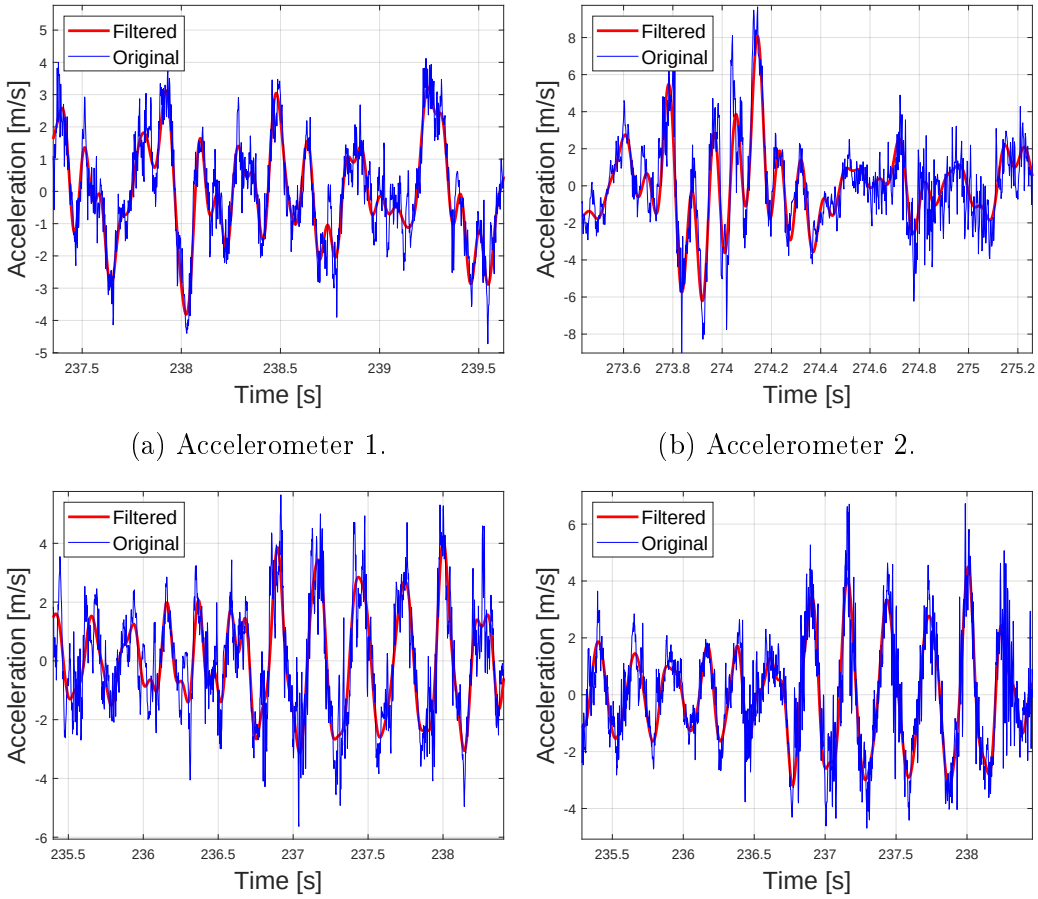

(a) Accelerometer 1.

(b) Accelerometer 2.

(c) Accelerometer 3.

(d) Accelerometer 4.

Figure B.1: Filtered and unfiltered acceleration signals captured by accelerometers on the truck's chassis.

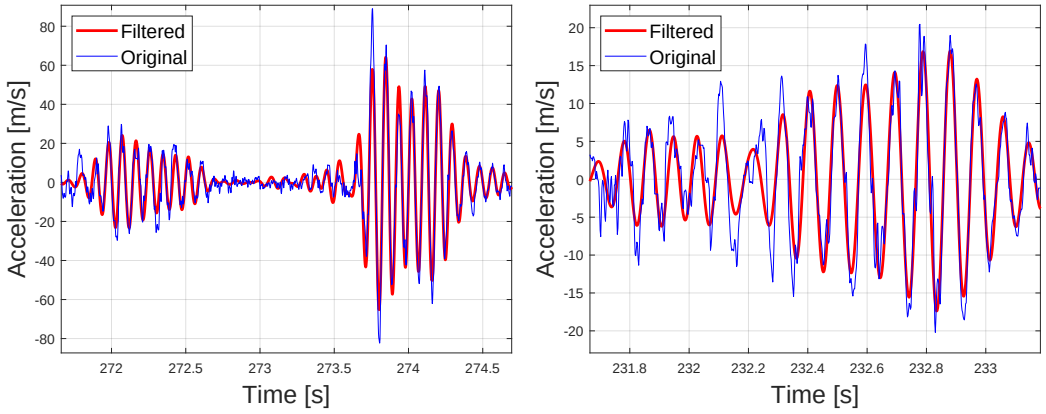

(a) Left front wheel acceleration.

(b) Right front wheel acceleration.

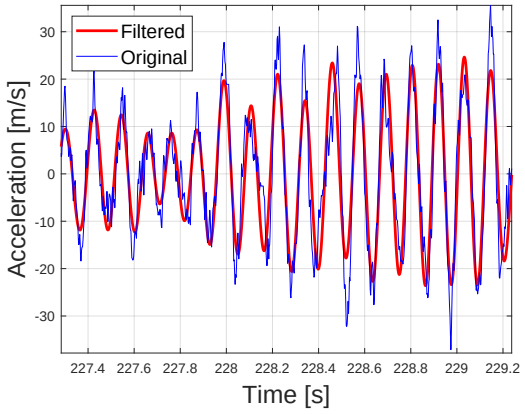

(c) Left middle wheel acceleration.

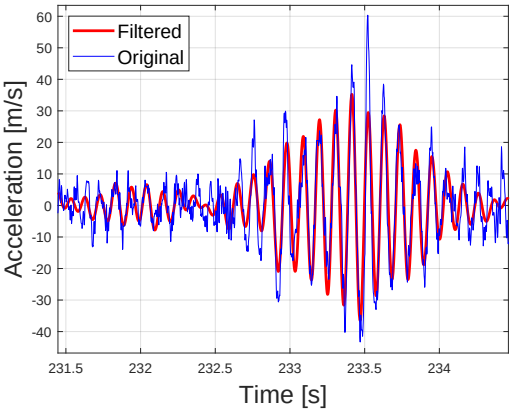

(d) Right middle wheel acceleration.

Figure B.2: Filtered and unfiltered vertical acceleration signals captured at the front and middle wheels.

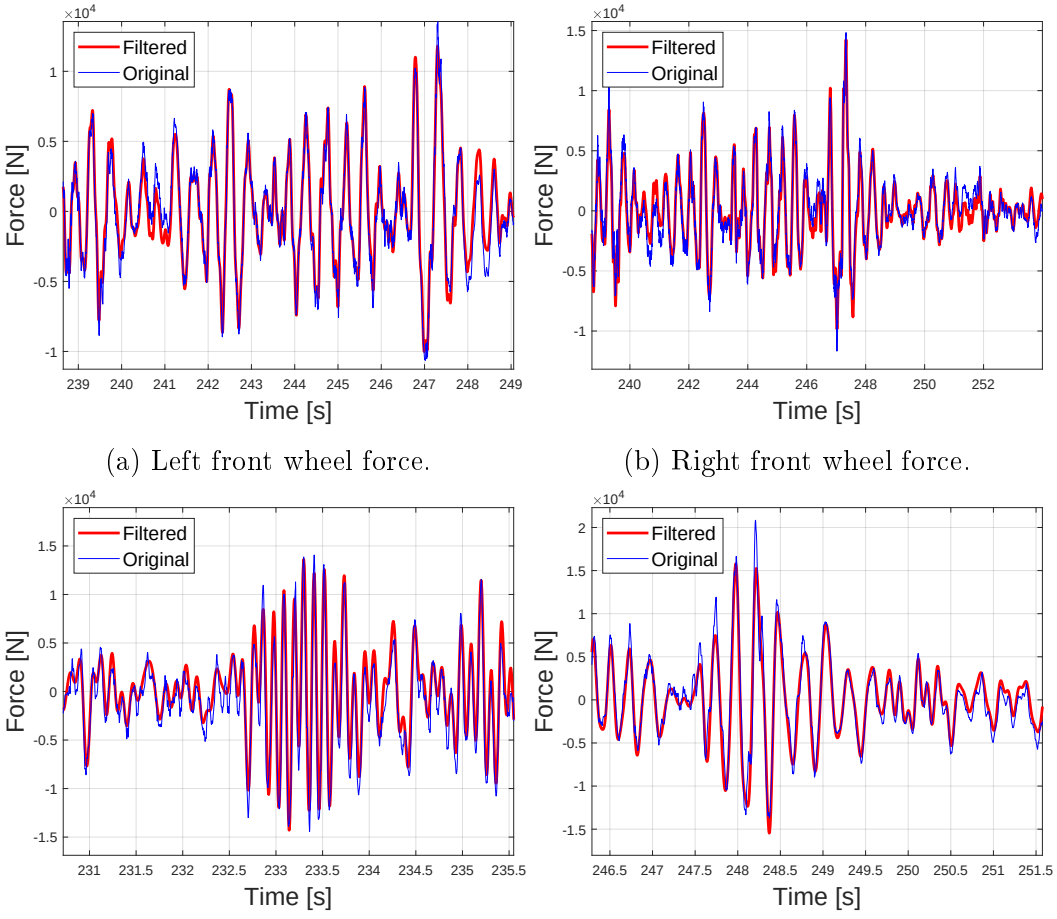

(a) Left front wheel force.

(b) Right front wheel force.

(c) Left middle wheel force.

(d) Right middle wheel force.

Figure B.3: Filtered and unfiltered vertical front and middle wheel forces.

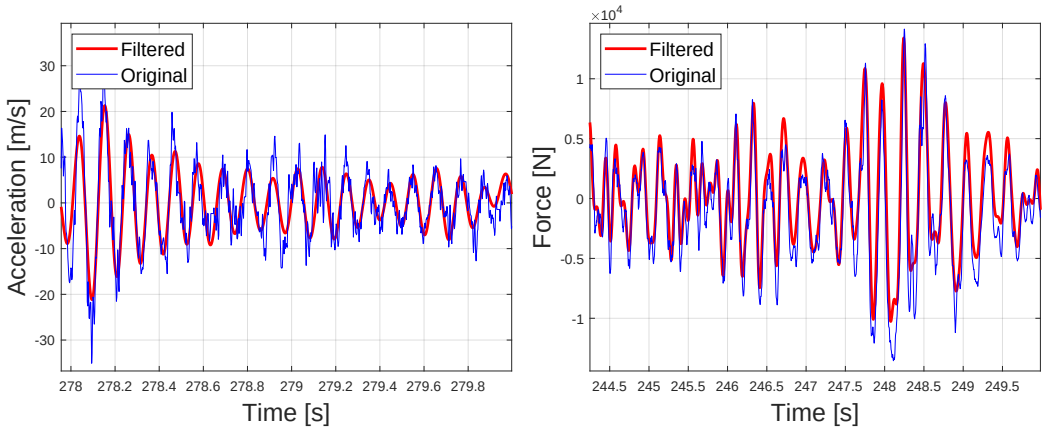

(a) Left rear wheel acceleration.

(b) Left rear wheel force.

Figure B.4: Filtered and unfiltered vertical accelerations and forces of the left rear wheel.

Appendix C

Payload size recovery using strain gauge field data

Estimations for the size of the payload on the truck's rear for Run 2 and Run 3 were recovered. Results of payload size recoveries using strains recorded by each individual strain gauge for Run 2 and Run 3 are provided in the tables below.

Table C.1: Recovered payload size using one strain gauge at a time for the Run 2 dataset.

Strain gauge (angle)	**Measured payload size [kN]**	**Recovered payload size [kN]**	**% Error**
1 (0°)	32.255	638.048	1878.1
1 (45°)	32.255	-170.214	627.7
1 (90°)	32.255	76.034	135.7
3 (0°)	32.255	-743.888	2406.3
3 (45°)	32.255	-361.876	1221.9
3 (90°)	32.255	-123.686	483.5
8 (0°)	32.255	112.93	250.1
8 (45°)	32.255	75.882	135.3
8 (90°)	32.255	682.633	2016.4
12	32.255	281.064	771.4
13	32.255	-380.649	1280.1
14	32.255	34.154	5.9
15	32.255	66.457	106.0
16	32.255	27.959	13.3
17	32.255	31.933	10.0
22 (0°)	32.255	60.281	86.9
22 (45°)	32.255	35.256	9.3

Continued on next page

Table C.1 – *Continued from previous page*

Strain gauge (angle)	**Measured payload size [kN]**	**Recovered payload size [kN]**	**% Error**
22 (90°)	32.255	-7.159	122.2
23.1 (0°)	32.255	-109.916	440.8
23.1 (45°)	32.255	-16.755	152.0
23.1 (90°)	32.255	8.391	74.0
23.2 (0°)	32.255	-1269.50	4035.8
23.2 (45°)	32.255	155.121	380.9
23.2 (90°)	32.255	-73.249	327.1
24 (0°)	32.255	219.467	580.4
24 (45°)	32.255	197.750	513.1
24 (90°)	32.255	20.825	35.4
25 (0°)	32.255	-12541.080	38981.0
25 (45°)	32.255	-196.019	707.7
25 (90°)	32.255	16.996	47.3
27 (0°)	32.255	585.261	1714.5
27 (45°)	32.255	-10621.457	33030.0
27 (90°)	32.255	-3027.028	9484.7
28 (0°)	32.255	-539.689	1773.2
28 (45°)	32.255	-160.252	596.8
28 (90°)	32.255	236.200	632.3
39 (0°)	32.255	-61.283	290.0
39 (45°)	32.255	-4208.342	13147.1
39 (90°)	32.255	-107.090	432.0

Table C.2: Recovered payload size using one strain gauge at a time for the Run 3 dataset.

Strain gauge (angle)	**Measured payload size [kN]**	**Recovered payload size [kN]**	**% Error**
1 (0°)	54.414	-14849.299	27389.5
1 (45°)	54.414	4799.567	8420.5
1 (90°)	54.414	-2572.722	4828.1
3 (0°)	54.414	4121.250	7473.9
3 (45°)	54.414	3300.965	5966.4
3 (90°)	54.414	2720.534	4899.7
8 (0°)	54.414	-3429.132	6401.9
8 (45°)	54.414	-4935.452	9170.2

Continued on next page

Table C.2 – *Continued from previous page*

Strain gauge (angle)	**Measured payload size [kN]**	**Recovered payload size [kN]**	**% Error**
8 (90°)	54.414	-12792.378	23609.4
12	54.414	-940.252	1828.0
13	54.414	-2599.416	4877.1
14	54.414	58.798	8.1
15	54.414	35.757	34.3
16	54.414	119.325	119.3
17	54.414	56.215	3.3
22 (0°)	54.414	8.140	85.0
22 (45°)	54.414	134.403	147.0
22 (90°)	54.414	-2.860	105.3
23.1 (0°)	54.414	-1424.094	2717.2
23.1 (45°)	54.414	-232.931	528.1
23.1 (90°)	54.414	57.462	5.6
23.2 (0°)	54.414	-4933.365	9166.4
23.2 (45°)	54.414	690.773	1169.5
23.2 (90°)	54.414	-211.134	488.0
24 (0°)	54.414	703.0391	1192.0
24 (45°)	54.414	5218.099	9489.6
24 (90°)	54.414	-831.724	1628.5
25 (0°)	54.414	34051.200	62478.0
25 (45°)	54.414	1060.836	1849.6
25 (90°)	54.414	399.706	634.6
27 (0°)	54.414	1188.509	2084.2
27 (45°)	54.414	-21485.631	39585.5
27 (90°)	54.414	-11443.670	21130.8
28 (0°)	54.414	-1324.552	2534.2
28 (45°)	54.414	-114.429	310.3
28 (90°)	54.414	406.959	647.9
39 (0°)	54.414	158.430	191.2
39 (45°)	54.414	-1599.22	3039.0
39 (90°)	54.414	142.502	161.9

List of References

Agilent Technologies (1999 May 2019). Practical strain gage measurements. Available at: `https://bit.ly/2Jm5UJb`

Agrawal, J. and Agrawal, S. (2015). Acceleration based particle swarm optimization for graph coloring problem. *Procedia Computer Science*, vol. 60, pp. 714–721.

Alfi, A. and Fateh, M.-M. (2010). Parameter identification based on a modified pso applied to suspension system. *Software Engineering Applications*, vol. 03, no. 1, pp. 221–229.

Alfi, A. and Modares, H. (2010). System identification and control using adaptive particle swarm optimization. *Applied Mathematical Modelling*, vol. 35, pp. 1210–1221.

Alvarez-Sánchez, E. (2013). A quarter-car suspension system: car body mass estimator and sliding mode control. *Procedia Technology*, vol. 7, pp. 208–214.

Bansal, J.C., Singh, P.K., Saraswat, M., Verma, A., Jadon, S.S. and Abraham, A. (2011). Inertia weight strategies in particle swarm optimization. *2011 Third World Congress on Nature and Biologically Inspired Computing*, pp. 633–640.

Brandt, A. and Brinker, R. (2014). Integrating time signals in frequency domain comparison with time domain integration. *Measurement*, vol. 58, no. 1, pp. 511–519.

Budynas, R.G. (1999). *Advanced Strength and Applied Stress Analysis*. 2nd edn. McGraw Hill, New York.

Cook, R.D., Malkus, D.S., Plesha, M.E. and Witt, R.J. (2007). *Concepts and Applications of Finite Element Analysis*. 4th edn. John Wiley & Sons. Inc. , New York.

Dhingra, A.K., Hunter, T.G. and Gupta, D.K. (2013). Load recovery in components based on dynamic strain measurements. *Journal of Vibration and Acoustics*, vol. 00, no. 1, pp. 1–9.

Doyle, S. (2019). Welcome to pynastrans documentation for master. Available at: `https://pynastran-git.readthedocs.io/en/latest/`

Drehmer, L.R.C., Casas, W.J.P. and Gomes, H.M. (2015). Parameters optimisation of a vehicle suspension system using a particle swarm optimisation algorithm. *Vehicle System Dynamics*, vol. 53, no. 4, pp. 449–474.

Gupta, D.K. (2013). *Inverse Methods for Load Identification Augmented By Optimal Sensor Placement and Model Order Reduction.* PhD, University of Wisconsin Milwaukee.

HBM (2015). *nCode GlyphWorks 11.0 Specification.* HBM United Kingdom Limited.

Hibbeler, R.C. and Yap, K.B. (2012). *Engineering Mechanics: Statics.* 13th edn. Pearson Education South Asia Pte Ltd, Singapore.

Hunter, T.G. (2018). Experimental correlation of an n-dimensional load transducer augmented by finite element analysis. *Wolf Star Technologies, LLC.*

Johannesson, P. and Speckert, M. (2013). *Guide to Load Analysis for Durability in Vehicle Engineering.* 7th edn. Wiley Automotive Ser.

Kennedy, J. and Eberhart, R. (1995). Particle swarm optimization. In: *Proceedings of the IEEE International Conference on Neural Networks.*

Kulakowski, B.T., Gardner, J.F. and Shearer, J.L. (2007). *Dynamic Modeling and Control of Engineering Systems.* 3rd edn. Cambridge University Press, New York.

Liao, L. (2011). *A Study of Inertia Relief Analysis.* Worldwide Aeros Corp.

Maher, D. and Young, P. (2011). An insight into linear quarter car model accuracy. *Vehicle System Dynamics*, vol. 49, pp. 463–480.

Mitchell, T.J. (1974). An algorithm for the construction of d-optimal experimental designs. *Technometrics*, vol. 16, no. 2, pp. 203–210.

My Little Salesman, Inc. (2019 Aug). 2012 mack granite roll off truck. Available at: `https://bit.ly/32NjL2S`

Pountney, R.E. and Dakin, J. (1992). Integration of test and analysis for component durability. *Environmental Engineering*, vol. 5.

Siemens (2014). *NX Nastran User's Guide.* Siemens Product Lifecycle Management Software Inc.

Siemens (2017). *NX Nastran 12 Quick Reference Guide.* Siemens Product Lifecycle Management Software Inc.

SubbaReddy, J., Bhavani, M., Kartheek, G. and Venkata Somi Reddy, J. (2018). Influence of parameters on safe design of leaf spring for static and dynamic loading using finite element analysis. *International Journal of Advance Engineering and Research Development*, vol. 5, pp. 505–519.

Ursem, R.K. and Vadstrup, P. (2004). Parameter identification of induction motors using stochastic optimization algorithms. *Applied Soft Computing*, vol. 4, no. 1, pp. 49–64.

Vanderplaats Research & Development, Inc. (2011). *DOT:Design Optimization Tools Users Manual*. 6th edn. VR&D, Colorado Springs.

Vanderplaats Research & Development, Inc. (2018). *Genesis Analysis Manual*. 17th edn. Vanderplaats Research and Development, Inc., Colorado Springs.

Wannenburg, J. (2007). *A Study of Fatigue Loading on Automotive and Transport Structures*. PhD, University of Pretoria.

Wannenburg, J. and Heyns, S. (2010). An overview of numerical methodologies for durability assessment of vehicle and transport structures. *Vehicle Systems Modelling and Testing*, vol. 05, no. 1, pp. 72–101.

Wikimedia Commons (2019 Aug).
Available at: `https://commons.wikimedia.org/wiki/File:Roll-Off.jpg`